FUNCTIONAL OXIDES WITH NITRIDE BUFFER LAYERS FOR HETEROEPITAXIAL DEVICES

A Dissertation

by

FAUZIA MOHAMMED HUSAIN KHATKHATAY

Submitted to the Office of Graduate and Professional Studies of
Texas A&M University
in partial fulfillment of the requirements for the degree of

DOCTOR OF PHILOSOPHY

Chair of Committee,	Haiyan Wang
Committee Members,	H. Rusty Harris
	Jim Ji
	Xinghang Zhang
Head of Department,	Chanan Singh

May 2015

Major Subject: Electrical Engineering

ABSTRACT

As conventional memory technologies approach their limit of scalability, there is a quest to find new technologies to replace existing memories. Of the emerging switching phenomena, ferroelectric switching and resistive switching have been considered for this work. Ferroelectricity is a property by which a material develops a spontaneous polarization that can be reversed by and external electric field. Resistive switching, the basis for the novel "memristor" devices, is a property that enables a device switch to a low or high resistance state depending on the magnitude and polarity of the applied voltage. In this work, various nanostructures have been explored to achieve property enhancement in functional oxides. For example, vertically aligned nanocomposite structures consist of two different materials that are simultaneously deposited onto a single substrate, and grow as two distinct phases. Vertically aligned nanocomposite structures offer the advantage of strain tuning through the vertical interfaces between phases.

First, to improve the ferroelectric properties of $BaTiO_3$, a conventional ferroelectric material, epitaxial vertically aligned nanocomposite $BaTiO_3$-CeO_2 films have been deposited on $SrTiO_3$ substrates. These films exhibit a columnar structure with high epitaxial quality. The films show a similar ferroelectric response as that of pure thin film $BaTiO_3$, but with an improved Curie temperature, despite the incorporation of CeO_2. These nanocomposite structures have been replicated on Si substrates using a double buffer layer of $SrTiO_3$/TiN to achieve the eventual integration of these films on

Si. No reduction in ferroelectric properties has been observed, but the films again showed an improvement in the Curie temperature.

Second, a simple resistive switching device has been demonstrated by the *in situ* partial oxidation of a TiN film under three different oxidation time periods. The oxidized region consists of near stoichiometric TiO_2, and serves as the oxide layer, while the unoxidized TiN serves as the bottom electrode. All films exhibit bipolar resistive switching and all films are forming-free. The forming-free property is attributed to an oxygen deficient TiO_{2-x} layer at the interface between the oxide and nitride regions.

Third, ZnO, a piezoelectric, has been selected as another complementary second phase material for $BaTiO_3$. Epitaxial and highly textured vertically aligned $BaTiO_3$-ZnO composite films have been deposited on $SrTiO_3$ substrates and $SrTiO_3$/TiN buffered Si substrates, respectively. Electrical characterization shows that the films grown on both substrates are ferroelectric at room temperature and exhibit similar properties. Composition analysis shows that both the laser fluence and the oxygen partial pressure can modulate the Ba/Ti cation stoichiometry which, in turn, impacts the ferroelectric properties. This is the first demonstration of the vertically aligned nanocomposite of $BaTiO_3$ and ZnO and its silicon based integration.

Finally, based on the excellent buffer layer and diffusion barrier properties of TiN for integrating functional oxides on Si, TiN has been applied as a protective layer on metal surfaces. A 500 nm thick TiN layer has been demonstrated to serve as an excellent diffusion barrier in extreme environments.

DEDICATION

to my family

ACKNOWLEDGEMENTS

I sincerely thank my advisor, Professor Haiyan Wang, for her advice and guidance throughout my term at Texas A&M University. She is an outstanding scientist and researcher, and it has been a privilege to work with and learn from her. She grooms her students to become independent researchers by demanding excellence with integrity, while allowing us the trust and freedom to try out new ideas and plan the course of our own research. Her counsel and steadfast support for her students extends beyond academic; she encourages us to lead healthy balanced lives with emphasis on personal growth. I continue to be inspired by her energy, ambition, tenacity, and, above all, her passion for scientific discovery.

I would like to acknowledge all my committee members, Dr. Rusty Harris, Dr. Jim Ji, and Dr. Xinghang Zhang for their help and attention on my research. I want to thank my former and present group members, Dr. Ickchan Kim, Dr. Joon-Hwan Lee, Dr. Chen-Fong Tsai, Dr. Michelle Myers, Dr. Aiping Chen, Dr. Li Chen, Dr. Qing Su, Dr. Yuanyuan Zhu, Liang Jiao, Clement Jacob, Jie Jian, Wenrui Zhang, Leigang Li, Jijie Huang, Meng Fan, and Han Wang for their camaraderie and collaboration, in addition to the valuable insight I have gained through our many discussions. I especially extend my gratitude to the staff at the Department of Electrical and Computer Engineering for their prompt and indispensable assistance with administrative procedures and technical issues in the lab. I also like to acknowledge the faculty and staff at the Microscopy and Imaging

Center as well as the Materials Characterization Facility for their help and advice with equipment training, sample preparation, measurement, and analysis.

Finally, I thank my family for their continued encouragement and unwavering support for all my endeavors throughout my life. I owe everything to them.

TABLE OF CONTENTS

Page

LIST OF FIGURES

Page

LIST OF TABLES

Page

CHAPTER I

INTRODUCTION AND LITERATURE REVIEW

The most commonly used memory technologies today are the volatile random access memories (RAM), static RAM (SRAM) and dynamic RAM (DRAM), and the non-volatile flash memory based on complementary metal oxide semiconductor (CMOS) technology.[1-3] Data storage in all these memory types is based on the charge state. The semiconductor industry, due to the increasing technological demands, is scaling down transistors to double the transistor density per chip every 18 months, following Moore's Law. While in the past, SRAM, DRAM, and flash have been successfully scaled down to improve device performance, increase chip density, and reduce the cost, they are soon approaching the feasible limits of size reduction. As a consequence attempts are underway to find new memory types that have a data storage principle different from existing technologies, also referred to as the "more than Moore" approach. These new materials should, in addition to being scalable and non-volatile, match or surpass the performance of existing technologies. Based on this, some potential non-volatile memory candidates have been explored based on ferroelectricity, magnetism, spin-torque transfer, phase change, and resistance change. In this work the two main types considered are ferroelectricity and resistance change. The following is a brief review on oxide materials and their functionalities, with emphasis on these two phenomena. Also included is a brief discussion on TiN as a potential buffer layer and diffusion barrier for eventual integration of these materials on Si.

1.1 Functional oxide thin films

1.1.1 Overview of functional oxide thin films

Functional oxides, an overwhelming majority of which consist of transition metal oxides, are the basis for "smart" materials whose properties can be considerably altered by environmental changes or by external stimuli. In addition to memory devices, these materials offer great potential in sensing and actuating devices as well as in microelectromechanical systems (MEMS). Advances in nanotechnology and fabrication have enabled precise control of device dimensions down to the nanoscale, where unique functionalities have been realized, hitherto not observed in bulk materials. These functionalities are determined largely by the crystal structures, bonding, and defects in these oxides.

1.1.2 Oxide crystal structures

Crystal structures form the basis for crystal chemistry, and the understanding of these structures is crucial to the synthesis and design of new functionalities. Functional metal oxides present a wide variety of crystal structures based on the bonding between their component elements.[4] Bonding in functional oxides is predominantly ionic, though varying levels of covalency are observed and could have a direct impact on the material properties.[5] A brief classification of functional oxides crystal structures is summarized in Table 1.1.

Table 1.1 Common functional oxide crystal structures.

System	Structure	Representative Materials
Binary	Rock salt	MgO, TiO, VO, CoO, MnO
	Wurtzite	ZnO, BeO
	Fluorite	CeO_2, ZrO_2, TbO_2, ThO_2
	Antifluorite	Li_2O, Na_2O, K_2O
	Cuprite	Cu_2O, Ag_2O, Pb_2O
	Rutile	TiO_2, IrO_2, MoO_2, RuO_2, WO_2
	Bixbyite	Pr_2O_3, Tl_2O_3
	Corundum	Al_2O_3, V_2O_3, Cr_2O_3
Ternary	Ilmenite	(Fe, Co, Ni, Mn)TiO_3, $LiNbO_3$
	Spinel	$LiTi_2O_4$, $NiFe_2O_4$, $MgAl_2O_4$
	Perovskite	$SrTiO_3$, $BaTiO_3$, $BiFeO_3$, $La_xSr_{1-x}MnO_3$
	Layered perovskite	$YBa_2Cu_3O_7$
	Ruddlesden-popper series	$SrRuO_3$, Sr_2RuO_4, $Sr_3Ru_2O_7$

1.1.2.1 Binary oxides

For binary oxides, which include monoxides (MO; M = metal), dioxides (MO_2), and sesquioxides or binary trivalent oxides (M_2O_3), common structures include rock salt, wurtzite, rutile, fluorite, bixbyite, and corundum. These materials are typically insulators

(MgO, CeO_2, Al_2O_3) or semiconductors (ZnO, TiO_2), though some monoxides can be metallic (LaO), superconducting (NbO), or even magnetic (EuO). Several binary oxides used in this study are introduced in detail below.

CeO_2, a rare earth oxide, has a fluorite structure belonging to the space group $Fm\bar{3}m$.[4] In this structure, shown in Figure 1.1, the unit cell consists of a face-centered cubic (f.c.c) of Ce cations, with O anions in the interstitial octahedral sites. CeO_2 has a lattice constant a = 5.41 Å with a Ce-O bond length of 2.34 Å; the Ce^{4+} and O^{2-} are eight-fold and four-fold coordinated, respectively.[6] CeO_2 is a wide bandgap insulator that has gained widespread popularity as an automotive emissions-reduction catalyst[7] and, more recently, as an oxygen ion transporting electrolyte in solid-oxide fuel cells.[8]

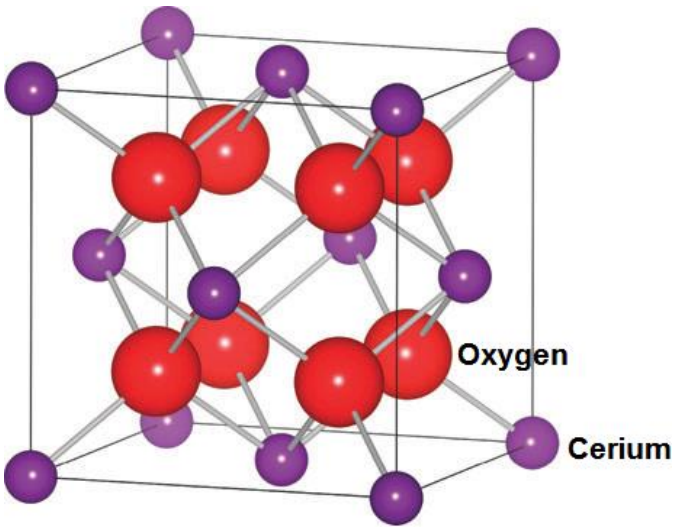

FIG. 1.1 Crystal structure of CeO_2.[9]

TiO_2 is a semiconducting oxide that naturally crystallizes into three main polymorphs, namely rutile, anatase, and brookite.[10] A few additional high pressure structures of TiO_2 have been synthesized,[11,12] but the most commonly used forms in thin film applications are rutile and anatase, shown in Figure 1.2. Rutile has a tetragonal structure with lattice parameters $a = b = 4.584$ Å and $c = 2.953$ Å, and belongs to the space group $P4_2/mnm$.[10] Anatase is also tetragonal with lattice constants $a = b = 3.782$ Å and $c = 9.502$ Å, and belongs to the space group $I4_1/amd$.[10] Both structures have six O atoms that surround each Ti in a distorted octahedron. In the case of rutile, one corner is shared by adjacent octahedra along the <110> directions, while in anatase, one corner is shared by adjacent octahedral forming (001) planes. In both cases, the stacked octahedral result in O atoms with three-fold coordination. TiO_2 is used in a wide variety of applications including catalysis applications, optoelectronic devices like photodiodes and solar cells, optical coatings, and MOSFET devices.[10,13-15] More recently, TiO_2 has gained considerable popularity as a prototype resistive switching or "memristive" oxide for next-generation memory devices.[16]

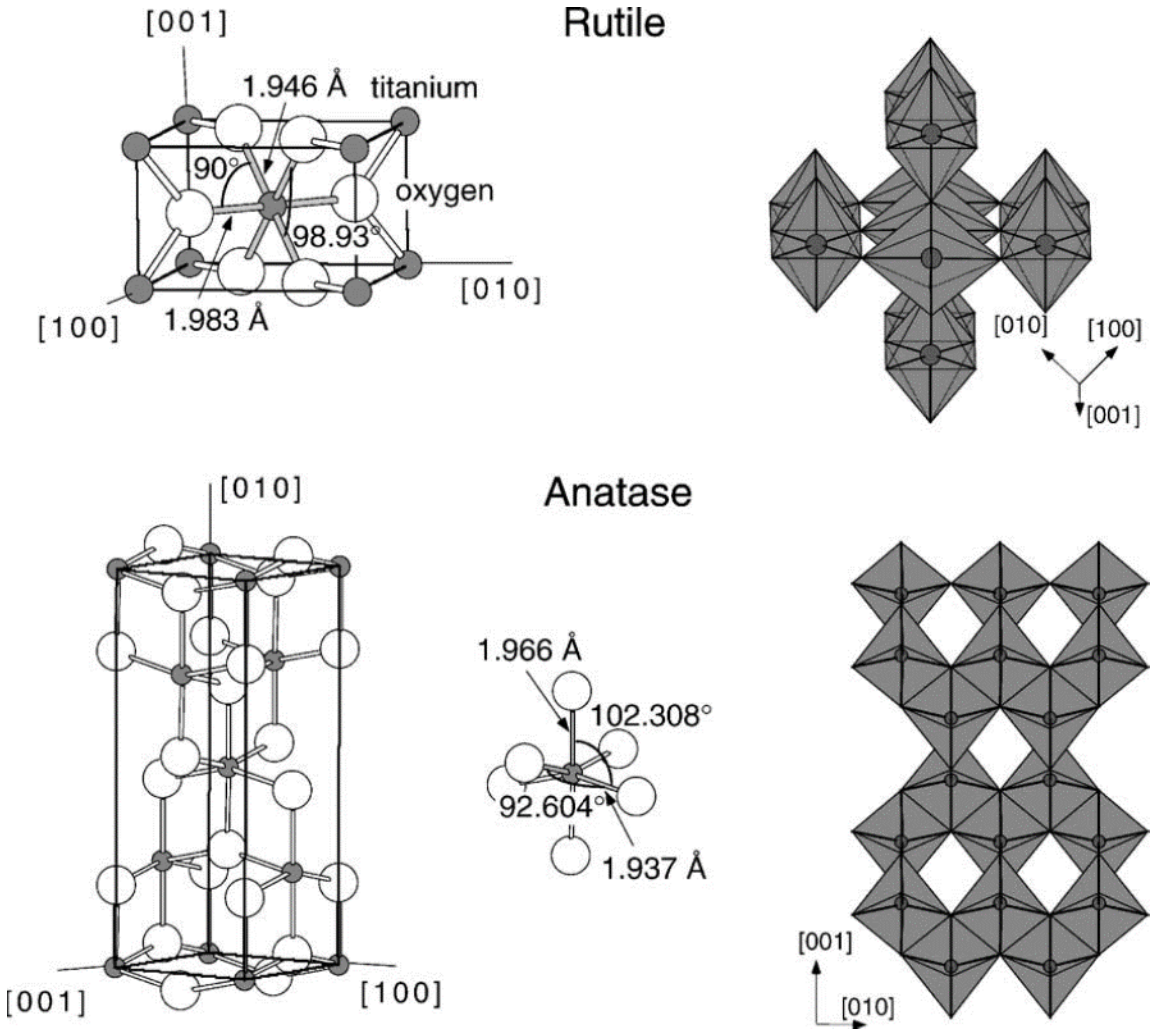

FIG. 1.2 Crystal structure of rutile and anatase TiO_2.[10]

ZnO is a direct bandgap semiconducting oxide that displays different crystal structures like rocksalt, cubic zincblende, and wurtzite, with hexagonal wurtzite being the most stable crystalline form.[17] Shown in Fig. 1.3, wurtzite ZnO has hexagonal lattice constants a = 3.24 Å and c = 5.21 Å, and belongs to the space group $P6_3mc$.[18] Each Zn^{2+} is surrounded by four O^{2-}. This tetragonal coordination gives rise to a lack of symmetry,

responsible for properties like piezoelectricity. ZnO has very rich defect chemistry also with prominent point or one-dimensional defects, which include mostly O vacancies and Zn interstitials. Due to its wide bandgap of 3.4 eV, ZnO has huge potential in optoelectronic devices. ZnO is also a unique oxide system that can be doped to display *n* and *p* type characteristics for homoepitaxial oxide-based *p*-*n* junctions.[19-21]

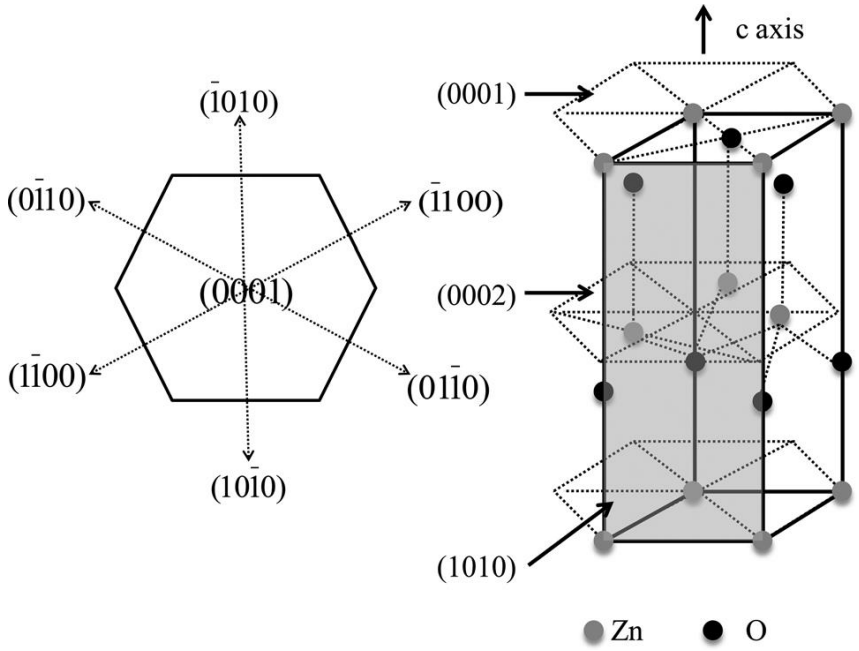

FIG. 1.3 Crystal structure of ZnO.[22]

1.1.2.2 Ternary oxides

More complex crystal structures are found among the ternary oxides, which include ilmenite ($(AB)O_3$; A, B = metal), spinel (AB_2O_4), perovskite (ABO_3), and

perovskite-derived structures like the Ruddlesden–Popper series and layered-perovskites ($A_{n+1}B_nO_{3n+1}$).[4,5] These materials display a variety of interesting properties like piezoelectricity, thermoelectricity, ferroelectricity, ferromagnetism, multiferroicity, and superconductivity.

The perovskite structure, shown in Figure 1.4, is based on the ReO_3 structure, with a corner shared octahedral in the unit cell with the A and B cations coordinated by 12 and 6 oxygen ions, respectively; the ionic radius of A is larger than that of B.

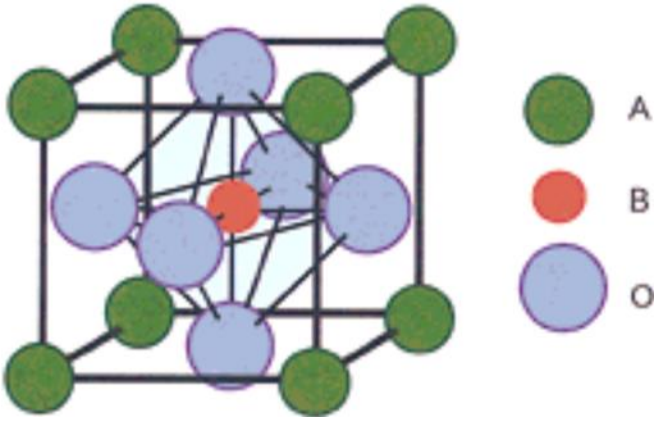

FIG. 1.4 The perovskite crystal structure.[23]

For an ideal cubic perovskite, the lattice parameter *a* geometrically related to its three component ionic radii, r_A, r_B, and r_O by the following equation:[24]

$$a = \sqrt{2}(r_A + r_B) = 2(r_B + r_O) \quad (1\text{-}1)$$

Goldshmidt's tolerance factor *t* is the ratio of the two expressions above, defined as[24]

$$t = \frac{r_A + r_O}{\sqrt{2}(r_B + r_O)} \quad (1\text{-}2)$$

In the case of $SrTiO_3$, a prototype ideal cubic perovskite, r_A = 1.44 Å, r_B = 0.605 Å, and r_O = 1.40 Å, resulting in t = 1. A deviation from unity in the value of t represents a distortion to the cubic unit cell. With the exception of $SrTiO_3$, most ABO_3 perovskites have a distortion in the cubic cell structure. ABO_3 stoichiometric perovskites can be divided into three classes depending on the valence states of A and B: $A^{+1}B^{+5}O_3$ (A = Na, K, Ag; B = I, Nb, Ta), $A^{+2}B^{+4}O_3$ (A = Ca, Sr, Ba, Pb; B = Ti, Zr, Fe, Mn, Sn, Mo, Hf), and $A^{+3}B^{+3}O_3$ (A = Y, Bi, La, Pr, Sm ; B = Al, Ti, V, Fe, Co, Mn, Cr). Oxides from the third class are (anti)ferromagnetic ($BiFeO_3$, $La_{0.7}Sr_{0.3}MnO_3$), while those from the first two classes are ferroelectric ($BaTiO_3$, $NaNbO_3$).

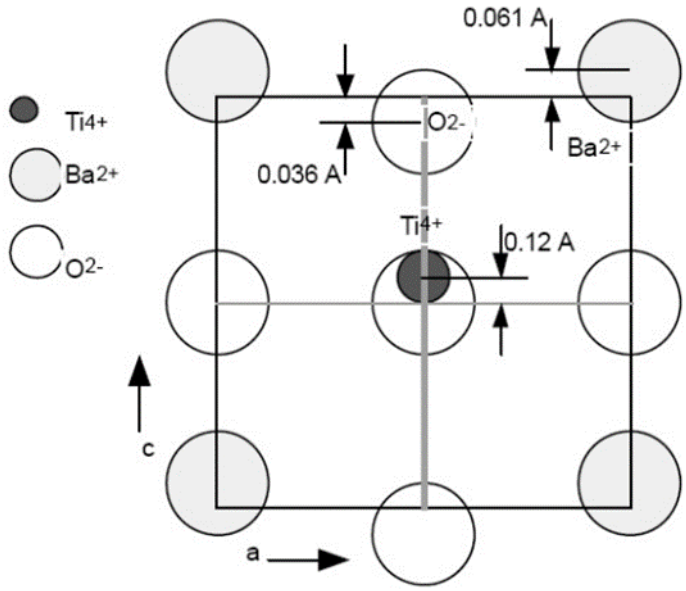

FIG. 1.5 Ionic displacements in $BaTiO_3$.[25]

$BaTiO_3$, a room temperature tetragonal perovskite shown in Figure 1.5, has lattice constants of a = 3.992 Å and c = 4.036 Å, and belongs to the space group *P4mm*.[25] The tetragonal distortion from the cubic structure results in ionic displacements of 0.061 Å in the Ba^{2+}, 0.012 Å in the Ti^{4+}, and -0.036 Å in the O^{2-} (only for the top and bottom faces, there is no change in the position of the O^{2-} ions along the vertical faces).

1.1.3 Functionality of oxides

Functional oxide thin films present a variety of interesting phenomena including dielectric, optical, ferroelectric, ferromagnetic, multiferroic, and resistance switching properties, that arise from their specific crystal structure, (a)symmetry, and defects. Ferroelectricity is a property of by which some materials possess a spontaneous polarization that can be reversed by an applied electric field. Resistive switching is a phenomenon by which a material switches to a low or high resistive state depending on the magnitude and/or polarity of the applied voltage. These two phenomena will be discussed in further detail in a later section.

HfO_2, a high dielectric permittivity (high-*K*) oxide has been successfully implemented as a gate oxide to replace SiO_2.[26] Other binary oxides under consideration include ZrO_2, TiO_2, $Al2O_3$, and Y_2O_3.[26-28] Dielectric permittivity in insulating perovskites is much higher than that of binary oxides, so a major application for these materials is in ceramic capacitors and high-*K* dielectric applications.[25] $BaTiO_3$, $SrTiO_3$, $LaAlO_3$, and $LaGdO_3$ are being considered as potential gate oxide materials in transistor

devices.[27-29] In ferroelectric perovskites, the dielectric permittivity changes as a function of the applied field. These electrically tunable dielectrics are attractive for microwave devices that can be tuned either electrically or magnetically.[30] Relaxor ferroelectrics, such as $Pb(Mn,Nb)O_3$ and $Pb(Zn,Nb)O_3$, have dielectric phase transitions over a wide range of temperature (called diffuse phase transitions).[4] These materials are relatively temperature insensitive and have very high dielectric permittivity, and are thus used for compact chip capacitors.[25]

ZnO has attracted the most attention among functional oxides as its electronic, magnetic, and optical properties can be tailored through doping, alloying, nano-engineering, heterostructures, and quantum wells.[31] It holds promise for optical devices based on excitonic effects due to its large exciton binding energy of 60 meV.[32] It is a strong ultraviolet (UV) wavelength absorber and emitter owing to its wide and direct bandgap making it ideal for optoelectronic applications including UV and blue laser diodes, light-emitting diodes, and photodetectors.[32] In TiO_2, photogenerated carriers react with the lattice oxygen to create oxygen vacancies at the surface, changing its reactivity in the presence of light, making it an attractive photocatalyst material for photodegradation of environmental pollutants.[33] It is also widely used in photovoltaic devices due to its ability to absorb light in the visible region.[33] An important property of perovskite oxides, the electro-optic effect is a change in the refractive index of a dielectric due to an applied electric field.[25] Some of these materials display electrically controlled bifringence and light scattering.[4] Electro-optic materials are transparent in the visible to infrared wavelength range. Potential applications for electro-optic materials are

in optical displays, optical fibers, light valves, and beam deflectors. Typical materials are $(Pb,La)(Zr,Ti)O_3$, $LiNbO_3$, and $LiTaO_3$.

Ferromagnetic materials develop a spontaneous magnetization in the absence of a magnetic field. Research on ferromagnetic materials continues to garner attention as spintronic devices are considered among the class of the so-called "next-generation" memory devices and potential candidates for "universal" memory devices to replace those based on current CMOS technology.[34,35] The operating principle of spintronic devices is based on magnetoresistance, the property of a material by which its electrical resistivity changes under an external magnetic field. Multilayer devices have been engineered to exhibit interesting structures and properties based on the combination of ferromagnetic, insulating, nonmagnetic, and antiferromagnetic materials. The rare-earth perovskite manganate families of $LaMnO_3$, i.e. $(La,Sr)MnO_3$, $(La,Ca)MnO_3$ are at the forefront of materials research in this area.[36]

A multiferroic material is one that simultaneously displays the properties of ferroelectricity and ferromagnetism, making it possible to change the magnetization by an applied electric field or to change the polarization by an applied magnetic field. Like ferroelectrics and ferromagnetics, multiferroics also are an exciting prospects for memory applications, combining the properties of both while offering functionalities beyond both. The most common single phase multiferroic perovskites include $BiFeO_3$, $BiMnO_3$, $YMnO_3$, and $Pb(Fe,Nb)O_3$.[37,38] More recently, composite films of ferroelectric and ferromagnetic materials have been engineered to explore their magnetoelectric coupling, e.g. $CoFe_2O_4$ with ferroelectrics like $Pb(Zr,Ti)O_3$ and $BaTiO_3$.

Superconductivity is a property by which a material has zero electrical resistance below a critical temperature, characterized by a sharp discontinuity in the resistivity at that temperature. In their superconducting state, superconductors have essentially zero loss, or zero power dissipation. However, this lossless property only exists below the critical transition temperature and the critical current density of the superconducting material. Below the transition temperature, superconductors also exhibit diamagnetism, with exclusion of the magnetic field below a critical field. Prospective applications for superconductors include superconducting cables for electric power related transmission, motors, generators and magnets. Cuprate materials, like the families of $La_{(2-x)}Sr_xCuO_4$ and $YBa_2Cu_3O_{7-x}$ are at the forefront of superconductor research.[39,40]

1.1.3.1 Ferroelectricity

1.1.3.1.1 Origin of ferroelectricity

Based on crystallographic symmetry, there are 32 possible point groups of crystal structures, stemming from the seven basic crystal systems.[41] Shown in Table 1.2, there are 21 point groups that are noncentrosymmetric, among which 20 develop an electrical polarization due to applied mechanical stress, namely piezoelectrics.[25] The lack of a center of symmetry causes a shift in the relative positions of the anions and cations when mechanical stress is applied, resulting in the formation of electrical dipoles. The appearance of electrical charge as a result of mechanical stress is called the direct piezoelectric effect, while a strain induced due to an applied electric field is called the converse piezoelectric effect. The direct effect results in a generator action, where

mechanical energy is converted into electrical energy, and are used in sensing devices and more recently, energy harvesting devices.[42,43] The result of the converse piezoelectric effect is a motor action, where electrical energy is converted into mechanical energy, used in acoustic and ultrasonic devices, microelectromechanical systems, and transducers.[43,44]

Several figures of merit are considered when evaluating the piezoelectric properties of a material:[23,25,45]

The piezoelectric strain constant d (also called the piezoelectric charge coefficient) relates the induced polarization P to the applied mechanical stress X in the direct piezoelectric effect by

$$P = dX \tag{1-3}$$

d also relates the induced strain x to the external electric field E in the converse piezoelectric effect by

$$x = dE \tag{1-4}$$

Table 1.2 Crystallographic classification of point groups according to centrosymmetry and polarity.[25] The shaded groups are piezoelectric, while those within the bold line are pyroelectric.

Polarity	**Symmetry**	**Crystal System**										
		Cubic		Hexagonal		Tetragonal		Rhombohedral		Orthorhombic	Monoclinic	Triclinic
non-polar (22)	centro (11)	$m3m$	$m3$	$6/mmm$	$6/m$	$4/mmm$	$4/m$	$\bar{3}m$	$\bar{3}$	mmm	$2/m$	$\bar{1}$
	non-centro (11)	432	23	622	$\bar{6}$	422	$\bar{4}$	32		222		
		$\bar{4}3m$		$\bar{6}m2$		$\bar{4}m2$						
polar (10)	non-centro (10)			$6mm$	6	$4mm$	4	$3m$	3	$mm2$	2 m	1

d has units of C/N for the direct effect and m/V in the case of the converse effect. *d* is typically written as d_{ij}, indicating that the particular coefficient relates the polarization perpendicular to the *i* direction due to a mechanical stress applied in the *j* direction. For example, d_{33} denotes the coefficient for the polarization generated in the vertical direction due to a stress applied in the vertical direction, and d_{31} denotes the coefficient for the polarization in the vertical direction due to a stress applied in the lateral direction. A similar notation is used for other variables defined in this section.

E is related to the externally applied stress *X* by the piezoelectric voltage constant *g* by

$$E = gX \tag{1-5}$$

The relationship between *d* and *g* is given by

$$g = \frac{d}{\varepsilon_0 \varepsilon} \tag{1-6}$$

where ε is the permittivity of the piezoelectric material (also known as the dielectric constant) and ε_0 is the permittivity of free space.

An important gauge for the rate of conversion between mechanical energy and electrical energy is the electromechanical coupling factor *k* given by

$$k^2 = \frac{stored\ mechanical\ energy}{input\ electrical\ energy} = \frac{stored\ electrical\ energy}{input\ mechanical\ energy} = \frac{d}{\varepsilon_0 \varepsilon \cdot s} \tag{1-7}$$

where *s* is the elastic compliance of the material.

Among the 20 piezoelectric crystal classes, 10 spontaneously form permanent dipoles depending on the operating temperature.[25] These materials are designated as pyroelectrics because the magnitude of the spontaneous polarization is temperature dependent. Within the lattice of these crystal classes, there exists a unique polar axis, due

to which they are also called polar materials.[23] Ferroelectrics are a subgroup of pyroelectrics, which possess a spontaneous polarization that can be reversed by the application of an external electric field. The perovskite group, or the oxygen octahedral group, is the most commonly implemented family of ferroelectric materials. In the typical ABO_3 unit cell, the polarization reversibility is primarily due to the displacement of the body centered B-site atom, housed within the corner-linked oxygen octahedral.[23] Upon the application of an electric field, the B-site atom assumes its new position along the direction of this field, corresponding to one of six polarization states depending on the direction of the applied field, polarization up and polarization down, shown in Figure 1.6. The small ionic movement results in a change in the dimensions of the unit cell and consequently the ceramic material becomes polarized. The material is ferroelectric when the dipoles are oriented parallel to each other. In cases where they are oriented in an antiparallel arrangement, the material is antiferroelectric.[4]

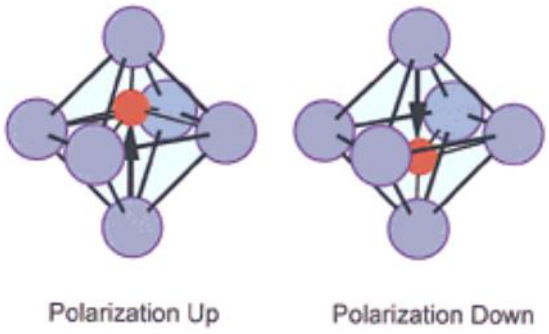

FIG. 1.6 Two of six possible polarization states caused by the ionic movement of the B-site cation.[23]

1.3.1.1.2 Ferroelectric polarization hysteresis loop

Shown in Figure 1.7 is a typical ferroelectric polarization-electric field (P-E) hysteresis loop showing the change in polarization as a function of the applied field (or applied voltage), corresponding to two opposite polarization states.

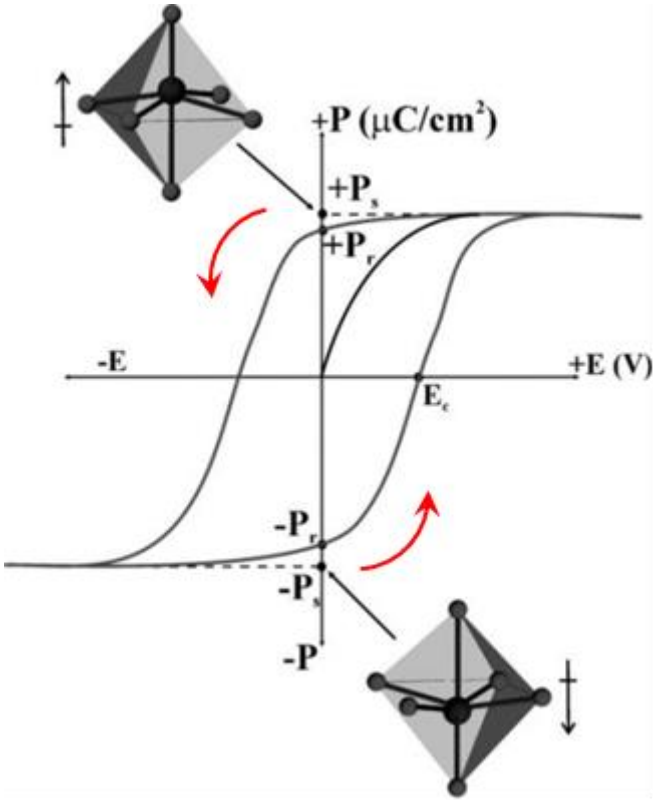

FIG. 1.7 Ferroelectric P-E loop corresponding to the two lattice distortions, polarization up and polarization down.[46]

The origin of the hysteresis loop is the rearrangement of dipoles due to an applied field. In the virgin state, the dipoles are randomly oriented, resulting in zero net

polarization,[4] and the applied electric field causes the dipoles to orient parallel to each other in the direction of the field. Some figures of merit are considered when evaluating a ferroelectric material.[46] The spontaneous polarization (P_s) is the total dipole moment per unit volume of a poled ferroelectric material, also called the saturation polarization because its value does not further increase with increasing the electric field. The remnant polarization (P_r) is the polarization retained when the electric field is removed. The coercive field (E_c) is the magnitude of the electric field required to force the polarization to zero. The switching field (E_s) is the magnitude of the field required for complete reversal of polarization.

1.3.1.1.3 Curie temperature

Another important ferroelectric parameter is the Curie temperature (T_C), a phase transition temperature beyond which, the crystal transforms from a noncentrosymmetric structure to a cubic centrosymmetric structure. In this so-called paraelectric phase, the thermal motion cancels out electron spins, and the spontaneous polarization completely disappears. To restore a poled ferroelectric back to its virgin state, the material must be heated beyond its T_C, and cooled back down to its ferroelectric state in the absence of an electric field. This process, called thermal depoling, restores the random orientation of the dipoles resulting in a net polarization of zero.[23] $SrTiO_3$ has a T_C of -168 ^oC, and is therefore cubic and paraelectric at room temperature.[47] Table 1.3 shows a comparison of the ferroelectric properties of common ferroelectric materials.

Table 1.3 Remnant polarization and Curie temperature of common ferroelectrics.

Material	***Pr*** **(μC/cm^2)**	T_C **(ºC)**
$BaTiO_3$	25-27	120-130
$PbZr_xTi_{1-x}O_3$	35	328
$BiFeO_3$	50-60	825
$SrBi_2TaO_7$	7-10	327

The ferroelectric phase always has a lower symmetry than the paraelectric phase. An anomaly is observed in the change in dielectric constant with temperature at the phase transition points, with a maximum at the T_C. The permittivity falls off with increasing temperature according to the Curie-Weiss law given by:

$$\varepsilon = \varepsilon_0 + \frac{C}{T-T_0} \approx \frac{C}{T-T_0} \tag{1-8}$$

where C is the Curie constant, T_0 ($T_0<T_C$) is the Curie-Weiss temperature. This anomaly in the dielectric constant at T_C is observed in antiferroelectrics as well.[4] Many ferroelectrics undergo several successive phase transitions which are all ferroelectric, which are accompanied by changes in the physical unit cell dimensions as well as dielectric, thermal, and elastic properties of the material, as shown in the example of $BaTiO_3$ in Figure 1.8.[48]

Since all ferroelectrics are also pyroelectrics and piezoelectrics, their specific applications are limited by their T_C.[25] For ferroelectric memory applications, the material should have a T_C well above room temperature, i.e. it should be ferroelectric rather than paraelectric at room temperature. Conversely, for high-K dielectric capacitor

applications, the T_C must be close to the operating temperature, to take advantage of the maximum value of the dielectric constant. In the case of pyroelectric sensors, the spontaneous polarization below the T_C must be highly temperature dependent. Finally, piezoelectric sensors and actuators must have a T_C far above room temperature so that they can be implemented in a wide temperature range.

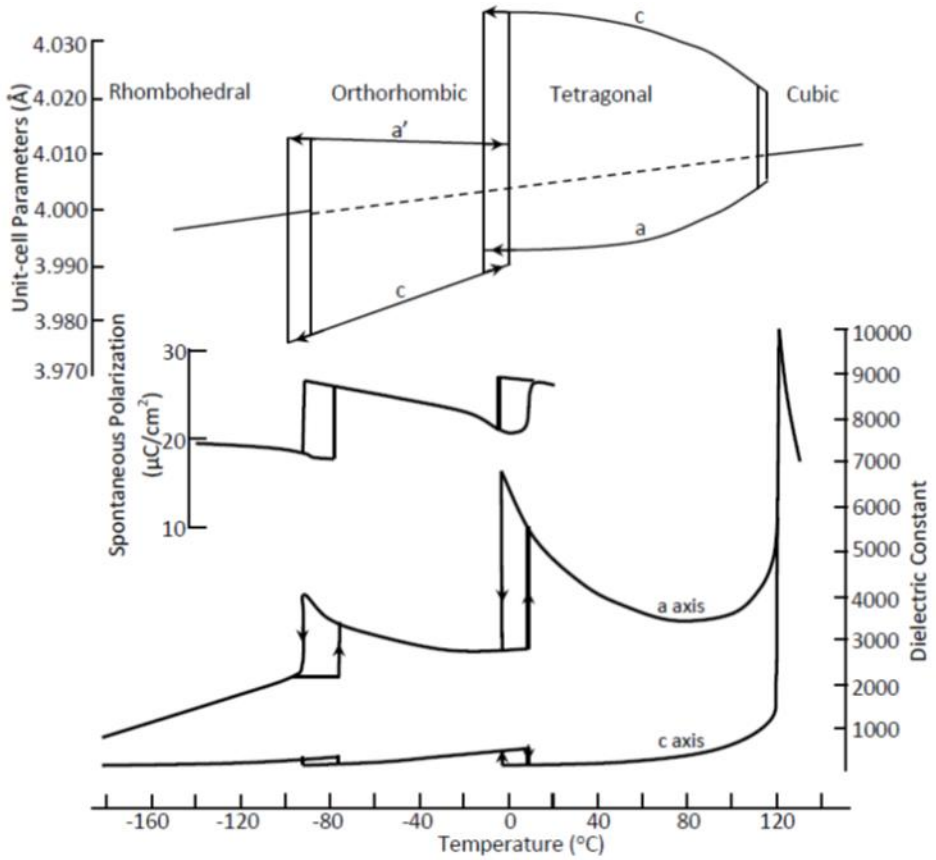

FIG. 1.8 Variation of the unit cell dimensions, spontaneous polarization, and dielectric constant as a function of temperature in $BaTiO_3$.[48]

1.3.1.1.4 Ferroelectric materials

The most common piezoelectric and ferroelectric materials, by far, are the Pb-based family of $PbZr_xTi_{1-x}O_3$ (PZT), a combination of $PbZrO_3$ and $PbTiO_3$, because of their good thermal stability and strong electromechanical coupling.[49] The optimal composition for superior piezoelectric and dielectric properties is at the morphotropic phase boundary between its rhombohedral and tetragonal phases at $PbZr_{0.52}Ti_{0.48}O_3$. PZT materials have a reported d_{33} values up to 779 pC/N, an electromechanical coupling factor of 0.5, and a T_C between 300-400 ^oC.[23,50] Moreover, PZT ceramics get easily poled, they are easier to sinter, have a broad range of dielectric constants, and form solid-solutions in many different compositions.[23] PZT is often doped to substitute Pb with La forming $(Pb,La)(Zr,Ti)O_3$ (PLZT). Other popular Pb-based material systems are $Pb(Mg_{1/3}Nb_{2/3})O_3$ (PMN) and $Pb(Zn_{1/3}Nb_{2/3})O_3$ (PZN).

In recent years, however, the need to eliminate the use of Pb-based materials has become apparent due to a growing environmental consciousness, and especially owing to the toxic effects of Pb on humans.[50,51] Though Pb-based devices are still the most popular due to their outstanding piezoelectric and ferroelectric properties, efforts are underway to develop materials that have properties that can match those of Pb-based materials. Potential Pb-free perovskites include titanates such as $BaTiO_3$, $(Ba,Sr)TiO_3$, $(Bi,Ni)TiO_3$, and $(Bi,K)TiO_3$, niobiates like $LiNbO_3$, $KNbO_3$, $NaNbO_3$, tantalates such as $NaTaO_3$, $(Sr,Ba)TaO_3$, and bismuth perovskites including $BiFeO_3$ and $BiScO_3$.[23,25,50,51] Non-perovskites include the tungsten bronze group and the bismuth layer-structured materials. The main drawbacks to widespread implementation of these Pb-free materials

have been their relatively lower T_C, poorer electromechanical coupling, and difficulty in poling.[23,51]

1.3.1.1.5 Barium titanate

$BaTiO_3$ is a highly stable chemical compound, the first perovskite discovered to have piezoelectricity and ferroelectricity with an electromechanical coupling factor of 0.35, and the first ceramic to be implemented in a piezoelectric transducer.[23,45] However, it is severely limited in its range of applications owing to its low T_C of ~120 ^oC. It is typically doped to modify its T_C and improve its properties, depending on the intended application. For high permittivity dielectric applications, dopants called T_C shifters like $SrTiO_3$, $PbTiO_3$, and $CaZrO_3$ are incorporated to increase or decrease the T_C. Sr can reduces the T_C, while Pb can increase the T_C, Ca can increase the temperature range for stability of the tetragonal phase, while Co can decrease the losses under high electric field without compromising on the piezoelectric constants. T_C depressors like $MgZrO_3$, $Bi_2(SnO_2)_3$, and $NiSnO_3$ are added to lower the peak in the dielectric constant at T_C.

Shown in Figure 1.9 are the polarization directions for the different phases of $BaTiO_3$.[52] In the cubic phase in Figure 1.9 (d) beyond the T_C, spontaneous polarization disappears so no polarization axis is shown. For the rhombohedral phase for temperatures less than -90 ^oC in Figure 1.9 (a), the displacement of the Ti^{4+} atom is along the [111] direction. In the orthorhombic phase in the temperature range of -90 ^oC to 5 ^oC, it is along the [011] direction as shown in Figure 1.9 (b). Finally, in the tetragonal phase in Figure 1.9 (c), in the temperature range of 5 ^oC up to the T_C, the polarization axis is in the [001] direction or along *c*-axis direction. Based on the above

discussion, the optimum room temperature ferroelectric response for $BaTiO_3$ occurs when the out-of-plane film growth is *c*-axis oriented.[53,54] In-plane compressive strain (and consequently out-of-plane tensile strain corresponding to an increase in the *c* lattice parameter) has been shown to increase the T_C as well as improve the P_r in $BaTiO_3$.[55]

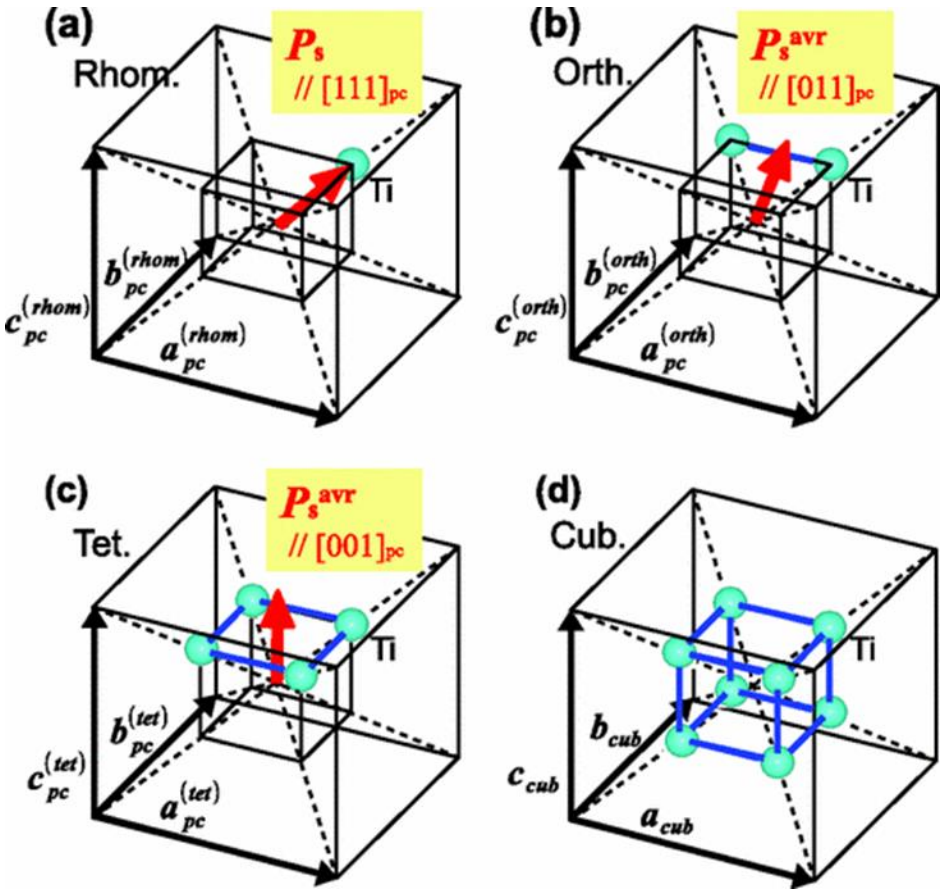

FIG. 1.9 Orientation of the polarization axis for the (a) rhombohedral, (b) orthorhombic, (c) tetragonal, and (d) cubic phases of $BaTiO_3$.[52]

The prospect of incorporating ferroelectric materials into nanoscale capacitor structures has prompted research on the influence of size effects on the dielectric and ferroelectric properties in thin films. Several thickness studies have been performed, both, experimentally and from theoretical calculations, on the decrease of polarization with decreasing thickness, and a complete loss of polarization below a critical thickness in $BaTiO_3$. The reported critical thickness varies from 12 Å to 41.7 Å from the theoretical calculations, and 50 Å from experimental results for $SrRuO_3/BaTiO_3/SrRuO_3$ structures.[56-59] For free standing relaxed $BaTiO_3$ thin films it was found to be 36 Å from first principles calculations.[60] The disappearance of polarization below the critical thickness has been attributed to dipoles quantum effects due to the interaction between the $BaTiO_3$ film and the $SrRuO_3$ electrodes.

Stoichiometry in complex oxide films is a critical parameter because the composition determines the unit cell structure and interaction between the constituent atoms which directly influence the physical and chemical properties of the material. In perovskite oxides, it is very common for the film to be deficient in the lighter elements in the system,[61] which can be modulated by deposition parameters like laser fluence in pulsed laser deposition. It has been shown in $BaTiO_3$ that for lower values of laser fluence, the deposited films are Ba-rich, as seen in Figure 1.10 (a), with a lower *c* lattice parameter, shown in Figure 1.10 (b), compared to films grown at higher values of laser fluence.[62] The corresponding P-E loops in Figures 1.10 (c)-(e) show that the polarization response of the films improves as the Ba:Ti ratio approaches its stoichiometric value.

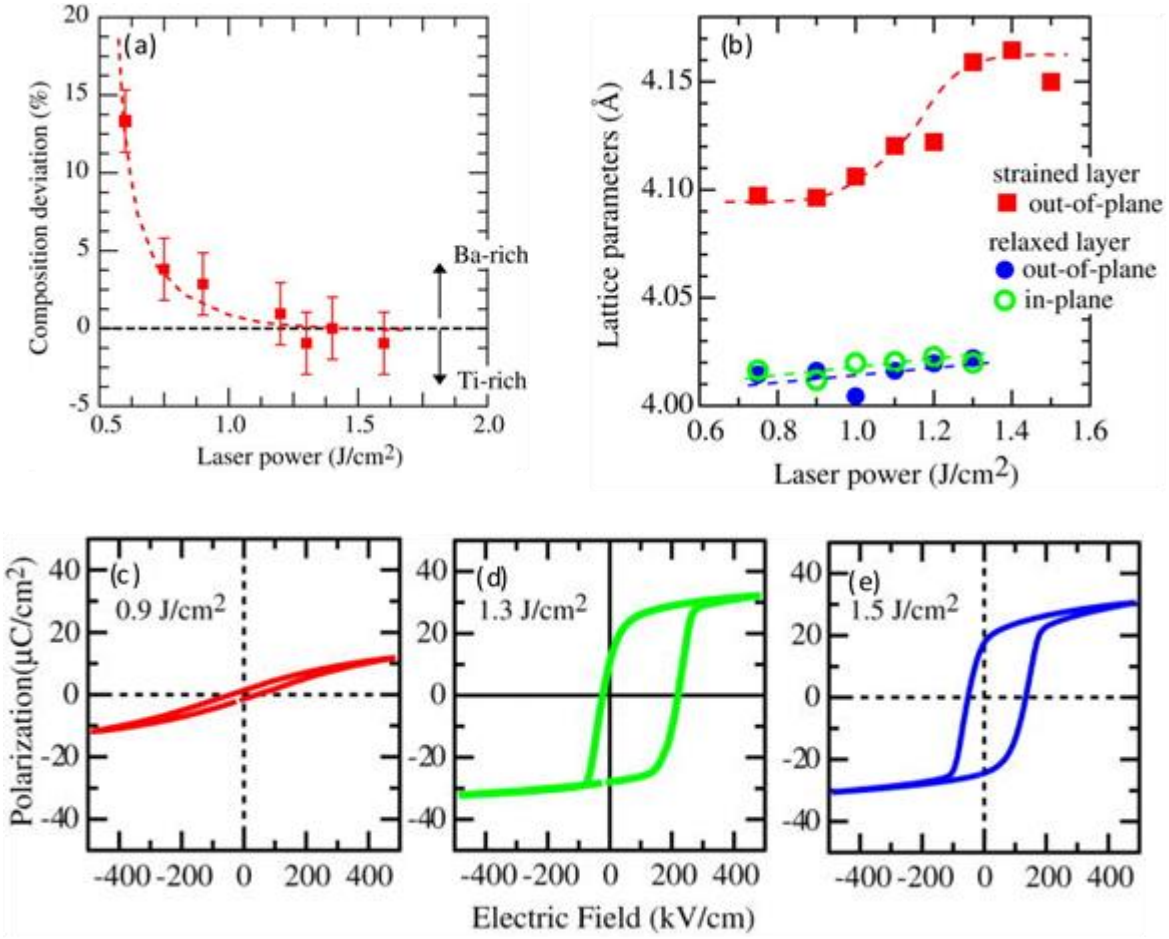

FIG. 1.10 The effect of laser fluence on the stoichiometry and ferroelectric properties of $BaTiO_3$: (a) Ba/Ti ratio and (b) the change in the *c* lattice parameter as a function of increasing laser fluence; P-E loops for films deposited at (c) 0.9 J/cm^2, (d) 1.3 J/cm^2, and (e) 1.5 J/cm^2.[62]

Another important parameter in oxide film growth is the oxygen partial pressure during deposition. For ferroelectric $BaTiO_3$ films, it was found that the Ba/Ti ratio can be modulated by the gas pressure rather than the actual gas species. However, there are

mixed opinions about how the gas pressure affects the film composition. One study reported ideal stoichiometry in films deposited at low pressures less than 7.5 mTorr, Ti deficiency in films deposited in the intermediate range of 7.5-75 mTorr, and Ba deficiency at pressures higher than 75 mTorr.[63] Conversely, another study found that oxygen pressures greater than 75 mTorr yielded Ti-deficient films, very low pressures caused the film to be oxygen deficient.[64] The ideal Ba/Ti and oxygen stoichiometry was achieved at oxygen pressures in the range of 15-75 mTorr.[64] In a more recent work, it was reported that $BaTiO_3$ films are Ba-rich at a low oxygen pressure of 5 mTorr, and Ti-rich at higher pressures.[65] Shown in Figure 1.11 (a), the ideal stoichiometry was achieved at an intermediate pressure of 40 mTorr, which also corresponds to the best P_r values achieved, in Figure 1.11 (b).

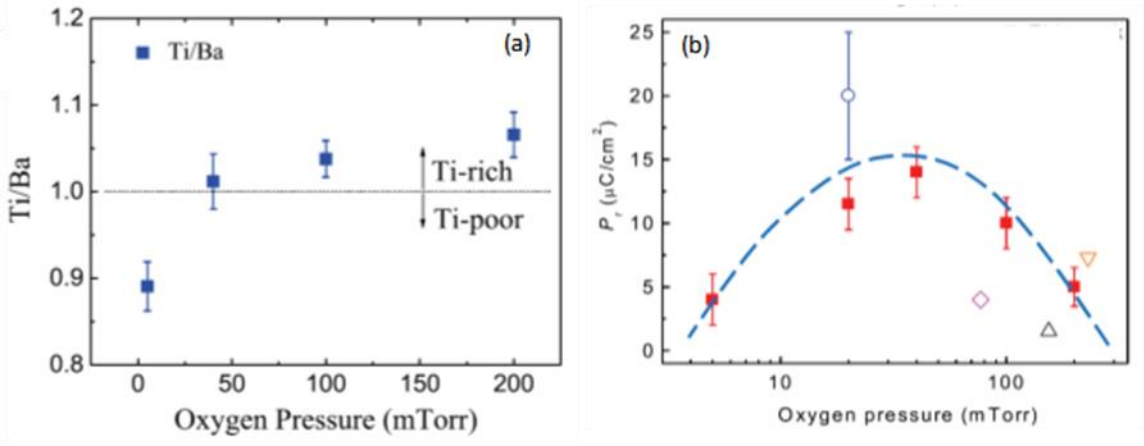

FIG. 1.11 (a) Ti/Ba stoichiometry and (b) P_r in $BaTiO_3$ films as a function of oxygen pressure.[65]

1.1.3.2 Resistive switching

Resistive switching (RS) has been a long observed phenomenon in many metal oxide materials, dating back to almost two centuries.[66] In a RS device, a certain voltage (SET voltage) is required to switch the device from a high resistance state (HRS) (low current state) to a low resistance state (LRS) (high current state), while another voltage (RESET voltage), that may be of a different polarity from SET, switches the device back from the LRS to the HRS. In 1971, Dr. Leon Chua proposed the idea of a fourth circuit element, the "memristor" or "memory resistor, independent of the resistive switching phenomenon. Shown in Figure 1.12 (a), the resistor relates the voltage *v* to the current *i*, the capacitor relates *v* to the electric charge *q*, and inductor relates *i* to the electric flux φ.[67] He theorized, that based on the symmetry of these passive circuit elements, there must be a fourth element that relates *q* to φ, such that

$$\mathrm{d}\varphi = M\mathrm{d}q \tag{1-9}$$

where *M* is the property of memristance with units of Ω.

M is a nonlinear circuit element, and a function of *q*, whose *i*-*v* characteristic is a Lissajous figure shown in Figure 1.12 (b). The voltage drop across the device is zero when no current flows through it. The frequency-dependent response is based on the q-φ nonlinear relationship for a sinusoidal input, and tends to a purely resistive state (shown by a straight line) as the frequency tends to infinity.

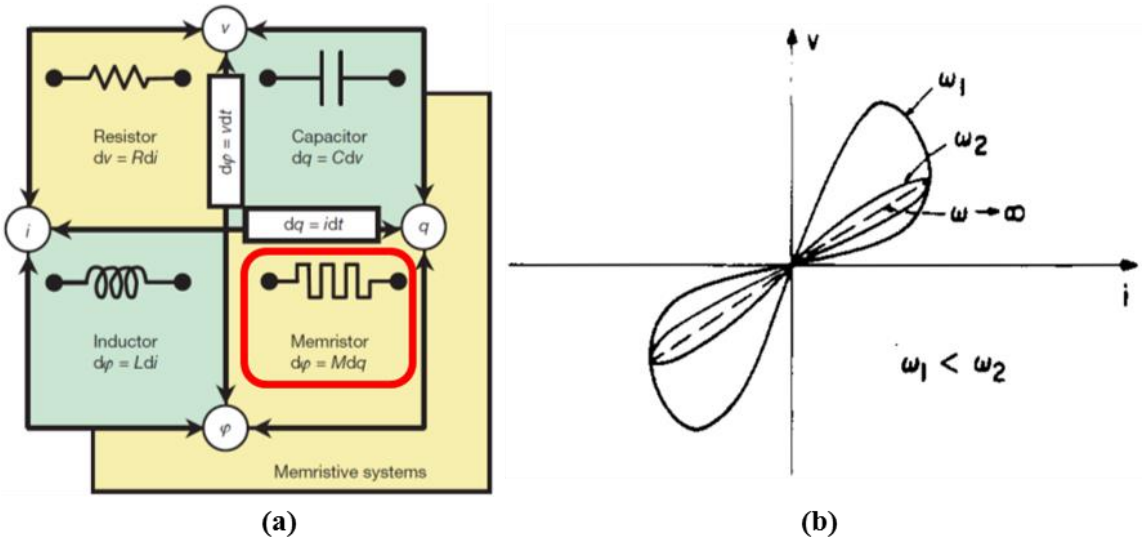

FIG. 1.12 (a) The four basic passive circuit elements. Highlighted is the fourth "missing" element, the memristor. (b) Lissajous figure: frequency response and current-voltage characteristics of a memristive device.[67,68]

The basic current controlled memristive device can be described as

$$v = \mathcal{R}(w, i)i \tag{1-10}$$

$$\frac{\mathrm{d}w}{\mathrm{d}t} = i \tag{1-11}$$

where $\mathcal{R}$ is the resistance dependent on the original internal device state and w is the state variable set.

The memristor is thus a two terminal device that has a resistance state dependent on the past device condition.[68] It was debated that several circuit models should have been more appropriately modeled as memristive systems, including the thermistor (a linear temperature dependent resistor), the ionic systems Hodgkin-Huxley circuit model

(describing the time varying potassium and sodium channel conductances for the nerve axon membrane), and the behaviors of discharge tubes.[68] However, at the time, there was no definite material realization of the memristive property.

In 2008, a group from HP Labs linked this missing memristor device to the resistive switching phenomenon, demonstrating the concept in a TiO_2 thin film device whose current-voltage (I-V) characteristics are shown in Figure 1.13.

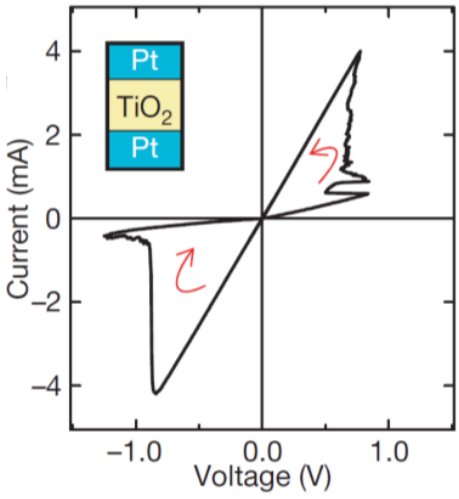

FIG. 1.13 I-V characteristics of the TiO_2 thin film memristive device demonstrated by HP Labs.[67]

As described in Strukov et al.,[67] it was proposed that the observed hysteretic behavior is due to the influence of atomic scale reordering on the current. This model describes a two terminal device in Figure 1.14 (a), consisting of a film of thickness *D* between metal contacts. The some depth *w* of the film has been heavily doped resulting

in a low resistance $\mathcal{R}_{ON}$ in that region, while the remaining film is undoped and therefore has a high associated resistance $\mathcal{R}_{OFF}$, shown in Figure 1.14 (b). $\mathcal{R}_{ON}$ and $\mathcal{R}_{OFF}$ are two variable resistors whose series resistance determines the total device resistance, in Figure 1.14 (c).

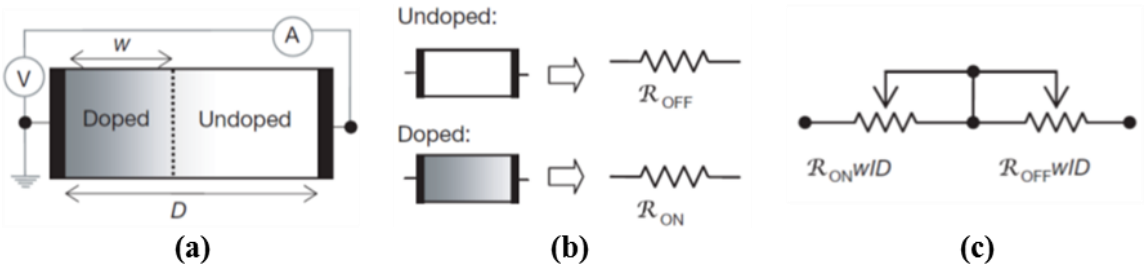

FIG. 1.14 Thin film model of coupled variable resistors: (a) doped and undoped regions of the film, (b) associated resistances, and (c) equivalent circuit.[67]

When a voltage is applied across the device, the dopants will drift in the direction of the field, causing the boundary between the doped and undoped regions to move. Based on linear ionic drift and ohmic electron conduction, and assuming $\mathcal{R}_{ON} \ll \mathcal{R}_{OFF}$

$$v(t) = \left(\mathcal{R}_{ON}\frac{w(t)}{D} + \mathcal{R}_{OFF}\left(1 - \frac{w(t)}{D}\right)\right) i(t) \approx \left(\mathcal{R}_{OFF}\left(1 - \frac{w(t)}{D}\right)\right) i(t) \quad (1\text{-}12)$$

$$\frac{\mathrm{d}\, w(t)}{\mathrm{d}t} = \mu_V \frac{\mathcal{R}_{ON}}{D} i(t) \quad (1\text{-}13)$$

where μ_V is the average ion mobility

$w(t)$ is calculated by integration yielding

$$w(t) = \mu_V \frac{\mathcal{R}_{ON}}{D} q(t) \quad (1\text{-}14)$$

From Equations 1-12 and 1-14, the total *M* is then

$$M = \mathcal{R}_{OFF}\left(1 - \mu_V \frac{\mathcal{R}_{ON}}{D^2}\right) q(t) \tag{1-15}$$

Since this groundbreaking work in 2008, there has been a renewed interest in the field of RS, primary due to the search of a "universal memory device", which would be low cost, high density, high speed, and nonvolatile, and have high endurance and high integration density.[69] The best reported results in RS devices have response times of less than 5 ns, on/off resistance ratios of 10^9, and endurance of more than 10^{12} cycles, and are scalable down to 10 nm, although not all in the same device, indicating that they hold promise in data storage and computing.[70] The primary application is in memory devices in the form of resistive RAM (RRAM) to replace CMOS-based technologies like DRAM, SRAM, and flash, that are approaching their physical and technological limits of scalability.[71] Another application is for logic devices, to improve the efficiency of field programmable gate arrays, using hybrid CMOS/memristor circuits and reduce the integration density.[69] In addition, the memristor closely mimics the behavior of a synapse. Even though CMOS based computing offer superior calculation capabilities, the mammalian brain is far more advanced in adaptive and "learning" abilities like classification, voice and pattern recognition. Hybrid CMOS/memristor circuits could potentially compete with the behavior and complexity of the human brain. Large scale commercialization of RS devices has been hindered by device-to-device variation, reliability, and integration in manufacturing processes, but the main limitation is that in spite of the many hypotheses, theories, and observations, the fundamental principle of RS is still not well understood.

1.1.3.2.1 Classification of switching modes and systems

The basic architecture for most RS cells is a metal-insulator-metal (MIM) structure. There are two switching modes observed, unipolar switching and bipolar switching. In unipolar switching, the resistance change is not dependent on the polarity of SET/RESET voltages. In Figure 1.15 (a), for a device biased in the LRS or "ON" state, a RESET voltage switches the device to the HRS or "OFF" state. The SET voltage has the same polarity as, but a higher magnitude than the RESET voltage, and switches the device to the ON state. This behavior is observed at both voltage polarities. In the case of bipolar switching, shown in Figure 1.15 (b), a (positive) SET voltage switches the device to the ON state and a RESET voltage of the opposite (negative) polarity switches the device back to the OFF state.

RS can be broadly classified into anion-based systems and cation-based systems, and is the result of mobile electrons and ionic species as well as localized electrochemical redox processes. Shown in Figure 1.16 are some important processes and redox reactions involved in resistive switching, though only some may be observed at a time depending on the switching mode and system.[71] The electrodes are designated as M' and M", while the MX represents the ion-conducting or mixed ionic-electronic conducting electrolyte.

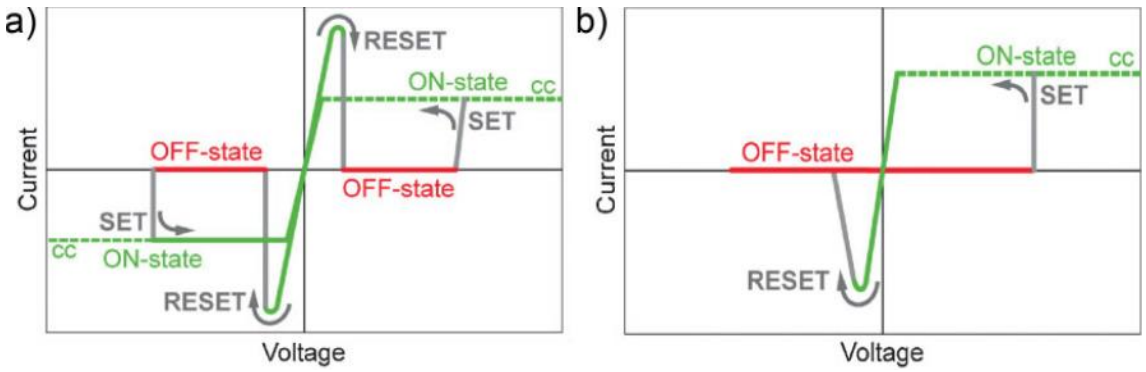

FIG. 1.15 (a) Unipolar switching and (b) bipolar switching.[72]

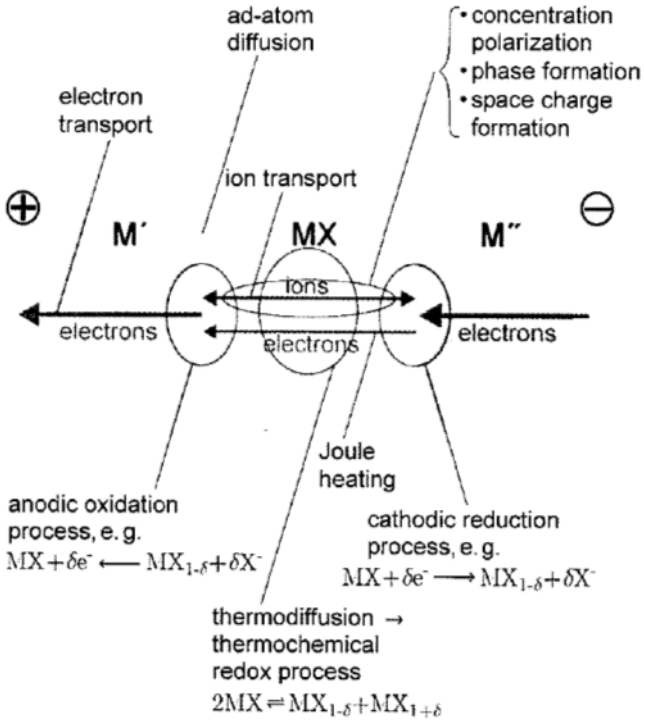

FIG. 1.16 Redox reactions and electrochemical processes involved in RS.[71]

Cation-based systems are electrochemical metallization (ECM) cells, also known as atomic switches, programmable metallization cells, and conductive bridging cells, in which the mobile ionic species are metal ions.[69,72] An ECM cell consists of an ion-conducting solid electrolyte sandwiched between two metal electrodes. The active electrode is made of an electrochemically active metallic material like Cu, Ag, or their alloys, while the counter electrode is made of an electrochemically inert material like Pt, Au, Ir, W, and Ni.[73] Shown in Figure 1.17 is the example of a $Ag/H_2O/Pt$ device.[69] The Ag atoms are oxidized to Ag^+ when a positive voltage is applied to the Ag anode. The Ag^+ cations dissolve in the electrolyte by anodic dissolution and, under the influence of the electric field, drift toward the inert Pt electrode where they are reduced back to Ag atoms and recrystallize on the electrode surface by cathodic deposition. The Ag atoms form dendrites, in Figure 1.17 (a), which grow back toward the anode. At the SET voltage, there is a continuous metal bridge formed between the anode and cathode, switching the device to the ON state, shown in Figure 1.17 (b). A positive voltage is applied to the Pt electrode causes the Ag atoms to get reduced to Ag^+, dissolve, and drift back toward the Ag electrode. At the RESET voltage, the Ag bridge between the two electrodes is ruptured, switching the device back to the OFF state. Though this example describes a case of bipolar switching, unipolar switching is also observed in cation-based devices, where Joule heating due to the high currents in the ON state cause the formed bridge to dissolve or melt.[73]

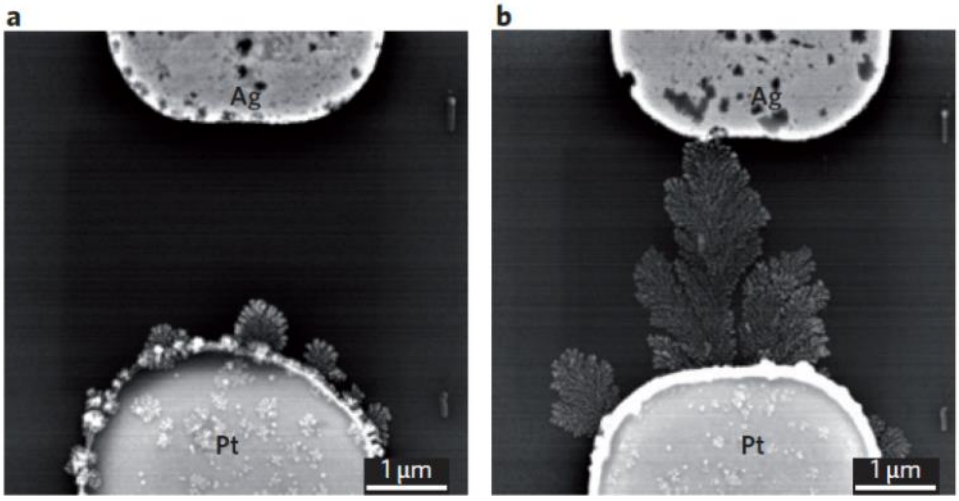

FIG. 1.17 A Ag/H_2O/Pt ECM cell in (a) HRS and (b) LRS.[69]

Most anion-based systems, insulating oxide materials, exhibit RS because rather than the electronic structure of the oxide materials, the RS is driven by defects.[69] The most common defects are Frenkel defects (anion or cation interstitial plus a vacancy) or Schottky pairs (anion and cation vacancy pairs).[4] Anion-based systems, also called valence change systems, include metal oxides and oxide dielectrics, where the mobile species are anions, i.e. oxygen ions and oxygen vacancies.[69] The oxygen vacancy formation reaction can be described in the Kröger-Vink notation as

$$O_O \rightleftharpoons \frac{1}{2}O_2(g) + V_O^{\cdot\cdot} + 2e' \quad (1\text{-}16)$$

where O_O and $V_O^{\cdot\cdot}$ represent oxygen ions and oxygen vacancies.[72]

The vacancy carries a charge opposite to that of the anion, and is thus positively charged. The motion of these charged species causes changes in the valence states of the metal

cations, resulting in a change in the resistance. The mobility μ_{V_0} of oxygen vacancies is described by

$$\mu_{V_0} \sim D_0 \, exp\left(-\frac{W_D}{kT}\right) \tag{1-17}$$

where W_D is the oxygen vacancy diffusion activation energy, k is Boltzmann's constant, T is the temperature, and D_0 is a constant.[74]

Most research on RS has been done on TiO_2 based devices, so it is considered to be a prototype material for this property.[75] In addition, RS has been observed in many other binary oxides including transition metal oxides ZrO_x, MgO_x, HfO_x, AlO_x, VO_x, SiO_x, CrO_x, SbO_x, MnO_x, FeO_x, CoO_x, NiO_x, CuO_x, ZnO_x, GaO_x, GeO_x, NbO_x, MoO_x, TaO_x, and WO_x, rare-earth oxides YOx, CeO_x, GdO_x, NdO_x, PrO_x, EuO_x, DyO_x, LuO_x, and YbO_x, perovskites $SrTiO_3$, $SrZrO_3$, $BaTiO_3$, $BiFeO_3$, $(Ba,Sr)TiO_3$, $(La,Co)MnO_3$, $(La,Sr)MnO_3$, $(La,Sr)FeO_3$, and $(Pr,Ca)MnO_3$, as well as nitrides AlN, SiN, and WN, and chalcogenides Cu_2S, Ag_2S, GeS_x, Ge_xSe_y, ZnSe, and ZnTe.[69,70,76] Typically oxide films for RS are of polycrystalline quality, rather than highly epitaxial. Both unipolar and bipolar switching have been observed in anion-based devices. The two main switching mechanisms observed are filamentary type and interface type switching which will be discussed in further detail in a later section.

1.1.3.2.2 Nonstoichiometry in TiO_2

"Nonstoichiometric" suboxides of TiO_2 (e.g. Ti_4O_7 or $TiO_{1.75}$), PrO_2 (eg. Pr_6O_{11} or $PrO_{1.833}$), Nb_2O_5 (eg. $Nb_{53}O_{132}$ or $NbO_{2.4906}$), have a deficiency in either the cation or anion lattice, resulting in a discrepancy between the number of atoms and the number of available sites in the unit cell.[4,75] These nonstoichiometric oxides are crystalline, well-

defined compounds whose electronic properties are dependent on the magnitude of nonstoichiometry. In TiO_2, Magnéli phases or oxygen deficient phases are of the form Ti_nO_{2n-1}, with phases from Ti_4O_7 to $Ti_{20}O_{39}$ already discovered, and Ti_4O_7 being the most commonly formed.[16,75,77] It has been determined that in TiO_2, oxygen vacancies are the dominant defect type at lower temperatures, while Ti interstitials dominate at high temperatures.[78] The positively charged oxygen vacancies serve as donors in TiO_2, and a sufficiently large concentration of vacancies can lower the Schottky barrier height at the electrode-TiO_2 interface.[16,72]

1.1.3.2.3 Electroforming

Typically, an initial irreversible preconditioning step called the electroforming step is required to initiate RS in a virgin device. The electroforming voltage or forming voltage is of a higher magnitude than the SET/RESET voltages, and is required to cause local depletion of oxygen ions, increasing the concentration of oxygen vacancies. Under a high voltage bias, the negatively charged oxygen ions are attracted to the anode where they accumulate, discharge, and are expelled into the atmosphere, leaving behind positively charged oxygen vacancies which accumulate under the cathode. The higher concentration of the charged vacancies makes the region in which they accumulate more conducting, leading to a reduction of the electric field in that region, reducing the motion of the oxygen vacancies. This gives rise to a "virtual cathode" or an extension of the cathode into the oxide, greatly reducing the effective switching region as shown in Figure 1.18.[72]

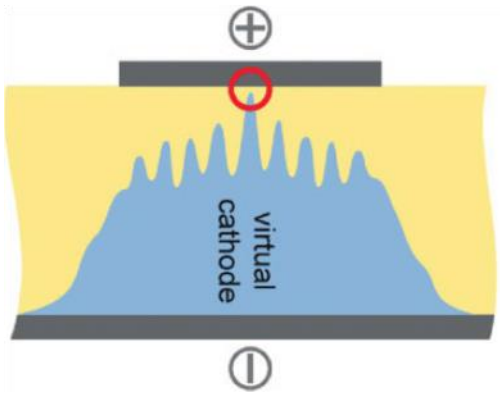

FIG. 1.18 Virtual cathode formed due to the accumulation of oxygen vacancies under the cathode.[72]

The gas expulsion and can cause physical deformation of the device, i.e. delamination and rupture, causing huge variation in device-to-device performance and threatening device integrity.[79] Figure 1.19 (a) shows an AFM image of a virgin device, while Figure 1.19 (b) shows an AFM image of the same device after electroforming. The electroformed device has developed a bubble with a pointed tip under the metal electrode suggesting gas eruption.[79] The forming voltage decreases with decreasing oxide thickness and has been eliminated in films with thickness less than 6 nm.[71,79] Another option is to include an oxygen deficient oxide layer in the oxide stack that would serve as a source of oxygen vacancies.[80]

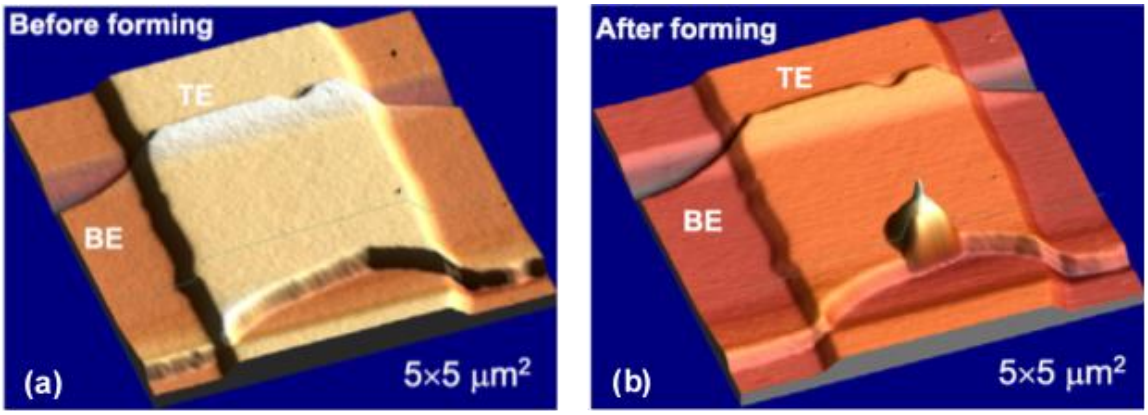

FIG. 1.19 AFM images of (a) a virgin device and (b) the same device after electroforming.[79]

1.1.3.2.4 Filamentary type switching

In filamentary switching, the switching occurs due to the formation and rupture of conducting filaments within the oxide, a thermochemical process, the energy for which is provided by Joule heating due to the current flow.[16] The resistance is limited to resistance of the conducting filament(s) and independent of electrode area.[16] A preliminary electroforming step is required to generate oxygen vacancies in the TiO_2 film.[71] In the SET process, a locally high concentration of oxygen vacancies, generated in the direction of the electric field, leads to the formation of conducting filaments of Magnéli phases. The vacancies preferentially nucleate at the cathodic interface and the conducting filament grows towards the anode. The resultant conducting filament has a conical shape that is broader at the cathode and narrower at the anode.[81] In the RESET process, Joule heating causes the conducting filament to melt and rupture. As the filament cools down, it crystallizes back to rutile or anatase, or to a defective rutile or

anatase $TiO_{2-\delta}$ ($\delta < 0.25$) that is less conducting than the Magnéli phase.[81] Filament formation and rupture has been directly observed by transmission electron microscopy (TEM) and *in situ* TEM studies,[82,83] as shown in Figure 1.20.

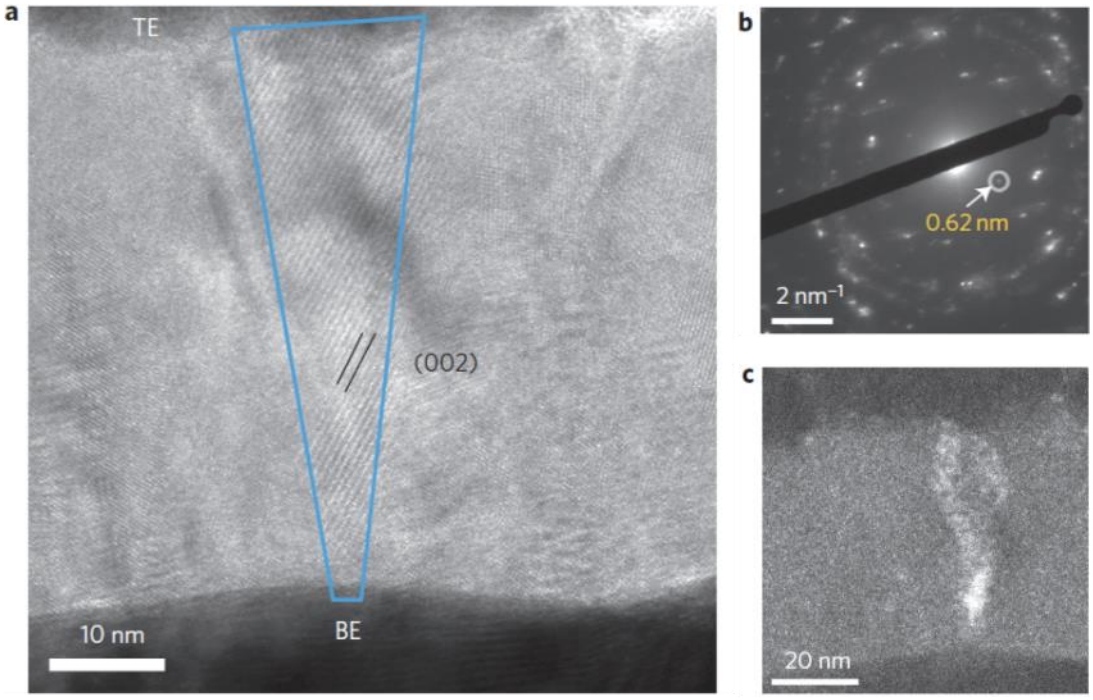

FIG. 1.20 (a) High resolution bright-field TEM image of a conical conducting filament consisting of a Ti_4O_7 Magnéli phase, (b) its corresponding diffraction pattern, and (c) a dark-field TEM image clearly showing the conical filament from the diffraction dot circled in (b).[82]

The filamentary type switching mechanism can give rise to, both, unipolar and bipolar switching. Unipolar switching is always filamentary type. In unipolar switching, the device consists of a metal oxide sandwiched between two inert metal electrodes.[84] In

unipolar filamentary switching, the conducting filament connects the anode and cathode at the SET voltage, resulting in the ON state. The RESET voltage is of a higher magnitude than SET, at which Joule heating causes the filament to melt and rupture. In the case of bipolar filamentary switching, the device is of a similar structure to a unipolar device, except that one electrode is inert while the other has high oxygen reactivity. The preliminary electroforming step creates localized conduction paths within the oxide, doped with oxygen vacancies whose motion is polarity dependent.[84] Figure 1.21 (a) and (b) show the I-V characteristics of unipolar switching and bipolar filamentary switching, respectively.[16]

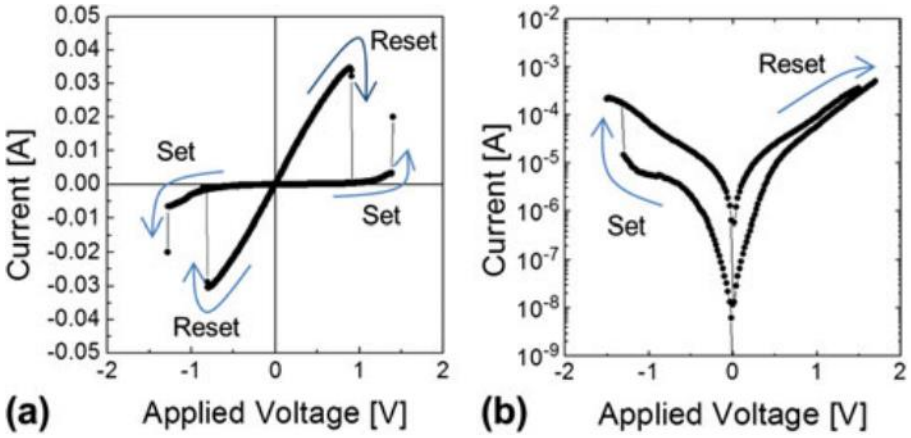

FIG. 1.21 I-V characteristics of (a) unipolar switching and (b) bipolar filamentary switching.[16]

1.1.3.2.5 Interface type switching

In interface type switching, the resistance is inversely proportional to the electrode area. The device consists of a semiconducting oxide whose one electrode forms a Schottky contact (non-rectifying) and second electrode forms an Ohmic contact (rectifying) with the oxide. RS in interface type switching is believed to be driven by the lowering of the Schottky barrier height by the positively charged oxygen vacancies.[71,72] Another theory is that the external bias can change the state of interfacial charge traps at the Schottky junctions, resulting in the collapse (LRS) and recovery (HRS) of the Schottky barrier, shown in Figure 1.22.[70] The rectifying behavior of a Nb-doped $SrTiO_3$ shown in Figure 1.22 (a). In Figure 1.22 (b), a forward bias on the Schottky junction draws out the electrons from the charge traps, while the traps left behind are now positively charged, reducing the built-in potential, putting the device in the ON state or LRS. A reverse bias on the Schottky junction in the ON state injects electrons back into the empty traps neutralizing their charge, resulting in a recovery of the Schottky barrier, putting the device back into the OFF state or HRS. Interface type switching is always bipolar, and exhibits a rectifying I-V behavior, shown in Figure 1.23.[70,84]

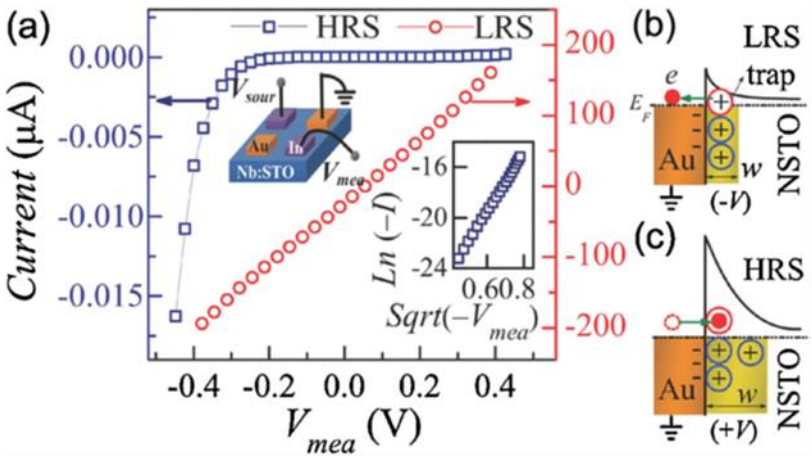

FIG. 1.22 (a) Device schematic and rectifying I-V behavior of a Nb-$SrTiO_3$ device; (b) the drawing out of electrons from the interface charge traps resulting in a collapse of the Schottky barrier and (c) electron injection into the charge traps and recovery of the Schottky barrier.[70]

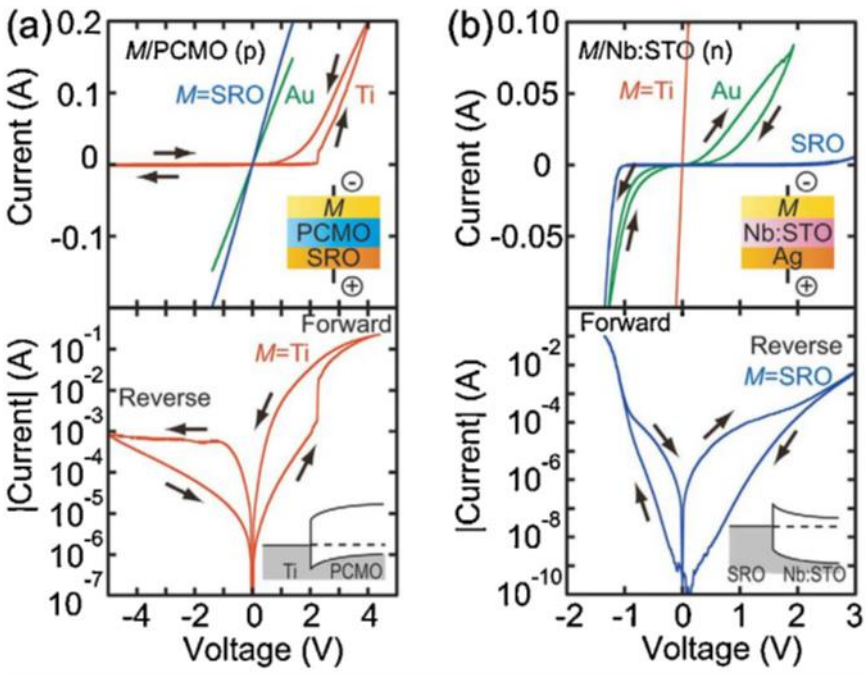

FIG. 1.23 I-V characteristics of (a) Au/$Pr_{0.7}Ca_{0.3}MnO_3$ (p-type)/$SrRuO_3$ and (b) $SrRuO_3$/Nb-doped $SrTiO_3$ (n-type)/Ag bipolar interface type (non-filamentary) switching devices.[70]

1.1.4 Thin film growth

Functional thin films can be grown by a variety of deposition methods. Physical vapor deposition (PVD) techniques include thermal evaporation, e-beam evaporation, magnetron sputtering, pulsed laser deposition (PLD), and molecular beam epitaxy (MBE). Chemical vapor deposition (CVD) techniques include atmospheric pressure CVD, low pressure CVD, metal-organic CVD, and atomic layer deposition (ALD). Additional methods like liquid phase epitaxy and solution based methods like spin-

coating and doctor-blading can also be used. Typically CVD techniques like ALD and PVD techniques like PLD and MBE are used for thin film deposition as they allow for very precise control of the deposition parameters, which can directly impact the film properties.

1.1.5 Epitaxy and strain

Epitaxy, in reference to thin films, refers to the ordered single-crystal growth of a film onto a substrate that, in most cases, is also single-crystal. For epitaxial film growth on a single-crystal substrate, there is typically a certain relationship between the film orientation relative to that of the substrate. Homoepitaxy refers to the case where the film and substrate are of the same material. In heretoepitaxy, the film is of a different material than the substrate. For a film with unstrained lattice parameter a_f grown on a substrate with unstrained lattice parameter a_s, the lattice mismatch f is given by

$$f = 2 \times \left(\frac{a_f - a_s}{a_f + a_s}\right) \tag{1-18}$$

Three modes arise in heteroepitaxial film growth based on the value of f, shown in Figure 1.24. In the lattice matched mode in Figure 1.24 (a), $f \approx 0$ when $a_s \approx a_f$, very similar to homoepitaxy. For $f < 7$ % in Figure 1.24 (b), the film is coherently strained so that the in-plane lattice parameter of the film $a_{f\parallel}$ matches a_s, without relaxation or generation of misfit dislocations. The in-plane strain can be calculated as

$$\varepsilon_{\parallel} = \frac{a_{f\parallel} - a_f}{a_f} \tag{1-19}$$

As a result of the change in the value of $a_{f\parallel}$, the value of the out-of plane lattice parameter is changed to $a_{f\perp}$.The resultant out-of-plane strain is calculated as

$$\varepsilon_{\perp} = \frac{a_{f\perp} - a_f}{a_f} \tag{1-20}$$

Beyond a certain critical thickness, the misfit dislocations form in the film and it transforms from a coherent strained structure to a relaxed incoherent structure. In the third mode, shown in Figure 1.24 (c), f > 7 %, the strain is too large for coherent film growth, resulting in a relaxed lattice mismatched condition. Domain matching epitaxy is a special case where domains of *m* lattice planes of the film are matched to *n* lattice planes of the substrate, resulting in epitaxial growth. Lattice mismatch within the domains then becomes

$$f = 2 \times \left(\frac{ma_f - na_s}{ma_f + na_s}\right) \tag{1-21}$$

where *m* and *n* are integers such that $n = m \pm 1$.

TiN/Si (001) with a large lattice mismatch of 24.6 % has been grown epitaxially by domain matched epitaxy with 3/4 matching of lattice planes along the film/substrate interface.[85] The lattice mismatch for the domain matched condition is reduced to 4 %. Several other examples of domain matched epitaxy have been demonstrated like ZnO/α-Al_2O_3 (0001) with 6/7 matching and AlN/Si (001) with 4/5 matching.

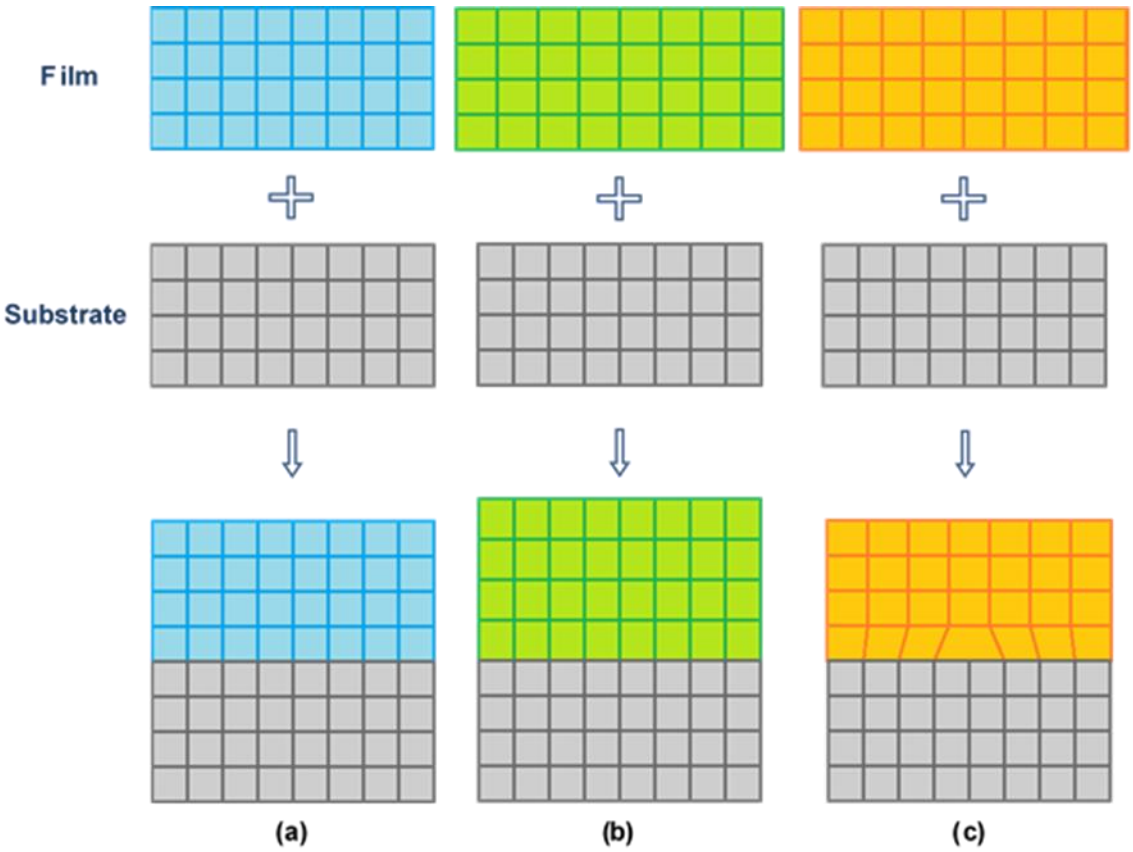

FIG. 1.24 Heteroepitaxial film growth: (a) lattice-matched, (b) coherently strained lattice-mismatched, and (c) incoherent growth-relaxed epitaxy.

1.1.5.1 Strain engineering in thin films

Based on this unavoidable epitaxial strain caused by lattice mismatch and differences in thermal expansion coefficients between thin film materials and the substrates, as well as defects formed during film growth, a unique opportunity presents itself for achieving enhanced functionalities in oxide thin films.[86] Compared to bulk

materials, strains of several percent can be accommodated in thin film material. Strain engineered growth of such materials requires high-quality single-crystal substrates that are suitable, both, structurally and chemically. Strain engineering has been employed in enhancing semiconductor carrier mobility in strained Si_xGe_{1-x} films.[87,88] The paramagnetic to ferromagnetic transition temperature doubled in strained $La_{2-x}Sr_xCuO_4$ thin films.[89-91] In ZnO films grown epitaxially on GaN, the electrical resistivity has been increased with increasing strain, while the optical bandgap becomes wider and narrower for compressive and tensile strain, respectively.[92] Some perovskite and related substrate materials include $SrTiO_3$, $LaAlO_3$, $GdScO_3$, $NdGaO_3$, and $YAlO_3$, shown in Figure 1.25.[93]

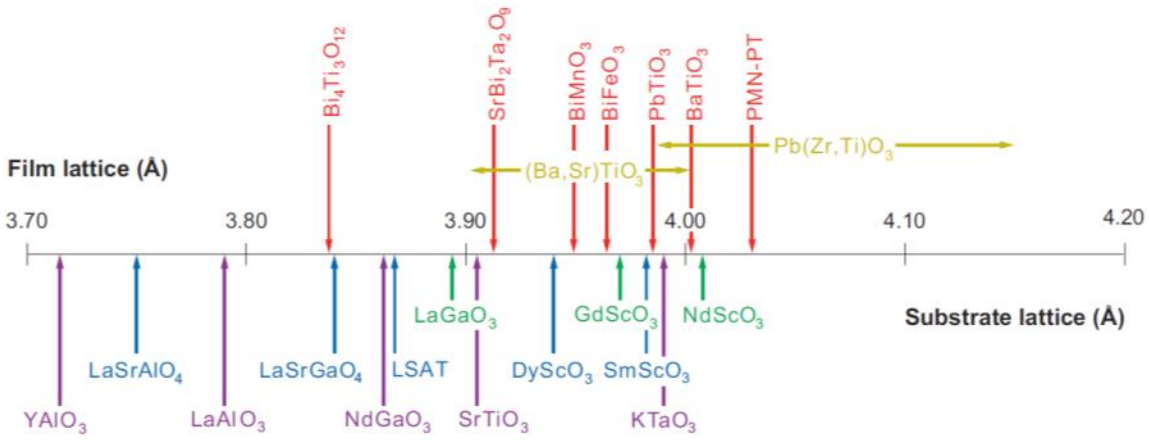

FIG. 1.25 Epitaxial ferroelectric thin films and various perovskite substrates displayed above and below the number line, respectively. The number line represents the pseudocubic/pseudotetragonal *a*-axis lattice constants.[93]

Strained ferroelectric films exhibit superior properties compared to bulk ferroelectric materials. The strong coupling between the polarization and the strain has enabled an increase in the T_C and improvement in polarization in many ferroelectrics, including $PbZrO_3$, $BaTiO_3$, $BiFeO_3$, and $SrTiO_3$.[55,94-96] Phase field simulations of $SrTiO_3$ and $BaTiO_3$ as a function of biaxial strain and temperature show that ferroelectricity in these materials can be modulated by the epitaxial strain.[86,97,98] In the phase diagram for $SrTiO_3$ in Figures 1.26 (a) and (b), it is seen that under high enough tensile strains, the normally room temperature paraelectric $SrTiO_3$ can exhibit room temperature ferroelectricity. For the case of $BaTiO_3$ in Figure 1.26 (c) and (d), the T_C increases from the bulk value of 120 ^oC in an unstrained film beyond 800 ^oC for a 2 % strain.

The P_s in ferroelectric thin films can also be significantly enhanced by epitaxial strain. Shown in Figure 1.27 (a) is the polarization observed in common ferroelectric thin films as a function of epitaxial strain.[99] Compared to other materials, $BaTiO_3$ and $PbTiO_3$ demonstrate a greater sensitivity of the polarization to the strain due to their higher electromechanical coupling in these materials. Coherent epitaxial growth of $BaTiO_3$ thin films on $ReScO_3$ with a compressive biaxial strain as high as 1.7 % exhibited a substantial increase in P_r from the bulk value of 27 $\mu C/cm^2$ to 70 $\mu C/cm^2$, shown in Figure 1.27 (b), as well as an increase in the T_C from 120 ^oC to 500 ^oC.[55]

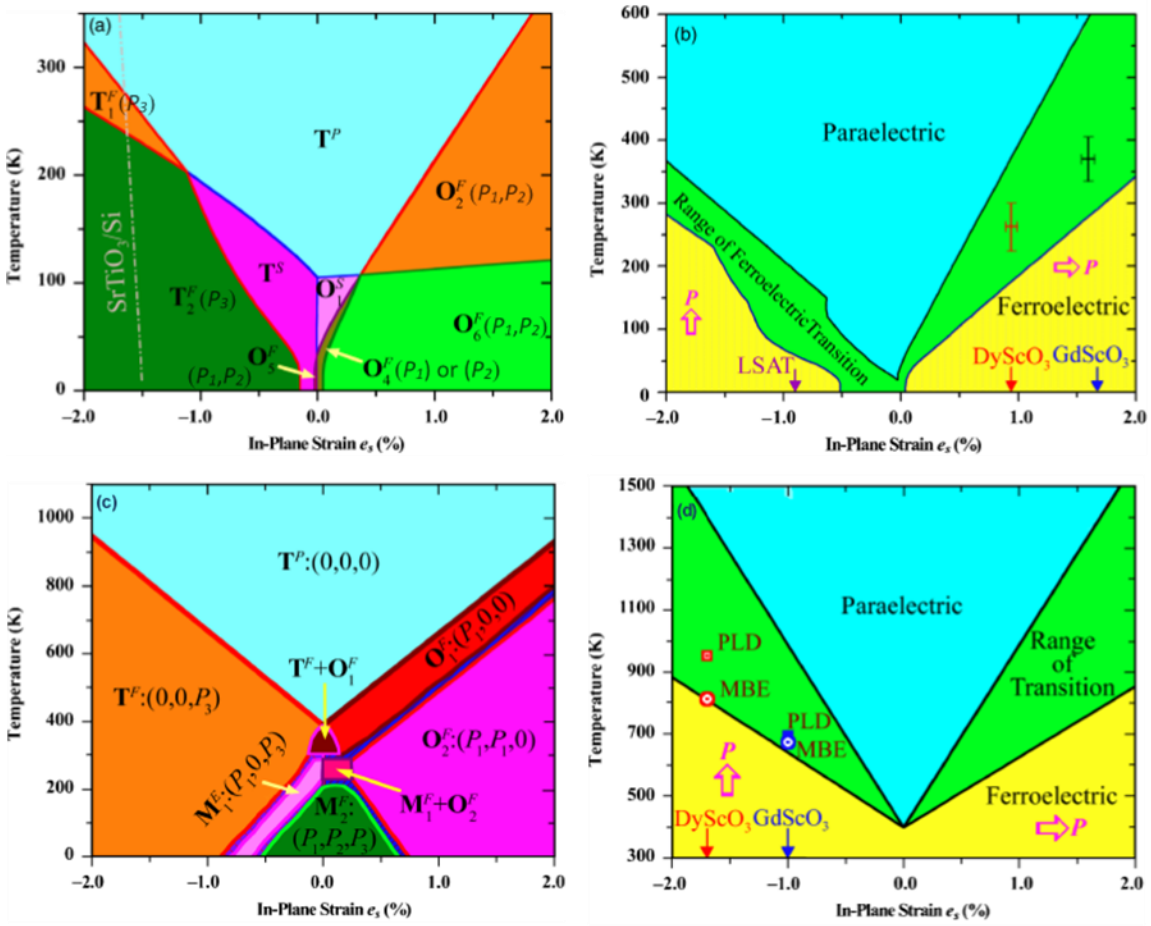

FIG. 1.26 (a) Phase field simulations and (b) simplified strain phase diagram for $SrTiO_3$; (c) phase field simulations and (d) simplified strain phase diagram for $BaTiO_3$.[86]

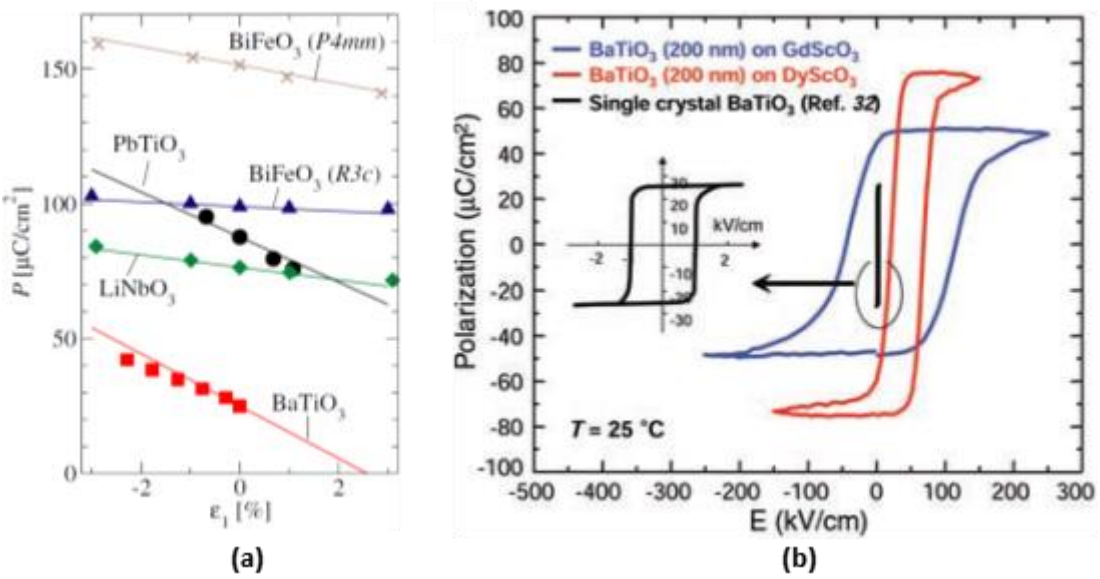

FIG. 1.27 (a) Spontaneous polarization as a function of epitaxial strain common ferroelectric thin films. (b) Polarization hysteresis loops showing the increase in the remnant polarization of $BaTiO_3$ following the increase in epitaxial strain due to growth on different substrate; the inset shows the polarization hysteresis loop for an unstrained bulk $BaTiO_3$ single crystal.[99]

In addition to pure lattice mismatched strain, buffer layers, between the film and substrate, have been employed in heteroepitaxial thin films to reduce the lattice mismatch between the film and the substrate while simultaneously promoting epitaxial film growth.[100] Conversely, they can also be used to introduce strain in the subsequently deposited thin film, which is dependent on the buffer layer thickness. Multilayered structures, of periodic layers of two or more materials, have been shown to improve the dielectric and ferroelectric properties in $Pb(Zr,Ti)O_3$ thin films.[101] An effective method

of strain control, the superlattice structure, is also repeating sequence of two or more materials, but in this case the individual layers thicknesses are on the order of a few nanometers, less than the critical thickness for misfit dislocation formation, as shown in the example of $PbTiO_3/SrTiO_3$ and $BaTiO_3/SrTiO_3$ superlattices in Figure 1.28.[102] In this structure the in-plane lattice parameter is constrained to match that of the substrate, keeping the film completely coherent with the substrate, with the overall properties of the superlattice film is determined by the elastic strain.

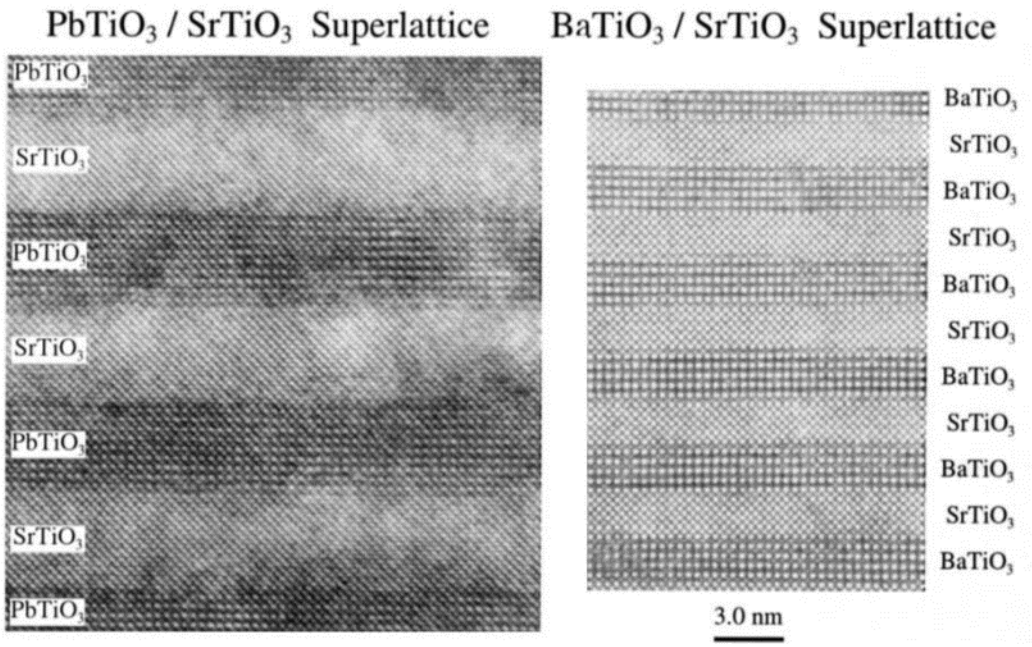

FIG. 1.28 $PbTiO_3/SrTiO_3$ and $BaTiO_3/SrTiO_3$ superlattices.[102]

1.1.6 Vertically aligned nanocomposites

As mentioned earlier, coherently strained epitaxial films begin to form misfit dislocations beyond a critical film thickness, after which the film becomes relaxed and incoherent. This maximum thickness for coherency varies from a few nanometers to a few tens of nanometers, depending on the film material and the growth conditions. However, in some materials, there is a minimum thickness above which it exhibits its particular functionality, e.g., ferroelectricity, making it difficult to tailor the strain in thicker films.[56] A solution to this difficulty is the emergent architecture of vertically aligned nanocomposite (VAN) films, consisting of simultaneously grown two different epitaxial phases on a single substrate. This architecture offers the advantages of the insensitivity of the strain to the film thickness and very large vertical interfaces, over conventional single phase epitaxial strain.

The development of functional oxide thin films is heading in the direction of nanostructured materials consisting of multilayered films, superlattices, nanoscale geometries and features like nanoparticles, nanorods, nanotubes, nanowires, nanorings, and nanoislands.[103-106] VAN systems are a progression in the field of nanoengineering, with concurrent heteroepitaxial growth of two different phases on the same substrate. Shown in Figure 1.29 are three different types of nanostructured thin films.

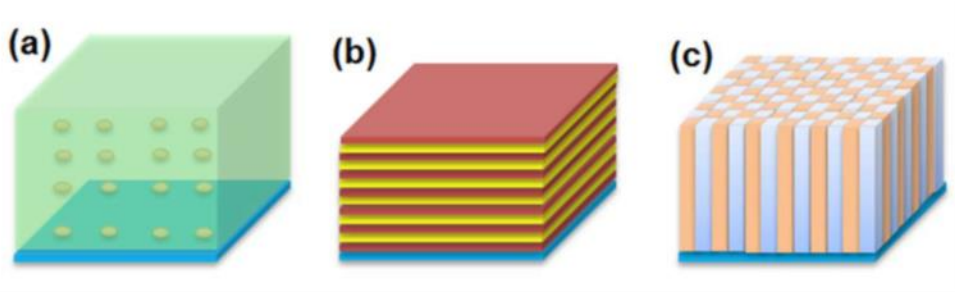

FIG. 1.29 Nanostructured thin films: (a) nanoparticles in a matrix, (b) multilayers, and (c) VAN thin film.

The two-phase nanocomposite system was first introduced in 2002, a composite film of $La_{0.67}Ca_{0.33}MnO_3$:MgO grown by a solution based technique.[107] Tunability of the magnetotransport properties of $La_{0.67}Ca_{0.33}MnO_3$ was reported, attributed to mechanical strain coupling with the surrounding MgO. Following this, a multiferroic system of ferromagnetic $CoFe_2O_4$ pillars in a ferroelectric $BaTiO_3$ matrix was demonstrated using single composite ceramic target by PLD.[108] Shortly after, strain control was reported in a checkerboard structure of $BiFeO_3$:Sm_2O_3 and then in $La_{0.7}Sr_{0.3}MnO_3$:ZnO. Following these pioneering works, several different two-phase systems have been demonstrated,[109] with significant enhancement in their functionalities for variety of applications like multiferroics, spintronics, superconductors, solid oxide fuel cells, and electrically tunable dielectrics.[108,110-115] Summarized in Table 1.4 is a broad summary of reported VAN systems.[116]

Table 1.4 Reported VAN systems.[116]

VAN System	**Crystal Structure**
$BiFeO_3$:Sm_2O_3	Perovskite-rocksalt
$BiFeO_3$:$CoFe_2O_4$	Perovskite-spinel
$BiFeO_3$:$NiFe_2O_4$	Perovskite-spinel
$BiFeO_3$:Nd_2O_3	Perovskite-rocksalt
$BiFeO_3$:Eu_2O_3	Perovskite-rocksalt
$BiFeO_3$:$BaZrO_3$	Perovskite-perovskite
$BaTiFeO_3$:Sm_2O_3	Perovskite-rocksalt
$BaTiO_3$:$CoFe_2O_4$	Perovskite-spinel
$BaTiO_3$: $NiFe_2O_4$	Perovskite-spinel
$BaTiO_3$:CeO_2	Perovskite-fluorite
$La_{0.7}Sr_{0.3}MnO_3$:ZnO	Perovskite-wurtzite
$La_{0.7}Sr_{0.3}MnO_3$:CeO_2	Perovskite-fluorite
$La_{0.7}Sr_{0.3}MnO_3$:Mn_3O_4	Perovskite-spinel
$La_{0.7}Sr_{0.3}MnO_3$:MgO	Perovskite-rocksalt
$PbTiO_3$:$CoFe_2O_4$	Perovskite-spinel
$BaZrO_3$:$YBa_2Cu_3O_{7-x}$	Perovskite-layered perovskite
$BaSnO_3$:$YBa_2Cu_3O_{7-x}$	Perovskite-layered perovskite
$SrTiO_3$:MgO	Perovskite-rocksalt
$LaSrFeO_4$:Fe	Perovskite-body centered cubic
$Ce_{0.9}Gd_{0.1}O_{1.95}$:$Zr_{0.92}Y_{0.08}O_{1.96}$	Fluorite-tetragonal
$Ce_{0.9}Gd_{0.1}O_{1.95}$:$La_{0.5}Sr_{0.5}CoO_3$	Fluorite-perovskite
$Ce_{0.9}Gd_{0.1}O_{1.95}$:$PrBaCo_2O_{5+x}$	Fluorite-double perovskite

1.1.6.1 VAN growth

Some prerequisite conditions should be met for the successful growth of a VAN film. Most importantly, the two component phases must be immiscible, or have limited intermixing. Epitaxial or near epitaxial growth, individually, must be possible for both phases on the substrate. Additionally, both phases should have similar growth kinetics and thermodynamic and chemical stability with the substrate and with respect to each other. Three growth thin film growth modes are possible based on Young's equation for heterogeneous nucleation,

$$\gamma_{sv} = \gamma_{fs} + \gamma_{fv} \cos\theta \tag{1-22}$$

where θ is the wetting angle, γ represents the interfacial energy, while the subscripts *s*, *f*, and *v* denote surface, film, and vapor, respectively. These include Volmer-Weber (island), Frank-Van der Merwe (layer-by-layer), and Stranski-Krastanov (combination of layer/island) growth. Minimizing the free energy of the system, the simplified growth model for a two phase VAN film includes adatom transportation and surface diffusion, followed by agglomeration of like species and island nucleation, and finally, columnar growth, as shown in Figure 1.30.

The microstructure of the resultant VAN film (column width, spacing, and arrangement) is determined by adatom diffusivity on the substrate surface, which is controlled by the deposition parameters, the materials selection of the substrate and component phases, as well as the ratio between the two phases.[117] Different architectures

can be achieved, including, but not limited to checkerboard, circular nanopillar, rectangular nanopillar, and nanomaze structures, as shown in Figure 1.31.

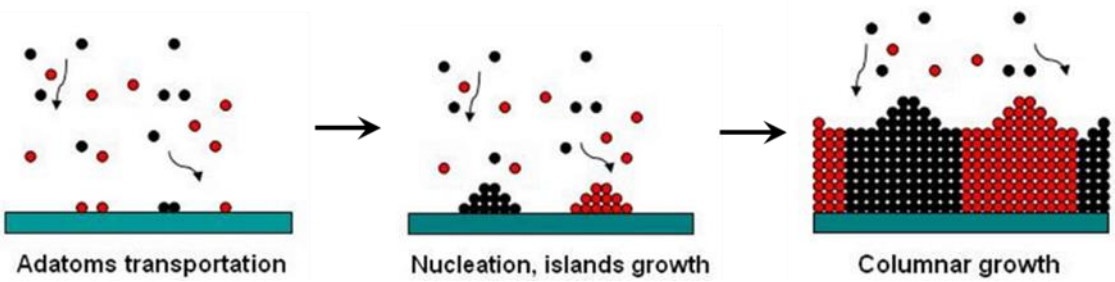

FIG. 1.30 Simplified growth modes for a two phase VAN system.

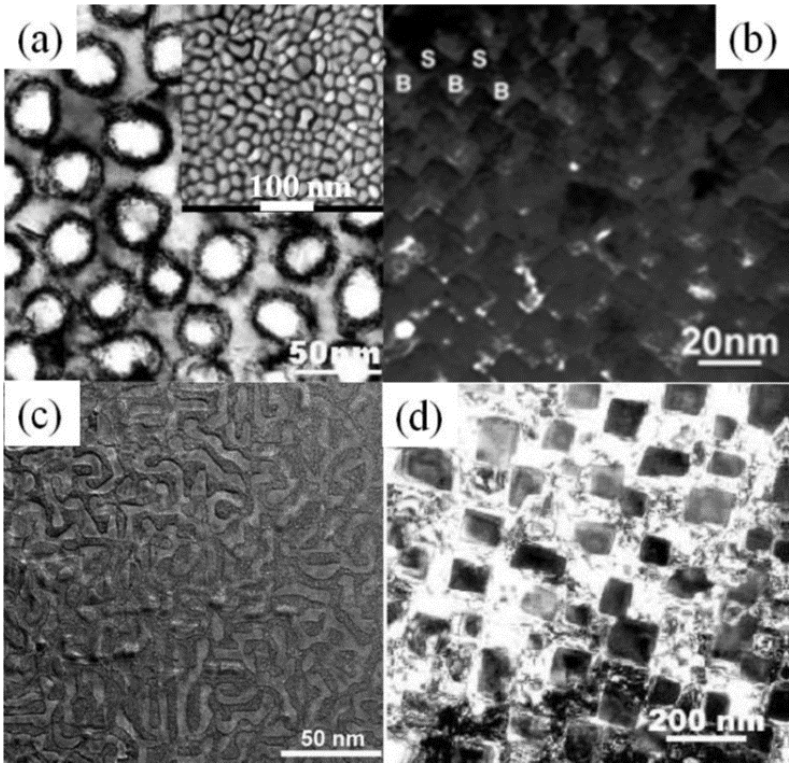

FIG. 1.31 Plan view transmission electron microscopy images of commonly observed VAN structures: (a) circular nanopillar, (b) checkerboard, (c) nanomaze, and (d) rectangular nanopillar.

1.1.6.2 Strain in VAN systems

VAN thin films have two types of strain; horizontal strain induced by the substrate at the film-substrate interface and the vertical strain along the interfaces between the two phases, shown in Figure 1.32.[116] The substrate induced strain relaxes beyond a certain critical film thickness. However, the strain between the two phases in

the VAN system can be tailored by material selection and material composition. The differences in the out-of-plane lattice parameter, crystal orientation, and crystal structure cause one phase to be under tensile strain and the other to be under compressive strain in the vertical direction. The immense sensitivity of the material properties is due to the large ratio of the surface area of the interfaces to the volume of the nanostructure phases.

Figure 1.33 shows the out-of-plane matching relationships between the two phases and the in-plane matching relationships of the individual phases with the $SrTiO_3$ substrates for the $BaTiO_3$-CeO_2 and $La_{0.7}Sr_{0.3}MnO_3$-ZnO VAN systems. In the case of $BaTiO_3$-CeO_2, the out-of-plane lattice parameter is changed to 4.1 Å from the bulk value of 4.036 Å corresponding to an out-of plane tensile strain of 1.6% due to the presence of CeO_2.[118] For $La_{0.7}Sr_{0.3}MnO_3$-ZnO, the $La_{0.7}Sr_{0.3}MnO_3$ out-of-plane lattice parameter is changed from 3.87 Å to 3.89 Å corresponding to an out-of-plane tensile strain of 0.52%.[111] Based on this, the strain in VAN systems can be tuned by selecting appropriate second phase materials. Shown in Figure 1.34 is a diagram with the theoretical out-of-plane strain matching relationship for various coupled two phase VAN structures.[116]

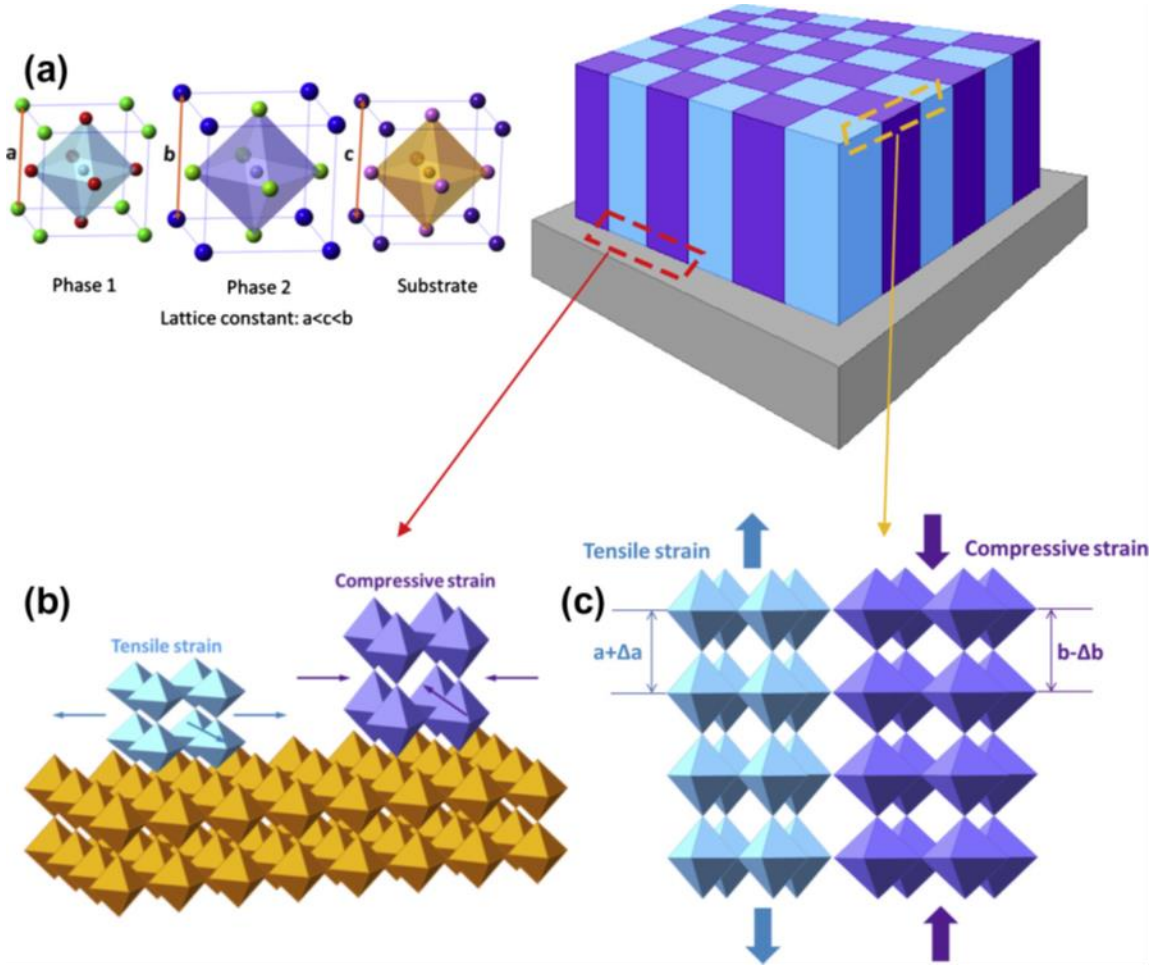

FIG. 1.32 Schematic representation of (a) relaxed unit cells of the substrate and the individual VAN phases; (b) substrate induced strain at the film-substrate interface and (c) vertical strain due to coupling between the two phases in the VAN film.[116]

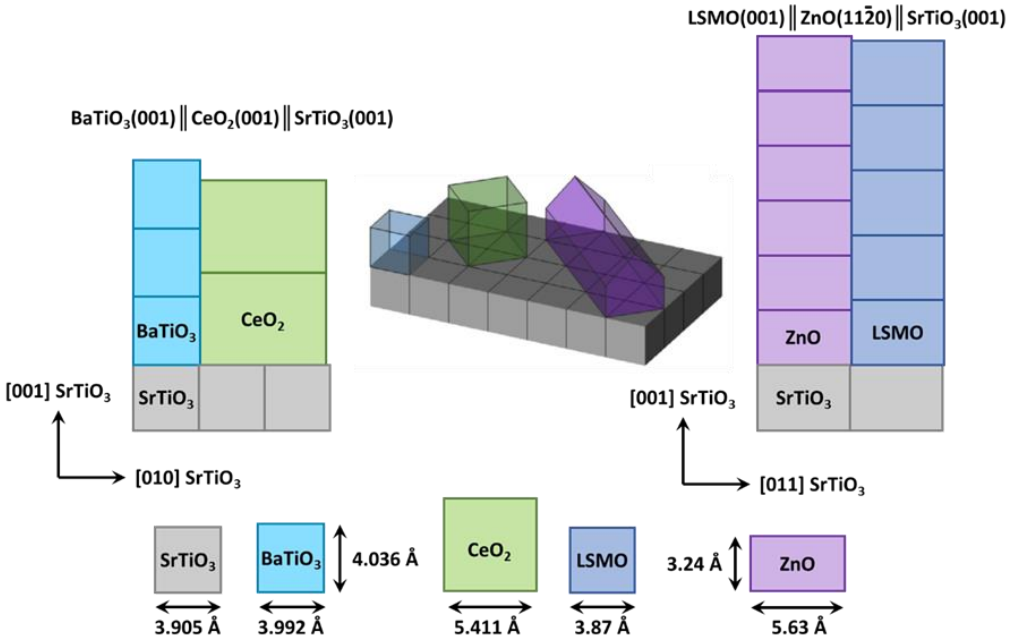

FIG. 1.33 Out-of-plane matching relationships between $BaTiO_3$-CeO_2 and $La_{0.7}Sr_{0.3}MnO_3$-ZnO VAN films grown on $SrTiO_3$ substrates.[116]

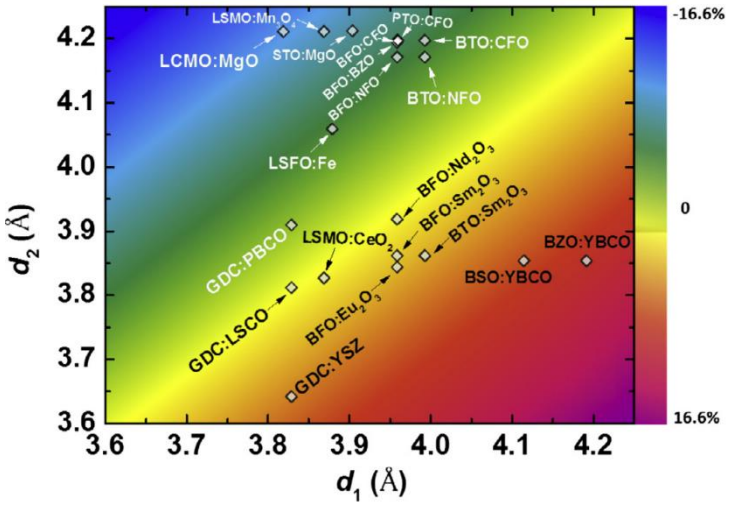

FIG. 1.34 Schematic showing theoretical out-of-plane strain matching relationship for various coupled two phase VAN structures.[116]

1.1.6.3 Property enhancement in VAN systems

Two phase VAN systems using a variety of perovskite materials have been explored for property enhancement. $BaTiO_3$-Sm_2O_3, $BiFeO_3$-Sm_2O_3, $Ba_{0.6}Sr_{0.4}TiO_3$, and $BaTiO_3$-CeO_2 have been used to enhance the ferroelectric response in $BaTiO_3$ by reducing dielectric loss and leakage current and increasing the T_C.[115,119,120] In solid oxide fuel cell applications, a VAN electrolyte of $Ce_{0.9}Gd_{0.1}O_{1.95}$- $Zr_{0.92}Y_{0.08}O_{1.96}$ showed an enhancement in the out-of-plane ionic conductivity,[114] while an interlayer of $La_{0.8}Sr_{0.2}MnO_{3-\delta}$-$Zr_{0.92}Y_{0.08}O_{1.96}$ between the electrode and electrolyte increased the oxygen catalytic properties.[121] Low field magnetoresistance properties have been enhanced in $La_{0.7}Sr_{0.3}MnO_3$-ZnO and $La_{0.7}Sr_{0.3}MnO_3$-CeO_2 due to the out-of-plane strain

induced in $La_{0.7}Sr_{0.3}MnO_3$ by incorporating the second phase.[111,122] The incorporation of $CoFe_2O_4$ as nanoparticles in superconducting $YBa_2Cu_3O_{7-\delta}$, as well as in a VAN buffer layer with CeO_2 has provided a unique approach for analyzing the flux pinning properties in $YBa_2Cu_3O_{7-\delta}$.[113,123] In several instances, two different material properties have been combined for advanced functionalities. A VAN system of $CoFe_2O_4$:$SrRuO_3$ has been shown to reveal a light-induced change in magnetization in the $CoFe_2O_4$.[124] Ferroelectrics are coupled with ferromagnetics for exploration of multiferroic properties like magnetoelectric coupling in $BaTiO_3$:$CoFe_2O_4$,[125-127] and magnetic anisotropy in $BiFeO_3$:$CoFe_2O_4$ systems.[128,129]

1.2 Functional nitride thin films

1.2.1 Overview of refractory nitrides

The term refractory nitrides, also known as transition metal nitrides, refers to the nitrides of Ti, Zr, Hf, V, Nb, Ta, Cr, Mo, and W. They exhibit mixed metallic, ionic, and covalent bonding. Refractory nitrides typically have a f.c.c. B1-NaCl crystal structure, where the nitrogen atoms occupy octahedral interstitial lattice positions, as shown in the case of TiN in Figure 1.35. The filled interstices make for a very hard and very brittle material. The nitrogen atoms are too far apart to bond with each other, and bond very strongly with the metal. The metal atoms, however, are typically large enough to bond with each other, resulting in a strong metallic character, due to which refractory nitrides are sometimes called interstitial alloys.[130] Refractory

nitrides have some very similar physical properties. They are hard, brittle, wear-resistant, chemically inert materials with high melting temperatures, with good corrosion resistance and high electrical and thermal conductivity. Their high melting temperatures are a result of bonding with nitrogen, which stabilize the metal structures. The property differences among the refractory nitrides arise from the differences in their relative sizes and electronegativity.[131]

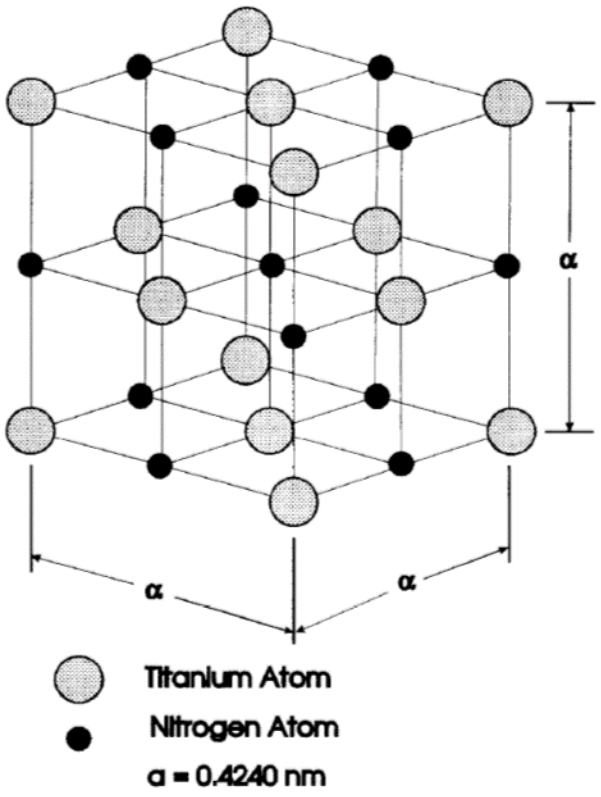

FIG. 1.35 The B1-NaCl structure. Shown is the example of TiN.[131]

1.2.2 Properties of titanium nitride

TiN, a Group IV interstitial nitride, has a broad range of compositions, from $TiN_{0.38}$ to $TiN_{1.18}$.[132] The lattice parameter of TiN has a maximum of 4.24 Å at the stoichiometric composition, and decreases at other TiN_{1-x} nonstoichiometric ratios.[133] TiN has a high melting point of 2950 ºC and a room temperature thermal conductivity of 19.2 W/m-K. Its Vickers hardness and Young's modulus, like other Group IV nitrides, have high values of 18-21 GPa and 251 GPa, respectively, for bulk TiN. These values are higher than those of other nitride groups, rendering it with superior mechanical stability.[133] Even higher values have been reported for TiN in thin film form, 33.58 GPa and 407 GPa for the hardness and elastic modulus, respectively.[134] It is a good electrical conductor with a resistivity of 20-25 μΩ-cm, slightly higher than its parent Ti, and has a work function of 4.09 eV.[133,135] It also has excellent radiation tolerance properties.[136]

1.2.3 Applications of titanium nitride

TiN has been implemented in a variety of protective and, due to its golden color, decorative coating applications. TiN has been successfully used as a coating on the heads of steel cutting and forming tools to improve their wear lifetime.[137,138] In the biomedical industry, it has been implemented as a coating for prosthetics and surgical implements.[139,140] Owing to its excellent erosion and corrosion resistance, it has been proposed as a protective coating in extreme environments.[141,142] Its low electrical resistance and low work function make it a good candidate for transistor gate electrodes,

low barrier voltage Ohmic contacts, and low barrier Schottky diodes. The applications explored in this work will be for diffusion barrier coatings, and buffer layers for heteroepitaxial film growth and integration of functional oxide thin films on Si.

1.2.3.1 Diffusion barrier

TiN has been used extensively in the semiconductor industry as a reliable diffusion barrier and adhesion promoter between Al interconnects and the underlying active areas in the Si substrate. However, with the change of the interconnect metal to Cu due to miniaturization of CMOS technologies, barrier layers thicknesses were reduced to below 20 nm.[143] The formerly excellent TiN-based diffusion barriers were found to fail through a metallurgical reaction with Cu at 350 ^{o}C and by diffusion along grain boundaries within the TiN film. In the past few years, however, there has been a renewed interest in TiN diffusion barriers as further miniaturization of semiconductor chips has moved in the direction of three dimensional technologies like through-silicon-via (TSV), self-aligned TSV, and wafer-on-wafer, which enable device wiring through the chip, rather than along the edges.[144-146] Another proposal on the horizon is the integration of multiple functionalities, including magnetic materials, MEMS components, and high-capacity thin film Li-ion batteries onto a single chip.[144,147,148] Vias in TSV are high aspect ratio trenches with depth to width dimensions on the order of 100:10 μm that are subsequently filled with Cu for vertical wiring and stacking of the chips. TiN is a potential candidate material for a diffusion barrier layer preventing diffusion between the Si wafer and the Cu due to the lower processing temperatures (less

than 200 ^{o}C) and greater thicknesses (~ 50 nm) of the barrier layer. TiN diffusion barrier layers deposited by CVD, with thicknesses ranging from 30 nm to 70 nm have excellent step coverage and show promising results preventing Cu and Li diffusion in Si up to temperatures of 700 ^{o}C.

1.2.3.2 Buffer layer for silicon integration

The epitaxial growth of functional oxide films, especially VAN systems, requires high quality and very expensive single-crystal substrates like $SrTiO_3$, MgO, and $LaAlO_3$, which can significantly drive up the cost of fabrication. There is thus a great need for future integration of oxide based materials and devices, including the new VAN architectures, with conventional Si-based CMOS technologies. It is also more economically desirable to use Si, the workhorse of the integrated circuit fabrication industry with its long established processing systems and vast knowledge base, as the basis for growing these VAN films. However, the epitaxial growth of functional oxides on Si posed significant challenges as the oxygen rich growth atmosphere for oxide growth oxidizes the Si surface and leads to poor growth quality. For example, the epitaxial growth of $BaTiO_3$ directly on Si requires highly controlled expensive deposition techniques like MBE or ALD.[54,149,150] Moreover, significant interdiffusion and intermediate phase formation is observed in the direct growth of $BaTiO_3$ on Si.[151] A $SrTiO_3$ layer could be grown epitaxially on Si to improve the quality of the $BaTiO_3$,[152,153] but again, MBE is needed for substrate-like quality.[154] It was demonstrated that a thin TiN seed layer deposited by PLD could promote the growth of

single crystal substrate like $SrTiO_3$ on Si.[155] Other high quality films of materials like diamond, $Mg_{0.1}Zn_{0.9}O$, and ZnO have also been grown on Si using a TiN buffer layer.[156-159] The double layer $SrTiO_3$/TiN buffer has been implemented for integration of functional oxides like $L_{0.7}C_{0.3}MnO_3$,[160] and VAN systems like $La_{0.7}Sr_{0.3}MnO_3$-ZnO and $BaTiO_3$-CeO_2 on Si, with properties comparable to films grown on single crystal STO.[112,118]

CHAPTER II

RESEARCH METHODOLOGY

2.1 Pulsed laser deposition

PVD techniques are thin film deposition methods that involve the condensation of vaporized materials from a target onto the intended substrate in a vacuum chamber. PLD is a PVD technique that uses a high energy laser as the energy source for the deposition. Shown in Figure 2.1 is the schematic of a PLD chamber. The PLD system consisted of a vacuum chamber houses a mount for the target, typically a multiple target carousel with rotating target mounts, and a heated substrate holder. The laser beam is incident on the target surface at an angle of 45^{o}, while the substrate holder is positioned 4-5 cm directly in front of the target. The focused laser beam on the target surface causes local melting and vaporization. The interaction between the laser beam and the vapor gives rise to a plasma or plume that grows out toward the substrate holder. The thin film is grown on the substrate by the condensation of the vaporized target material.

The film quality is controlled by deposition parameters such as laser energy density, pulse repetition rate, substrate temperature, target-substrate distance, working gas partial pressure, and gas species.

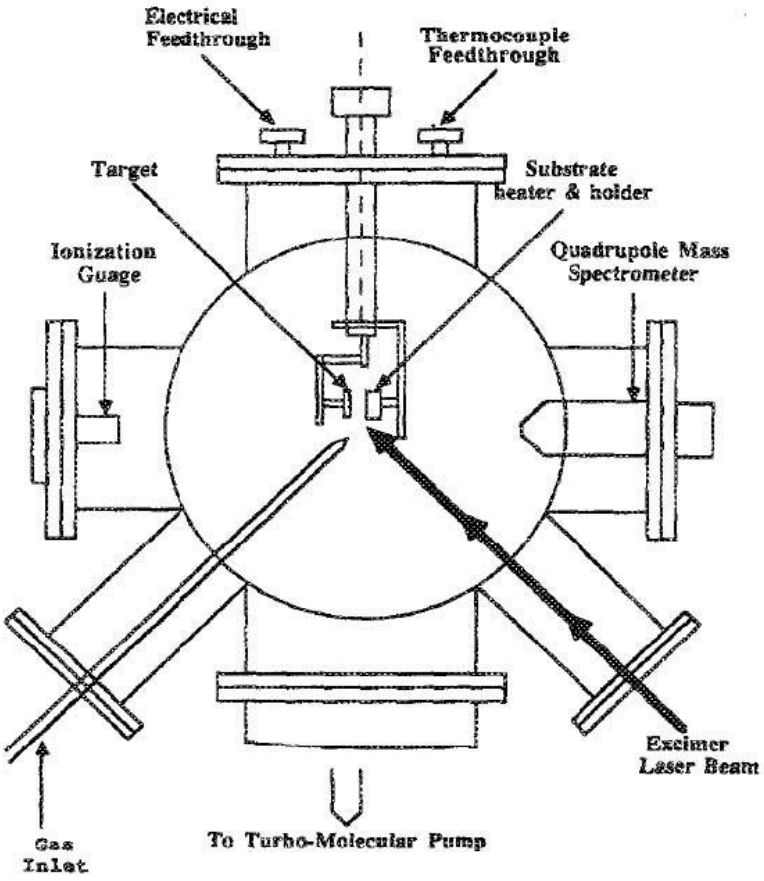

FIG. 2.1 Schematic of a pulsed laser deposition system.[161]

Typical wavelengths for PLD laser sources are in the deep ultraviolet to blue range (~200-400 nm). Common laser sources include excimer lasers and solid-state lasers like neodymium-doped yttrium aluminum garnet lasers, with excimer lasers being more popular. The excimer laser is a gas-based laser system which produces high energy radiation through the dissociation of excimer molecules formed by excitation of their component gases. The excimer laser gas is a mixture of a noble gas (Ar, Kr, Xe) and a halogen (F or Cl). The output wavelength of the laser depends on the specific gas

species; ArF, KrF, XeCl produce wavelengths of 193 nm, 248 nm, and 308 nm, respectively. Optical components, including mirrors, apertures, and lenses, are used to direct and focus the beam. For thin film deposition, the laser is typically operated in a pulsed mode, with a pulse duration of 20-25 ns, rather than continuous to better control the film growth.

For a laser beam incident on a target, the interaction between the two can be divided into three stages.[161,162] Shown in Figure 2.2 (a) is a schematic explaining the laser-target interaction. Figure 2.2 (b) shows the laser beam incident on a target. The first is the interaction of the laser beam with the target material, and is highly dependent on the laser beam and the target material. The electromagnetic energy is absorbed by the target surface and first converted to electronic excitation and then into thermal, chemical, and mechanical energy, with localized temperatures greater than 2000 K, causing melting, evaporation, ablation, excitation, and exfoliation of the target material. The second stage is the interaction between the laser beam and the evaporated material, which forms a plasma or plume as the target continues to absorb energy. The plasma, which consists of mixture of energetic species including small particles, molted globules, clusters, molecules, atoms, ions, and electrons, begins to isothermally expand outward while being supplemented by evaporated material. The first two stages begin at the start of the laser pulse and last through its duration. The third stage, anisotropic adiabatic plasma expansion, occurs immediately after the laser pulse ends. This adiabatic plasma expansion results in deposition onto the substrate. The ablated materials are deposited onto the substrate surface where they nucleate and grow.

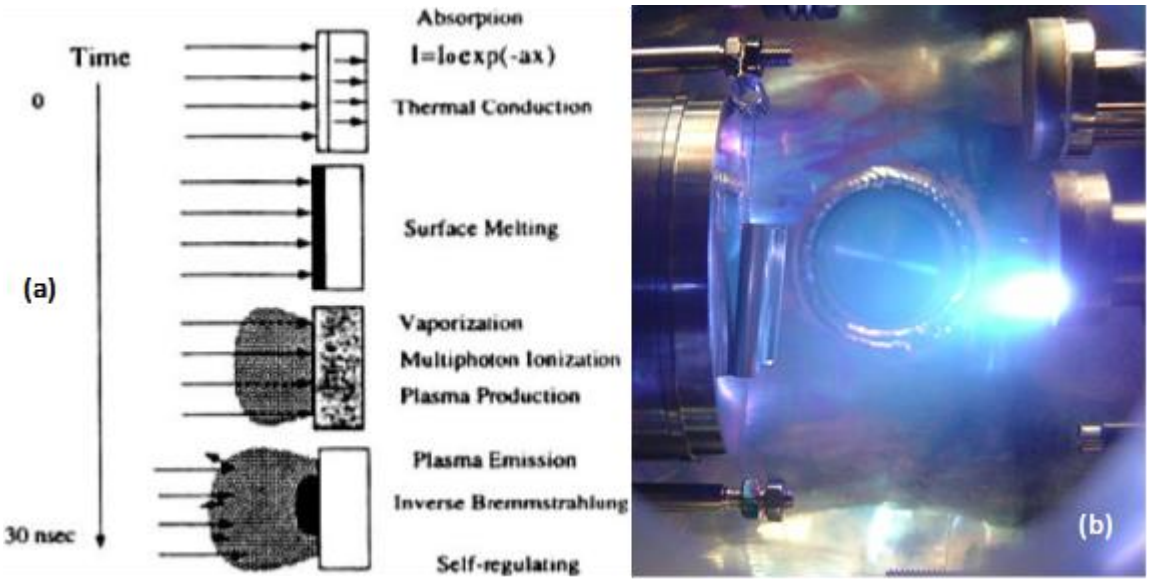

FIG. 2.2 (a) Schematic of laser-target interactions, (b) laser pulse on the target and plasma formation during deposition.

2.2 Material properties

2.2.1 X-ray diffraction

X-ray diffraction (XRD) is a non-destructive analytical technique that is used to identify the structure and chemical composition of crystalline materials. It can also be used to determine the crystal orientation, crystallite size, and stress in single crystal, powder, and thin film specimens.[41] Diffraction, or Bragg diffraction, is the scattering of light in crystalline structures, whose wavelength is on the same order of magnitude as the spacing of the crystal planes, and occurs due the interference between the light waves

as they reflect from the crystal planes, shown in Figure 2.3. For a coherent incident x-ray beam with wavelength λ with incident angle θ, the path length difference between diffracted rays from consecutive planes with interplanar spacing d must vary by an integral number of wavelengths for constructive interference, i.e. $n\lambda$. Thus the path length difference is given by Braggs' Law as

$$n\lambda = 2d \sin\theta \tag{2-1}$$

where n is a whole number.

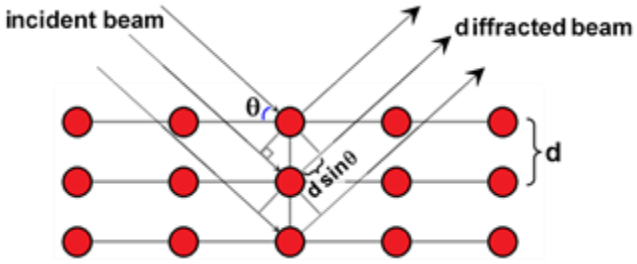

FIG. 2.3 Bragg diffraction for a set of crystal planes with interplanar spacing d.

As the incident angle θ is varied, the Bragg diffraction is satisfied for certain crystallite orientations in a polycrystalline sample. For an x-ray source of known wavelength, the angle of the diffracted beam is measured, from which the interplanar spacing d can be calculated. This is the most basic form of XRD measurement and analysis, referred to as powder diffraction. Thin film diffraction is a set of advanced XRD techniques for characterizing thin film samples of epitaxial or highly textured quality to determine the lattice constant, epitaxial quality, defects, texture, mosaicity, and surface roughness in

thin film materials lattice constant, lattice distortion,. Shown in Figure 2.4 are the geometry and tilt axes of a thin film diffractometer.

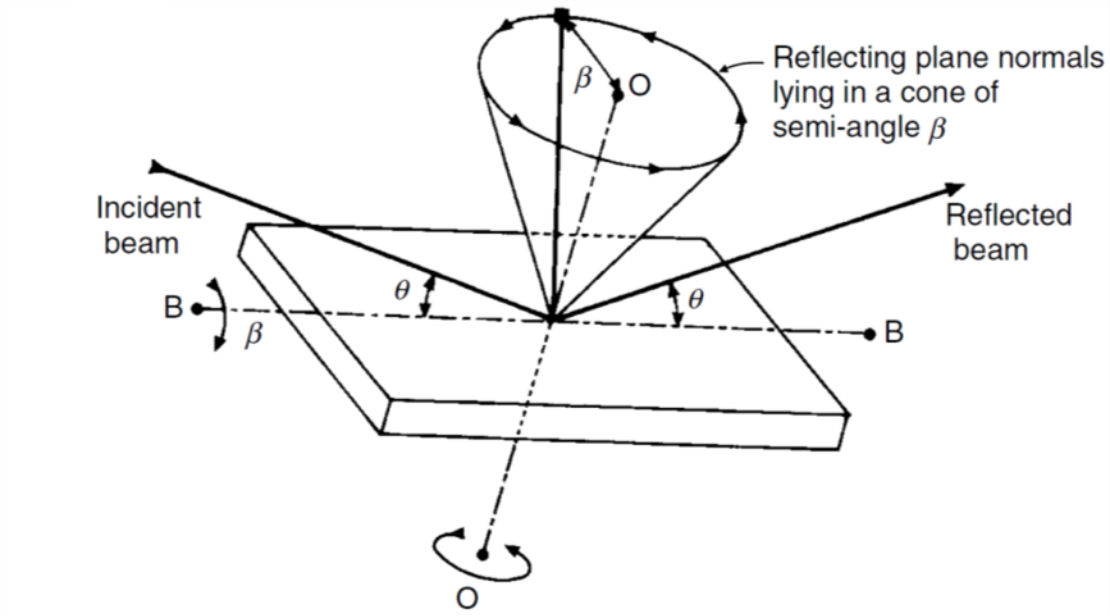

FIG. 2.4 Geometry and tilt axes of a thin film diffractometer.[41]

2.2.2 Transmission electron microscopy

TEM is a powerful tool for characterization of materials that offers information on sample morphology, crystallography, as well as chemistry sub-nanometer resolution. It is a microscopy technique that is similar to optical microscopy, but in this case, information is obtained from the interaction of an electron beam as it is transmitted

through an ultra-thin sample (~ 100 nm). The resolving power or spatial resolution of an imaging device is given by the Rayleigh criterion as

$$R = \frac{0.61\lambda}{n\,sin\alpha} \tag{2-2}$$

where λ is the wavelength of the light, n is the refractive index of the lens, and α is the half angle of the maximum cone of light that can enter or exit the lens. The product $n\,sin\alpha$ is also referred to as the numerical aperture of the lens.

The spatial resolution in conventional optical microscopes is limited by the minimum visible wavelength. The TEM uses an electron beam as the illuminating species rather than photons, enabling far greater resolution owing to the significantly shorter wavelength of electrons, by several orders of magnitude. The wavelength λ in nm of an electron beam at an accelerating voltage V is given by

$$\lambda = \frac{1.22}{\sqrt{V}} \tag{2-3}$$

Typically, an accelerating voltage of 200 kV is used, resulting in an electron beam wavelength of 0.0027 nm.

Shown in Figure 2.5 is a block diagram of a TEM. A typical TEM consists of four main components: the electron source, the system of electromagnetic lenses, the sample stage, and the image acquisition systems, all of which are housed in a high vacuum column. The electron source consists of an electron gun, extraction, and acceleration optics to ensure a parallel, single wavelength beam. The condenser lens system provides illumination to the specimen, while the objective, intermediate, and projector lenses as well as their associated apertures are used for focusing and

magnification of the image onto a viewing screen or an image acquisition system. The TEM has two basic modes of operation; namely the diffraction mode and the imaging mode, shown in Figure 2.6 along with the imaging optics in the TEM. Either mode can be selected by changing the focal length of the intermediate lens. In the diffraction mode, the image plane coincides with the back focal plane of the objective lens, while in the imaging mode, the image plane coincides with the image plane of the objective lens.

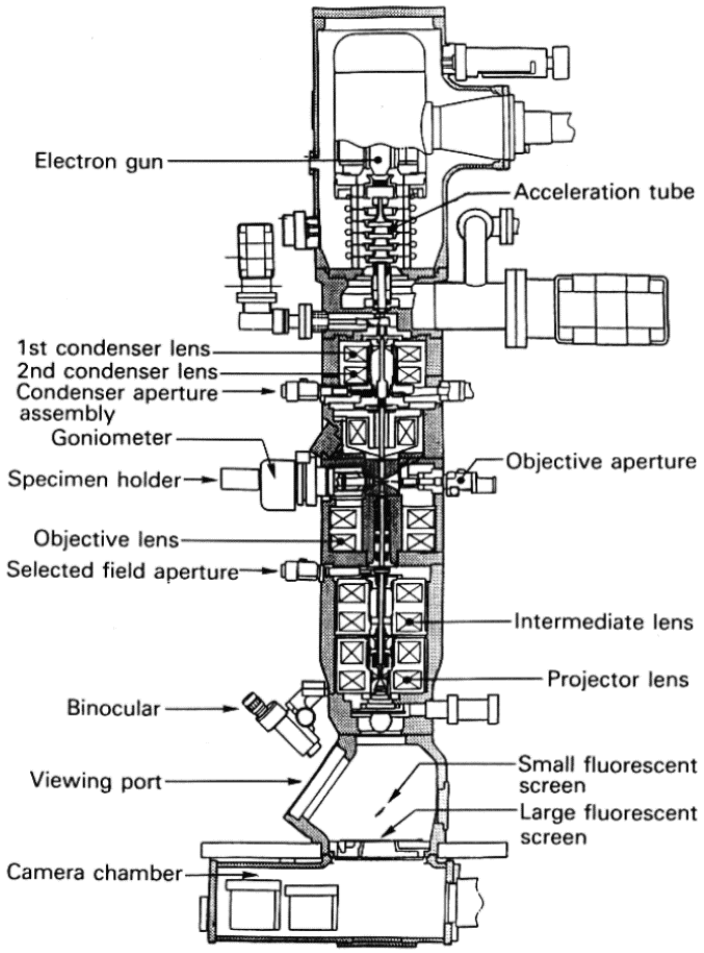

FIG. 2.5 Block diagram showing the layout and major components of a TEM.[163]

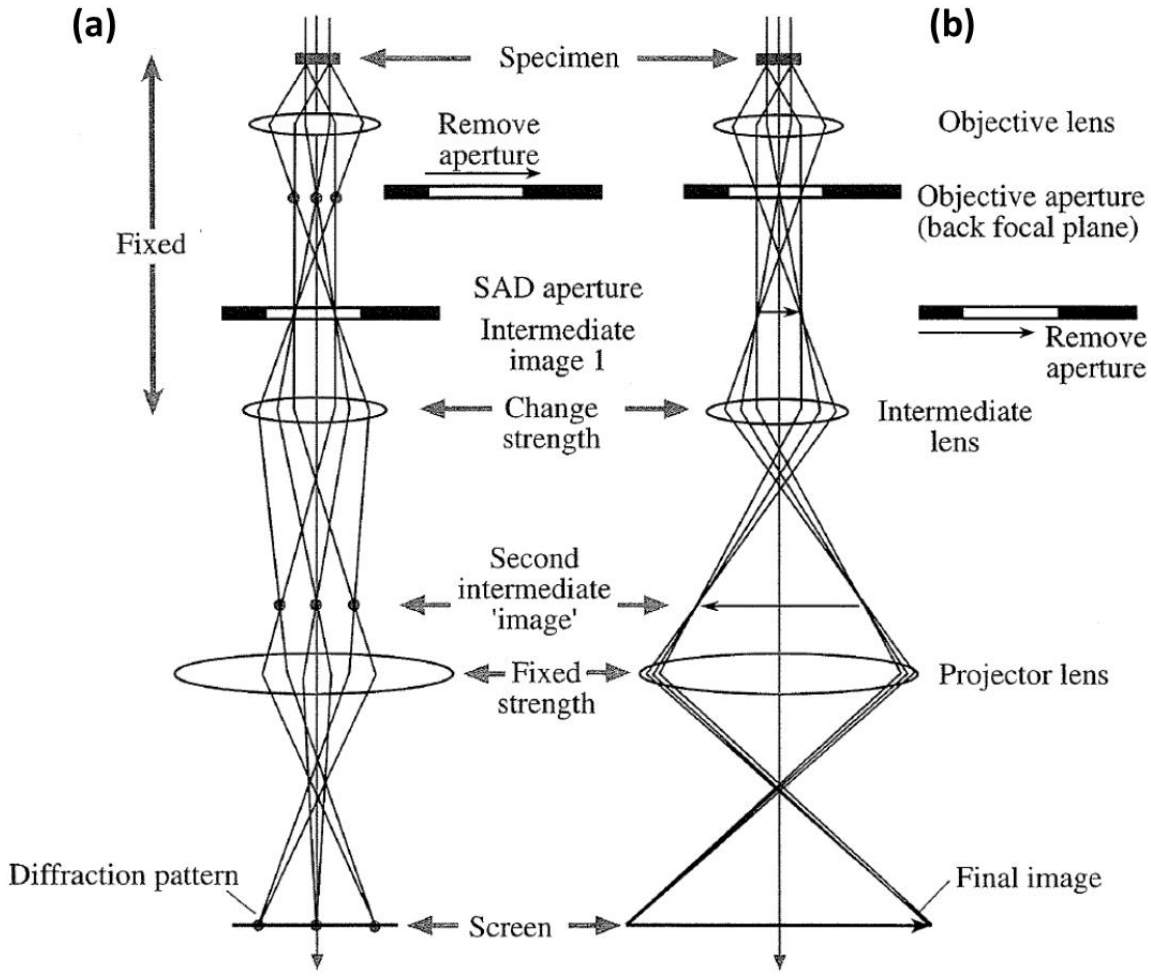

FIG. 2.6 The two basic modes of operation in a TEM: (a) diffraction and (b) imaging.[164]

The contrast of the imaging mode can be improved by inserting appropriate objective apertures at the back focal plane of the objective lens, allowing only certain regions of the diffraction pattern to pass through. When only undiffracted electrons are allowed to pass, a bright-field image is formed, shown in Figure 2.7 (a); when only certain diffracted electrons are allowed, a dark-field image is formed, shown in Figure 2.7 (b).

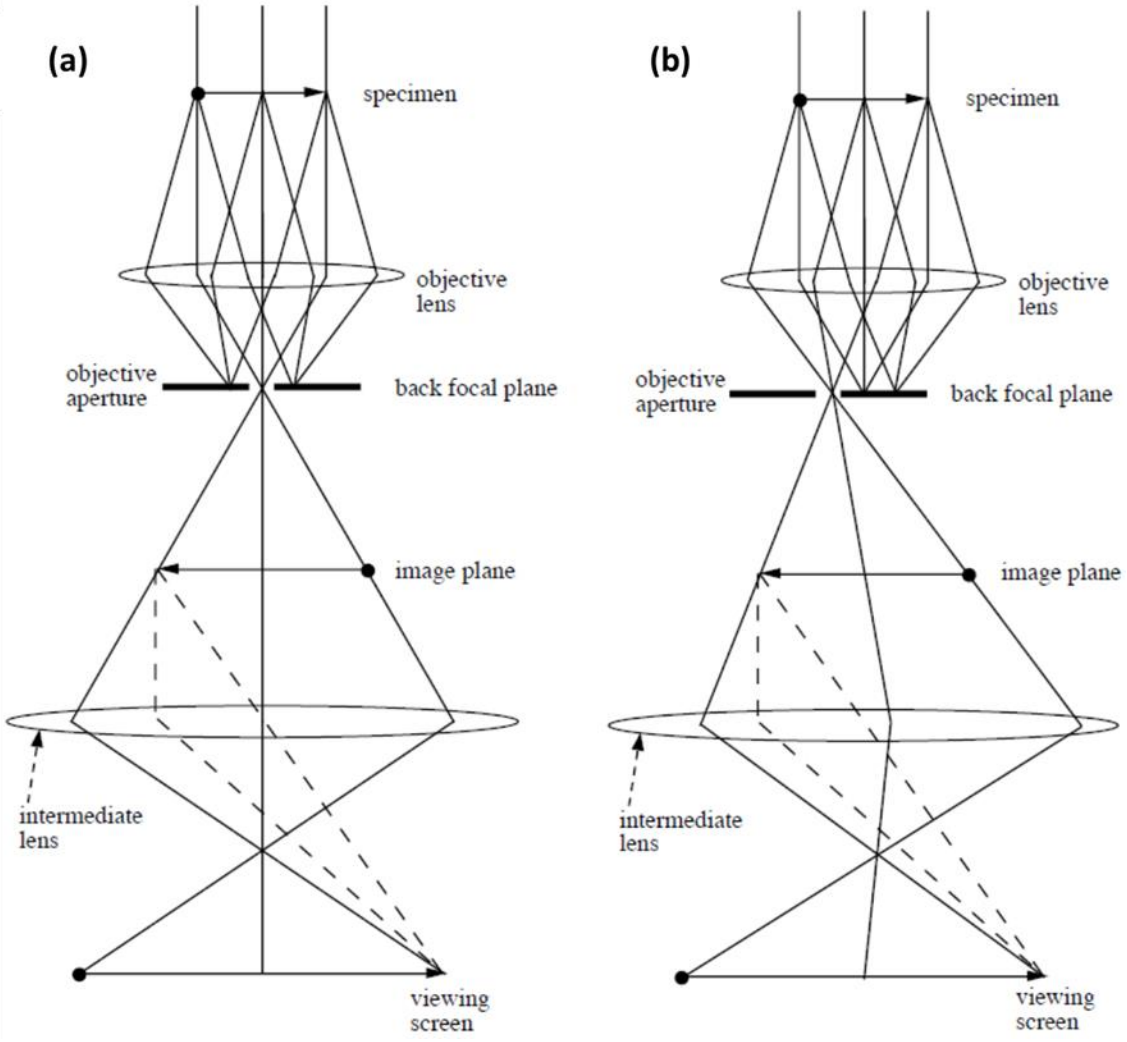

FIG. 2.7 Schematic diagram showing the (a) bright-field and (b) dark-field imaging modes.[163]

Additional imaging techniques in TEM can be used to provide very specific information. High-resolution TEM (HRTEM) allows imaging of the sample at the atomic scale and resolution of its crystallographic structure, making it very useful in the study of material properties on the nanoscale. In this mode, image contrast is highly

dependent on the microscope and specimen parameters, as well as the condition of the microscope and its components. Appropriate accelerating voltages, focal lengths, and aperture sizes must be selected to minimize chromatic aberration, diffraction effects, and astimgmatism. Another invaluable imaging mode is scanning TEM (STEM), where the rastering of the beam across the sample elemental mapping techniques like electron dispersive x-ray spectroscopy (EDS) and electron energy loss spectroscopy are possible. STEM imaging uses a high angle annular dark-field (HAADF) detector that is capable of acquiring atomic resolution images with contrast that is dependent on the atomic (Z) number.

2.2.3 Scanning electron microscopy

Scanning electron microscopy (SEM), like TEM, is an electron microscopy technique and uses electrons at the illumination source.[165] It has, for the most part, similar layout and components as the TEM, but has a different working principle. Rather than being transmitted through the sample, the electron beam interacts with the sample surface, leading to the emission of various types of secondary electrons and photons, providing information about the topography and chemical composition of the sample. The resolution of the SEM is lower than that of the TEM, the best case is on the order of a few nm, with a magnification up to 500 kX. Shown in Figure 2.8 is the schematic showing the layout and components in a SEM, all under high vacuum like the TEM.[166] Unlike the TEM, however, the objective lens and associated apertures are situated before the sample.

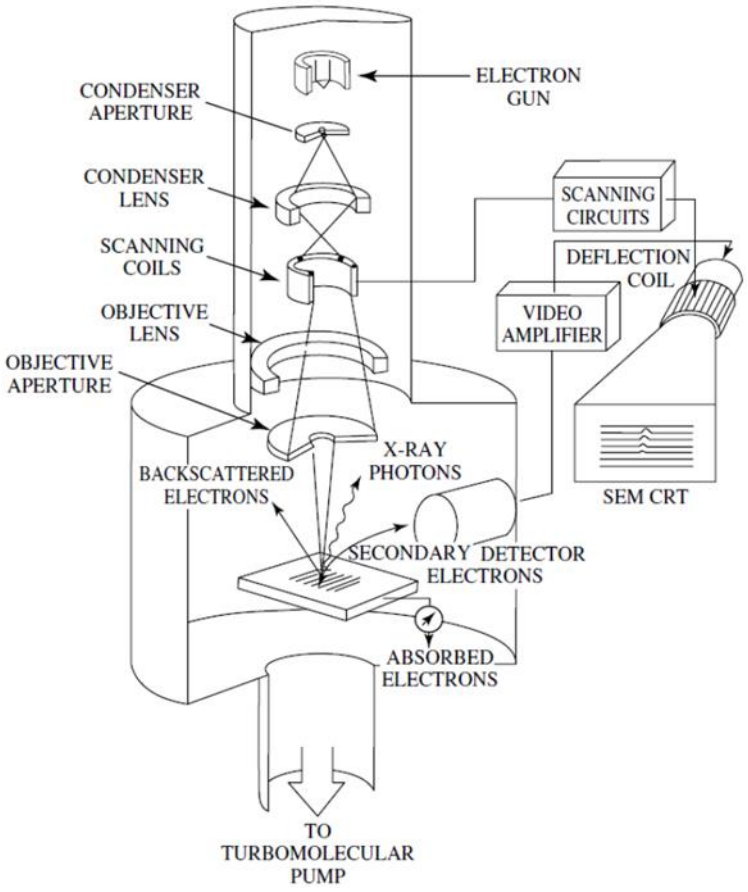

FIG. 2.8 The major components and their layout in a SEM.[166]

The electron beam is focused to a fine probe performs a raster scan across the sample surface. The secondary species are projected onto an imaging detector, directly mapping every point scanned by the electron beam. Several interactions occur due to the electron penetration of the surface, which cause the emission of the different secondary species, as shown in Figure 2.9.

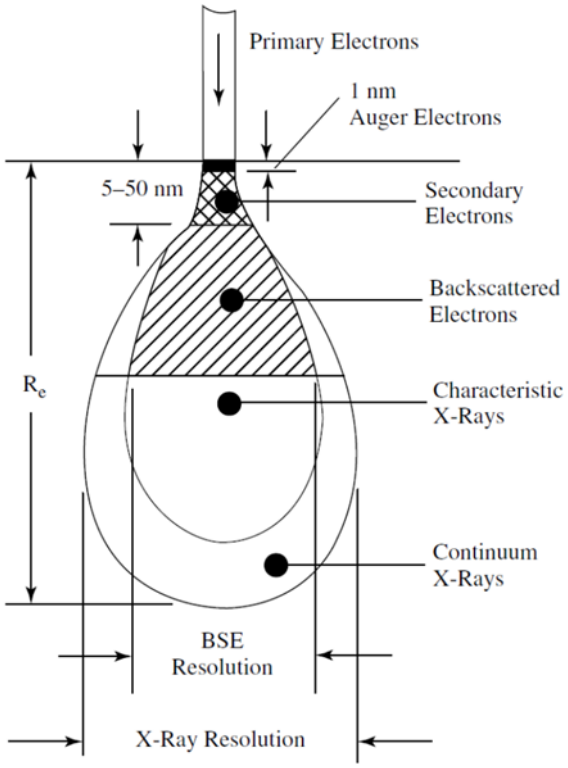

FIG. 2.9 Relative escape depths for different secondary species created due to interaction with an incident electron beam.[166]

The three primary image types produced in the SEM are secondary electron (SE) images, backscattered electron (BSE) images, and elemental x-ray maps. SEs are produced primarily due to inelastic scattering of the primary beam with the atomic electrons in the sample. The energy of emitted SEs is typically less than 50 eV from an escape depth of 5-50 nm. SEs give topographical information about the sample surface. BSEs are higher energy electrons produced by elastic scattering of the primary beam by the nuclei of the atoms in the sample. BSEs have energies greater than 50 eV, typically close to the energy of the primary beam, and BSEs have depths a hundred times greater

than those of SEs. Backscattering is more likely due atom with a higher Z number, so the BSE intensity due to a higher Z number atom will be greater than with a lower Z number atom. BSE images provide contrast based on Z number differences and are especially useful in the analysis of composite materials. The third type of image, or elemental x-ray analysis (also known as electron microprobe), can use either energy dispersive or wavelength dispersive detectors, based on the characteristic x-rays emitted from the sample. Though elemental x-ray analysis is described here in relation to SEM, it is equally be implemented in TEM with the same working principle.

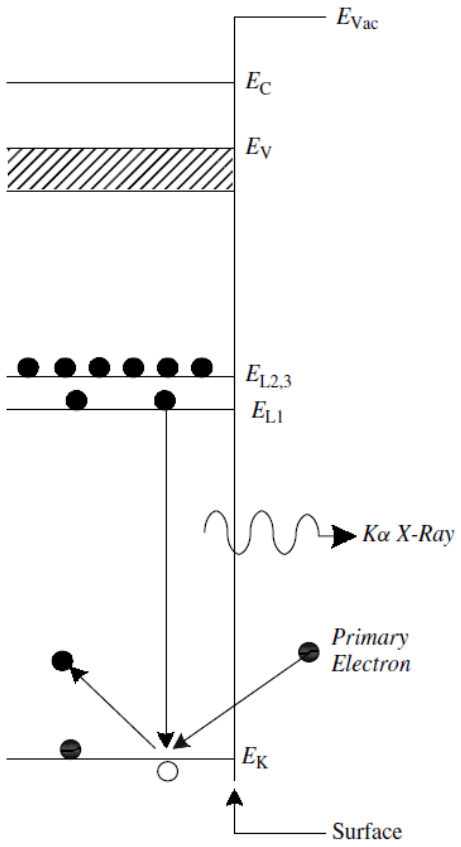

FIG. 2.10 Electronic processes in EDS.[166]

In EDS, the electron beam bombardment on a sample causes a core level electron to get ejected from its shell leaving behind a hole, as shown in Figure 2.10. An electron from an outer shell fills the hole, emitting a characteristic x-ray photon whose energy is equal to the energy difference between the outer shell and lower energy shell. EDS is used to get quantitative information about the chemical composition of the sample. The lateral resolution in EDS is limited by the ability to focus the primary beam (probe size) and the interaction volume of the beam in the sample.

2.2.4 Secondary ion mass spectrometry

One of the most sensitive materials analysis techniques, secondary ion mass spectrometry (SIMS), also known as the ion microprobe, has limits of detection in the range of parts per million (ppm) or lower.[165] It has a depth resolution as low as 2 nm and a lateral resolution of 2 to 5 μm depending on the mode of operation. The operating principle of SIMS is based on sputtering and ionization of atoms from a sample surface using a primary beam of heavy ions. Magnetic lenses deflect the ionized species to a detector where they are collected and analyzed based on particle mass to provide the chemical composition of the sample. For quantification, reference materials of identical composition must be analyzed under similar conditions as a comparison. Unlike the non-destructive materials analysis techniques discussed so far, SIMS is a destructive technique.

Ions like O_2^+, Cs^+, and Ar^+ are used as the primary species. Primary ion energies range between 1-20 keV. When the primary ion beam bombards the sample, energy and

momentum are transferred to the atoms in the sample causing their ejection from the surface in the form of neutral particles and charged particles (atomic ions and ionized clusters). The interaction volume between the primary beam and the sample atoms is referred to as the mixing zone, whose depth is a dependent on the incident angle, mass, and energy of the primary ions and of the sample, and is a resolution limiting factor in this technique. SIMS measures only the charged species, not the neutral ones, so its detection limit depends on the ionization probability of the ejected particles. Shown in Figure 2.11 is a schematic showing the layout of the SIMS system.

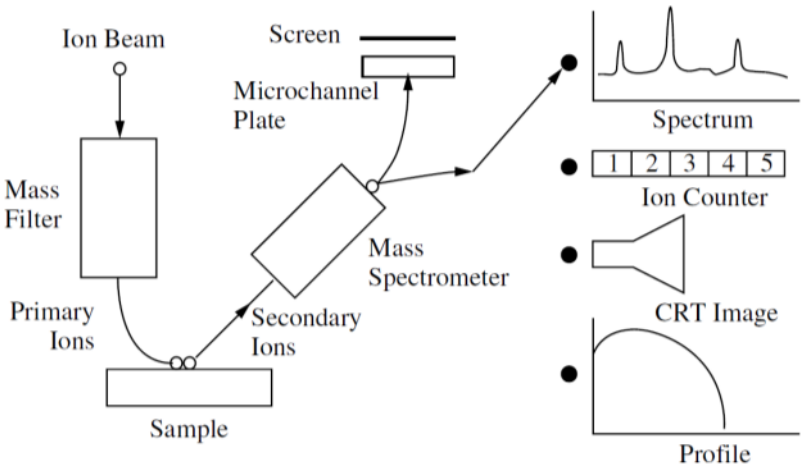

FIG. 2.11 Schematic layout of a SIMS system.[166]

SIMS has four basic operation modes: depth profiling, bulk analysis for lateral resolution, mass scanning to determine the mass spectrum in an entire volume of a sample, and imaging to determine lateral distribution of specific elements (can be used in conjunction with depth profiling). The main types of instrumentation are mass

separation by the electromagnetic field and time-of-flight measurements. Mass separation due to the electromagnetic field is based on physically separating ions depending on their charge to mass ratios by changing the magnetic field strength. In time-of-flight measurements, the primary ion beam is pulsed following which the secondary ions drift to the detector; mass separation in this case is based to the time required by different masses to reach the detector.

2.3 Polarization-electric field measurement

Ferroelectric P-E measurements are typically performed using sophisticated commercially available testers. In addition to the P-E measurement, several other measurements can be performed, like retention, imprint, fatigue, capacitance-voltage, and leakage current measurements on ferroelectrics, as well as resistive and dielectric materials. The basic measurement circuit is a modified version or the original circuit used by Sawyer and Tower for their measurements on Rochelle salt. Shown in Figure 2.12 (a) is the original Sawyer- Tower circuit.

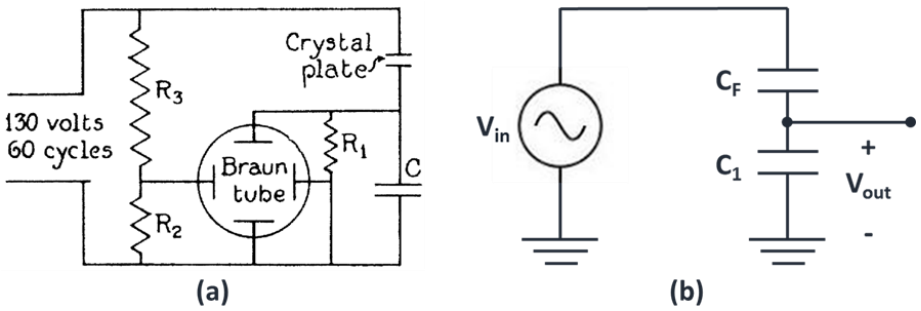

FIG. 2.12 (a) The original and (b) simplified Sawyer-Tower circuit.[167]

From the simplified Sawyer-Tower circuit in Figure 2.12 (b), a voltage source is connected to the ferroelectric capacitor C_F which is connected in series to a sense capacitor C_1 of known capacitance such that $C_1 >> C_F$.

The charge Q across a parallel plate capacitor is given by

$$Q = CV \tag{2-4}$$

where C is the capacitance and V is the applied voltage. The charge can also be written as

$$Q = 2P_r A \tag{2-5}$$

where A is the cross-sectional area.

From Eqns. 2-4 and 2-5, the relationship between the capacitance and polarization is given by

$$C \propto \frac{dP_r}{dV} \tag{2-6}$$

Thus, the polarization is measured by monitoring the change in the voltage across the sense capacitor C_1 in Fig. 2.12 (b). Shown in Figure 2.13 (a) and (b) are the capacitance and polarization hysteresis loops, respectively, for a $Pb(Zr,Ti)O_3$-$Pb(Fe,Ta)O_3$ composite

structure. As described in Eqn. 2-6, it is observed that the maxima of the capacitance curves occur at the coercive voltages $\pm V_C$ of the polarization loop.

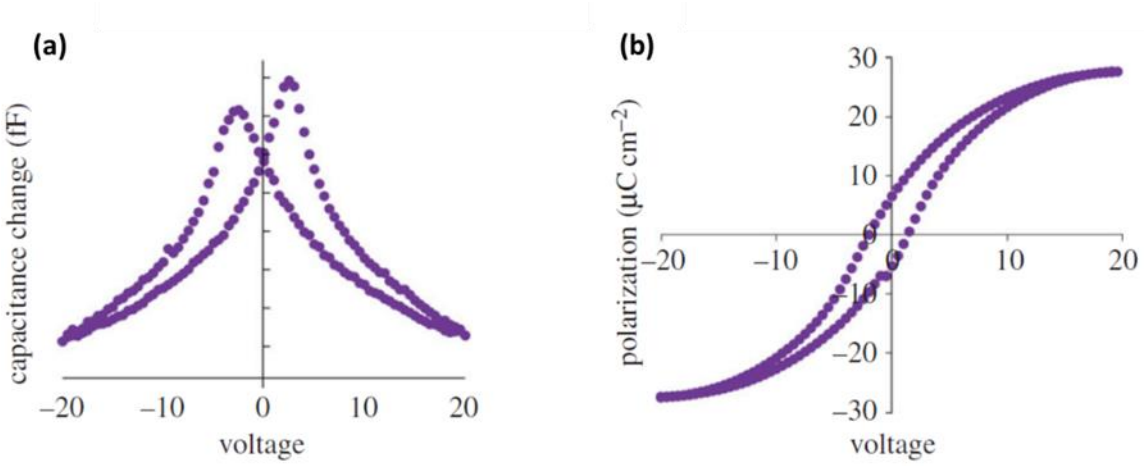

FIG. 2.13 (a) Capacitance and (b) polarization hysteresis loops, respectively, for a $Pb(Zr,Ti)O_3$-$Pb(Fe,Ta)O_3$ composite structure.[168]

CHAPTER III

FERROELECTRIC PROPERTIES OF BARIUM TITANATE – CERIUM OXIDE NANOCOMPOSITES ON STRONTIUM TITNATE SUBSTRATES*

3.1 Overview

Epitaxial $(BaTiO_3)_{0.5}(CeO_2)_{0.5}$ films have been deposited in vertically aligned nanocomposite form on $SrTiO_3$ substrates. X-ray diffraction and transmission electron microscopy characterization show that the films consist of distinct *c*-axis oriented $BaTiO_3$ and CeO_2 phases. Polarization measurements show that the $BaTiO_3$-CeO_2 films are actually ferroelectric at room temperature, and the ferroelectric response is comparable to that of pure $BaTiO_3$ on $SrTiO_3$ single crystalline substrates. Capacitance-voltage measurements show that, instead of decreasing, the Curie temperature increases to 175 ^oC. This work is an essential step towards integrating novel nanostructured materials with advanced functionalities into Si-based devices.

---

*This chapter is adapted with permission from "Ferroelectric Properties of Vertically Aligned Nanostructured $BaTiO_3$-CeO_2 Thin Films and Their Integration on Silicon" by F. Khatkhatay, A. P. Chen, J. H. Lee, W. R. Zhang, H. Abdel-Raziq, and H. Y. Wang, ACS Applied Materials & Interfaces, **5**, 12541 (2013). Copyright © 2013 by the American Chemical Society.

3.2 Introduction

Efforts on developing lead-free materials for ferroelectric applications have gained momentum, owing largely to the great technological needs for such materials and the toxic nature of lead, along with an increasing environmental consciousness.[50,51,169] $BaTiO_3$ (BTO), a representative ferroelectric perovskite oxide, has long been the frontrunner among alternatives to lead-based materials in the development of thin-film ferroelectric devices. Bulk BTO exhibits a tetragonal structure at room temperature, with an in-plane lattice parameter a = 3.992 Å and out-of-plane lattice parameter c = 4.036 Å, and a remnant polarization (P_r) of about 25-27 μC/cm^2.[25] A major impediment to the implementation of BTO in ferroelectric devices has been its low Curie temperature (T_C) of 120 ^{o}C to 130 ^{o}C, where the BTO crystal structure changes from tetragonal to cubic.[23,25] As the temperature is increased, the spontaneous polarization (P_s) decreases, disappearing completely once T_C is exceeded.[25] The optimum ferroelectric response for BTO occurs when the out-of-plane film growth is c axis oriented.[53,54] In-plane compressive strain has been shown to increase the T_C as well as improve the P_r in BTO.[55]

Recently, a new method of introducing strain by incorporating a secondary phase into thin film architectures has evolved, namely self-assembled vertically aligned nanocomposites (VANs).[116] A VAN system, a class of two phase thin-film materials, typically consists of two immiscible phases that show periodic vertical growth of alternating nanoscale heteroepitaxial domains. The unique architecture of these

structures allows for precise tuning of their mechanical, electronic, and magnetic properties through vertical strain control, as well as interfacial coupling of those properties for advanced functionalities in a variety of applications like multiferroics[108,110], spintronics[111,112], superconductors[113], solid oxide fuel cells[114], and electrically tunable dielectrics[115].

The area of electrically tunable dielectrics is a potential application for ferroelectric perovskites like BTO, owing to the variability of their dielectric constants with applied DC bias.[30] The main drawback is that ferroelectrics suffer from high dielectric losses, which can be reduced by doping or by addition of a second phase low dielectric constant material. For this purpose CeO_2, a rare-earth fluorite oxide, has long been considered as a prospective dopant in BTO.[170] BTO and CeO_2 have liquid immiscibility in the 20 to 85 % CeO_2 range[171,172], and can both grow epitaxially on $SrTiO_3$ (STO) substrates, with cube-on-cube growth[53] and 45° in-plane rotation[173], respectively, based on their lattice parameters (a_{BTO} = 3.992 Å; a_{CeO_2} = 5.411 Å; a_{STO} = 3.905 Å). However, previous studies have shown that even small additions of CeO_2 reduce the BTO tetragonal to cubic phase transition temperature and thereby the T_C to below room temperature.[171,172,174,175] It is possible, by carefully controlling the processing conditions, that BTO and CeO_2 could still be retained as two separate phases in the same composite material, and grow epitaxially in VAN form on STO. In this work, ferroelectric BTO-CeO_2 VAN films have been deposited on single crystal STO substrates.

3.3 Experimental

All films were deposited in a vacuum chamber with a base pressure of approximately 10^{-7} Torr at a temperature of 700 ^{o}C by pulsed laser deposition (PLD) using a Lambda Physik Compex Pro 205 KrF excimer laser (λ = 248 nm). $SrRuO_3$ (SRO) bottom electrodes and BTO-CeO_2 films were deposited at a pulse rate of 5 Hz at an optimized oxygen partial pressure of 40 mTorr. Immediately following the deposition, the films were annealed at a temperature of 500 ^{o}C for 30 mins at an oxygen partial pressure of 500 Torr. 100 nm thick Au top contacts of 0.1 mm^2 area, were deposited on the BTO-CeO_2 film surface.

X-ray diffraction (XRD) spectra were measured using a PANalytical Empyrean 2 diffractometer. Leakage current and capacitance-voltage (C-V) measurements were conducted using an Agilent E4980A Precision LCR meter. Ferroelectric polarization-electric field hysteresis (P-E) measurements were conducted on a TF Analyzer 1000 with leakage current compensation from aixACCT Systems GmbH. Transmission electron microscopy (TEM) and scanning tunneling electron microscopy (STEM) images were taken using a FEI Tecnai G2 F20 ST FE-TEM and electron diffraction images were acquired using a JEOL JEM-2010 TEM.

3.4 Results and discussion

3.4.1 BTO-CeO_2 film growth

Fig. 3.1 shows the XRD θ-2θ pattern of BTO-CeO_2 grown at a pulse rate of 5 Hz on single crystalline STO substrates with an SRO bottom electrode. Clear peaks were observed for BTO (*00l*) and CeO_2 (*00l*), suggesting a preferential out-of-plane orientation of (*00l*) for both phases. No additional peaks associated with the BTO-CeO_2 system were observed, indicating that there is no intermixing between the two phases. The *c* value is determined to be 4.10 Å for the BTO phase. The peak position error is found to be ±144 arcsec, corresponding to a *d*-spacing error of ±0.002 Å. ϕ-scans, to investigate the in-plane orientation, were conducted on the BTO-CeO_2 films on STO, shown in the inset in Fig. 3.1. A comparison of the ϕ-scans of the STO (110) and BTO (110) planes shows four small peaks for the BTO phase which exactly coincide with four sharp peaks for the STO substrate, indicating the cube-on-cube growth for the BTO phase as expected. From the comparison of the ϕ-scans of the STO (111) and CeO_2 (111) planes, it is evident that the four smaller peaks from the CeO_2 phase are offset from the four sharp STO peaks by exactly 45°, indicating that the CeO_2 phase has an in-plane rotation of 45° relative to the STO substrate. The in-plane orientation again shows that the BTO and CeO_2 have grown as two distinct phases and that there is no obvious intermixing between the two phases.

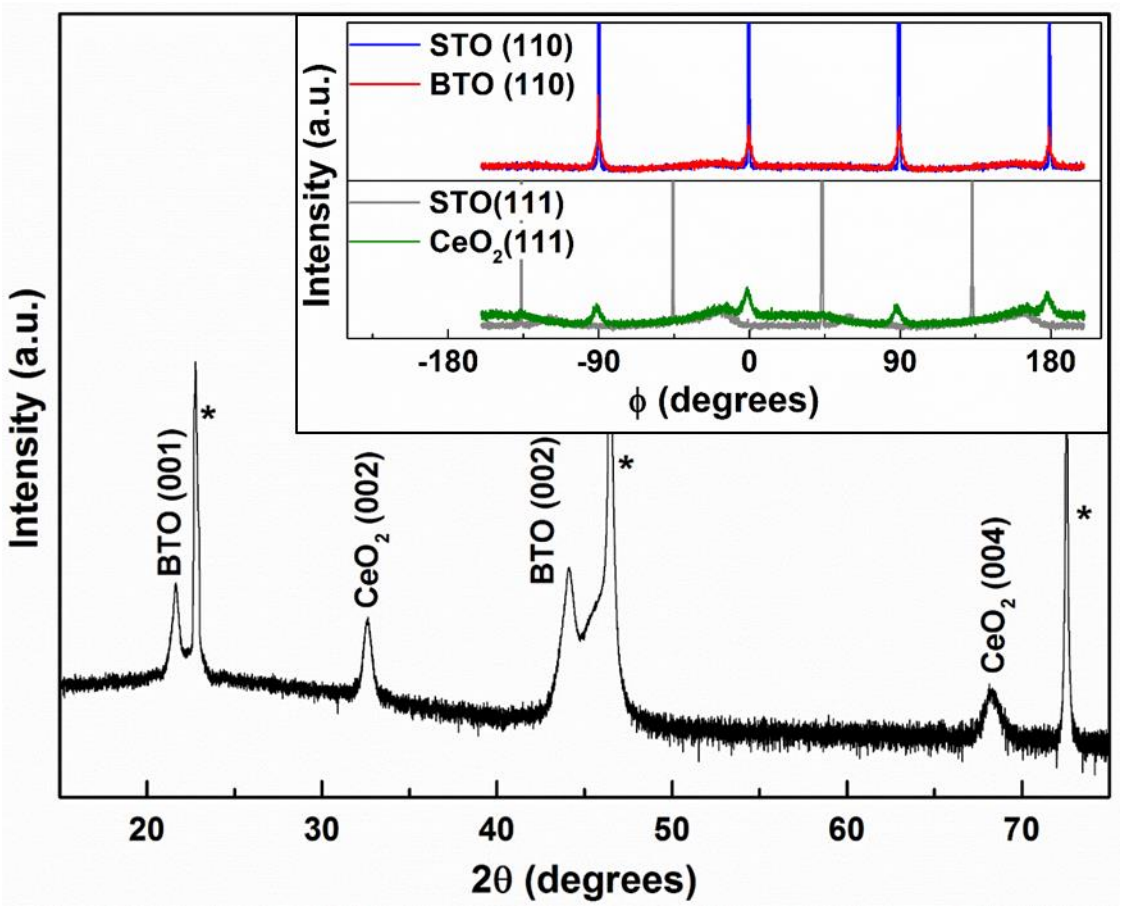

FIG. 3.1 XRD θ-2θ scan of the for BTO-CeO_2 films grown on STO, the substrate peaks are denoted as "*". The inset shows the ϕ-scan of the BTO (110) plane relative to the STO (110) plane and the CeO_2 (111) plane relative to the STO (111) plane.

3.4.2 Microstructure characterization

TEM cross-section images of the BTO-CeO_2 films grown on STO are shown in Fig. 3.2. The low magnification image of the cross-section is shown in Fig. 3.2 (a), with

the inset showing the corresponding selected area electron diffraction (SAED) pattern. The BTO-CeO_2 layer is approximately 65 nm thick and has obvious columnar structure of the two phases. The SAED pattern shows the in-plane matching relationship to be $(010)_{BTO} \| (011)_{CeO2} \| (010)_{STO}$, confirming the observations in the XRD ϕ-scans in Fig. 3.1, where BTO matches STO as cube-on-cube and CeO_2 matches with STO with a 45^o in plane rotation. The *c* and *a* values for the BTO phase are determined to be 4.06 Å and 3.98 Å, respectively, suggesting in a *c/a* ratio of 1.02, an out-of-plane tensile strain of 0.59 % and an in-plane compressive strain of 0.3 %, compared to the bulk values of 4.036 Å and 3.992 Å for *c* and *a* (*c/a* ratio of 1.011). The calculation of the lattice parameters based on the TEM diffraction pattern was conducted to verify the calculations from the XRD measurements. The lattice parameters based on the XRD data should still be taken as the accurate values. The high resolution image in Fig. 3.2 (b) shows that the film has grown epitaxially on the thick SRO layer with distinct vertically aligned BTO and CeO_2 phases, both with column widths of 3-5 nm. The high resolution image of the film in Fig. 3.2 (c) of the BTO-CeO_2/SRO/STO interfaces shows that the interfaces are sharp and abrupt. The 7 nm thick SRO film grows highly epitaxially on the STO substrate, so does the nanostructured BTO-CeO_2 film.

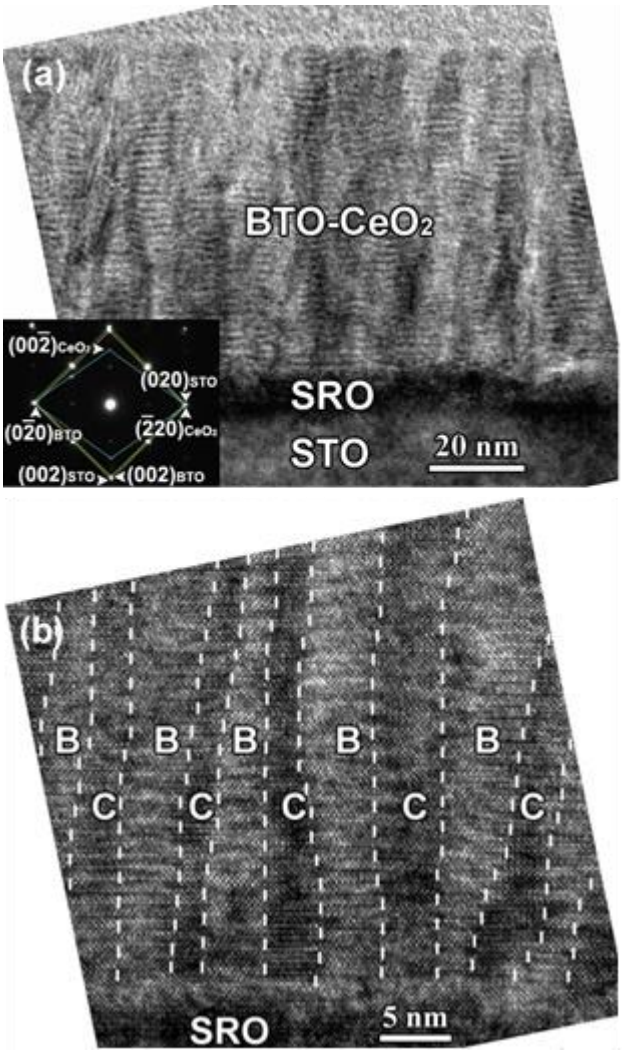

FIG. 3.2 TEM micrographs for the BTO-CeO_2 films deposited on STO. (a) Low resolution image showing the film stack with the inset showing the corresponding SAD pattern; (b) high resolution image showing vertically aligned nanocolumns of BTO (B) and CeO_2 (C); (c) high resolution image of the interface between the BTO-CeO_2 film, SRO bottom electrode, and STO substrate.

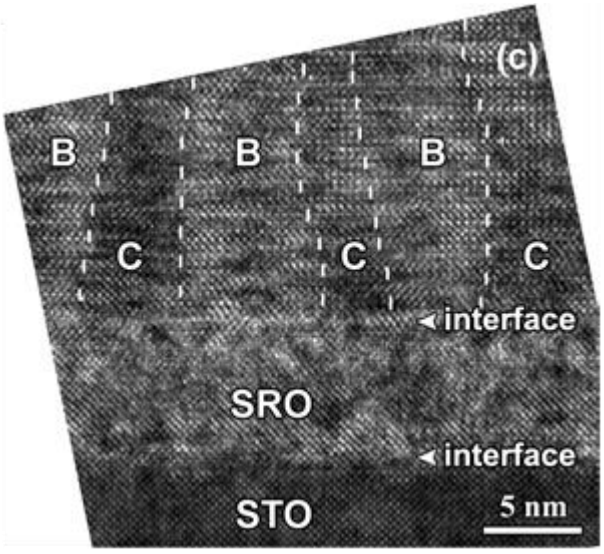

FIG. 3.2 Continued.

3.4.3 Electrical measurements

Figure 3.3 presents the electrical properties measured for the BTO-CeO_2 films grown on STO. Figure 3.3 (a) shows the leakage current, while Figure 3.3 (b) shows the P-E curve measured on the at 1 kHz up to a voltage of 10 V at room temperature. There is a distinct ferroelectric response at room temperature, indicating that the T_C is above room temperature. In the ferroelectric P-E curve, *Ps* is the saturation polarization value,

Pr is the remnant polarization when the applied field reduced to zero, *Vc* and *Ec* are the coercive voltage and coercive field, respectively, required to force the polarization value to zero. The P_r is determined to be 21 μC/cm^2, with a coercive voltage (V_c) of 3.5 V, coercive field (E_c) of 538 kV/cm, and P_s of 37 μC/cm^2. These values are consistent with the P_r of 14 μC/cm^2 and P_s of 27 μC/cm^2 measured for pure BTO films grown on STO.[65] The C-V hysteresis curves in Figure 3.3 (c), measured at 10 kHz, shows a butterfly curve. However, the maxima of the C-V curve at ±0.2 V do not correspond to the V_c values observed in Figure 3.3 (b). This disparity could be attributed to artifacts due to the instrument configuration or the high leakage current, or both. Figure 3.3 (d) shows the change in the measured dielectric permittivity ($\varepsilon/\varepsilon_0$) as a function of measurement temperature. The peak in the $\varepsilon/\varepsilon_0$ curve at 175 ^{o}C suggests that the T_C has increased beyond the values of 120-130 ^{o}C for bulk BTO. This suggests that the incorporation of CeO_2 with BTO in VAN form presents a promising approach for increasing T_C of BTO.

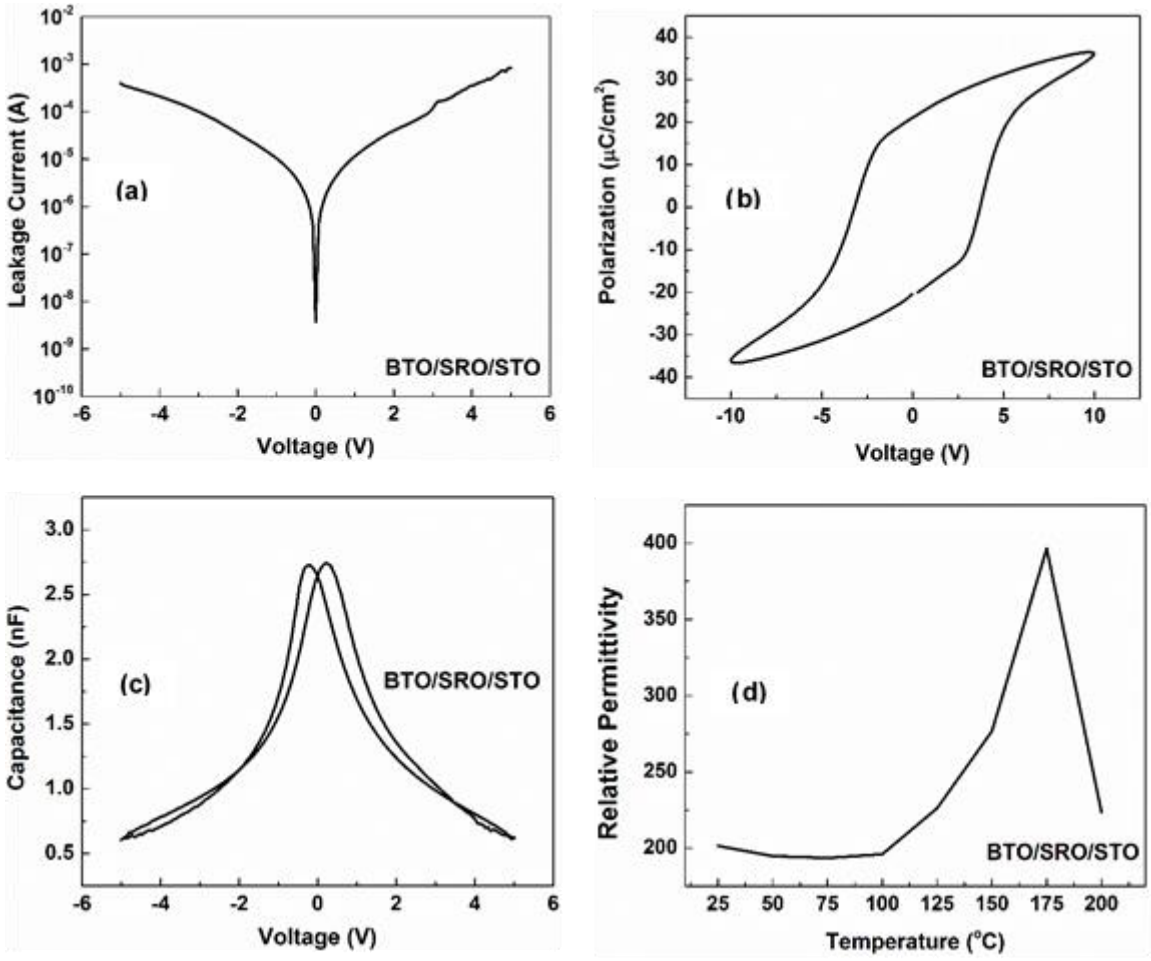

FIG. 3.3 Electrical measurements on BTO-CeO_2 films deposited on STO substrates: (a) leakage current, (b) polarization hysteresis at 1 kHz, (c) room temperature capacitance-voltage curve at 10 kHz, and (d) the variation of the dielectric constant with temperature at 10 kHz.

3.4.4 Discussion

The data presented so far show that the ferroelectric properties of the BTO-CeO_2 films deposited on STO substrates are comparable to reports of pure BTO deposited on STO substrates.[65,176,177] The remarkable property of BTO-CeO_2 composite thin films is the exhibition of ferroelectric properties at and beyond room temperature, despite the high concentration of CeO_2. However, in previous reports, CeO_2 has been shown to decrease the tetragonal to cubic phase transition temperature and hence the T_C in BTO.[171,172,174,175] Even in a vertically oriented BTO and CeO_2 composite, the T_C was reported to steadily decrease with increasing concentrations of CeO_2, down to as low as -80 ^oC.[178] Increasing the CeO_2 concentration in BTO was found to cause an expansion of the *a* axis, a shrinking of the *c* axis, resulting in a net decrease in the *c*/*a* ratio, which was believed to be caused due to Ce substitution of Ba in the BTO lattice.[170,179,180] It was determined that in reducing environments above 1250 ^oC, CeO_2 undergoes a chemical change to Ce_2O_3, where the stable tetravalent Ce^{4+} state changes to Ce^{3+}, which is responsible for the substitution of the Ba.[180] Most of these previous reports involved processing temperatures far beyond 1250 ^oC. A high temperature processing step in target preparation could result in a reaction involving the Ba and Ce and thus any films deposited using that target would be affected accordingly.

Conversely, in our case, the sintering temperature for the composite target was maintained at 1200 ^oC, preventing Ce/Ba substitution reaction from occurring. The *c*/*a* ratio for the BTO-CeO_2 film is 1.02, which shows that tetragonality is maintained in the

BTO lattice at room temperature. Previously, VAN structures of BTO-Sm_2O_3[119] and $Ba_{0.6}Sr_{0.4}TiO_3$-Sm_2O_3[115] on STO substrates both show an increased T_C, where the onset of the tetragonal to cubic phase transition was delayed in the strained BTO matrix by the considerably harder Sm_2O_3 phase. CeO_2 has a reported elastic modulus in the range of 112 to 264 GPa,[181] so it serves a similar function as the Sm_2O_3 (elastic modulus of 125 GPa[119]) described above. Thus, the retention of ferroelectric properties at room temperature is due to the processing conditions of the composite target, while the extension of the T_C beyond the bulk value can be attributed to the strained configuration owing to the VAN structure.

3.5 Conclusions

We have successfully demonstrated, for the first time, a room temperature ferroelectric response in BTO-CeO_2 1:1 molar ratio composites, and an increase in the T_C to 175 ^oC owing to a strained VAN structure. The BTO-CeO_2 films grow in a VAN architecture of 3-5 nm column widths on STO substrates. The BTO-CeO_2 composite shows no Ce substitution of the Ba in the BTO lattice, no obvious intermixing, and no intermediate phase formation. These results show that by precise tailoring of processing and deposition conditions, it is possible to improve the ferroelectric response and the T_C of the BTO-CeO_2 system.

CHAPTER IV

INTEGRATION OF BARIUM TITANATE – CERIUM OXIDE NANOCOMPOSITES ON SILICON*

4.1 Overview

Epitaxial $(BaTiO_3)_{0.5}(CeO_2)_{0.5}$ films have been deposited in vertically aligned nanocomposite form on $SrTiO_3$/TiN buffered Si substrates to achieve high quality ferroelectrics on Si. The thin TiN seed layer promotes the epitaxial growth of the $SrTiO_3$ buffer on Si, which in turn is essential for the high quality growth of the vertically aligned nanocomposite structure. X-ray diffraction and transmission electron microscopy characterization show that the films consist of distinct *c*-axis oriented $BaTiO_3$ and CeO_2 phases. Polarization measurements show that, the $BaTiO_3$-CeO_2 films on Si are actually ferroelectric at room temperature, and the ferroelectric response is comparable to pure $BaTiO_3$ as well as the $BaTiO_3$-CeO_2 films on $SrTiO_3$ single crystalline substrates. Capacitance-voltage measurements show that, the Curie temperature increases to 150 ^oC. This work is an essential step towards integrating novel nanostructured materials with advanced functionalities into Si-based devices.

---

*This chapter is adapted with permission from "Ferroelectric Properties of Vertically Aligned Nanostructured $BaTiO_3$-CeO_2 Thin Films and Their Integration on Silicon" by F. Khatkhatay, A. P. Chen, J. H. Lee, W. R. Zhang, H. Abdel-Raziq, and H. Y. Wang, ACS Applied Materials & Interfaces, **5**, 12541 (2013). Copyright © 2013 by the American Chemical Society.

4.2 Introduction

In the previous chapter, we have demonstrated that the ferroelectric properties of $BaTiO_3$ (BTO) can be improved by incorporating it with CeO_2 into a vertically aligned nanocomposite (VAN) structure. Most epitaxial VAN systems thus far, including our BTO-CeO_2 system, have been demonstrated on expensive single-crystal oxide substrates such as STO, MgO, and $LaAlO_3$, with very few exceptions.[116] Instead, it is more economically desirable to integrate the proposed BTO-CeO_2 VANs on Si substrates, which simultaneously opens up the possibility of future incorporation of VAN systems in conventional Si-based devices. Previously, epitaxial BTO thin films on Si have been demonstrated using molecular beam epitaxy and atomic layer deposition.[54,149,150] To improve the quality of BTO grown on Si, an epitaxially grown STO buffer layer can be implemented[152-154], while a thin TiN buffer layer can be used to promote the growth of single-crystal-like epitaxial STO. In this work, ferroelectric BTO-CeO_2 VAN films have been deposited on Si substrates. Various buffer layer combinations, including no buffer, STO only, TiN only, and STO/TiN, have been explored to determine the best epitaxial quality of the VAN films and their ferroelectric properties. Finally, the VAN film deposition frequency was varied to determine the optimal ferroelectric properties for the VAN structures on Si.

4.3 Experimental

All films were deposited in a vacuum chamber with a base pressure of approximately 10^{-7} Torr at a temperature of 700 ^{o}C by pulsed laser deposition (PLD) using a Lambda Physik Compex Pro 205 KrF excimer laser (λ = 248 nm). The TiN and STO targets used for PLD were hot-pressed stoichiometric TiN and STO, respectively, purchased from Plasmaterials, Inc. The BTO-CeO_2 (1:1 molar ratio, sintered at 1200 ^{o}C) and $SrRuO_3$ (SRO) targets were custom made from powders purchased from Alfa Aesar. The substrates used for deposition were Si (001). The substrates were subjected to a 5 min buffered oxide etch to strip the native oxide prior to loading in the vacuum chamber. The TiN seed layer was deposited under vacuum at a pulse rate of 10 Hz. The STO buffer and SRO bottom electrode were deposited at a pulse rate of 5 Hz, while the deposition frequency for the BTO-CeO_2 films was varied as 2 Hz, 5 Hz, and 10 Hz, all at an optimized oxygen partial pressure of 40 mTorr. Immediately following the deposition, the films were annealed at a temperature of 500 ^{o}C for 30 mins at an oxygen partial pressure of 500 Torr. 100 nm thick Au top contacts of 0.1 mm^2 area, were deposited on the BTO-CeO_2 film surface in a custom-built magnetron sputtering system using a 99.99% pure Au sputter target from Williams Advanced Materials.

X-ray diffraction (XRD) spectra were measured using a PANalytical Empyrean 2 diffractometer. Leakage current and capacitance-voltage (C-V) measurements were conducted using an Agilent E4980A Precision LCR meter. Ferroelectric polarization-electric field hysteresis (P-E) measurements were conducted on a TF Analyzer 1000

with leakage current compensation from aixACCT Systems GmbH. Transmission electron microscopy (TEM) and scanning tunneling electron microscopy (STEM) images were taken using a FEI Tecnai G2 F20 ST FE-TEM and electron diffraction images were acquired using a JEOL JEM-2010 TEM.

4.4 Results and discussion

4.4.1 Effect of buffer layers

4.4.1.1 BTO-CeO_2 VAN growth on Si

A set of BTO-CeO_2 VAN thin films were deposited on Si substrates with various combinations of buffer layers. Figure 4.1 shows the XRD spectra of the BTO-CeO_2 samples deposited at 5 Hz on Si (a) with STO/TiN buffer, (b) with TiN only, (c) with STO only, and (d) without any buffer. In Figure 4.1 (a), the films on the STO/TiN buffered Si shows clear peaks for BTO (*00l*), CeO_2 (002), and STO (*00l*) peaks which, similar to the films grown directly on the STO substrate, indicates a preferential out-of-plane orientation of (*00l*) for both phases as well as the STO buffer layer. This suggests that the VAN films grown on STO/TiN buffered Si have comparable crystallinity and film quality as those on the STO substrates. No peaks associated with TiN buffer are observed, except for a small TiO_2 (004) peak, indicating that the thin TiN seed layer (10 nm) has been partially oxidized during the subsequent oxide layer growth.

Among the other samples, in Figure 4.1 (b-d), only the sample with TiN buffer shows two small peaks from BTO (*00l*), while the sample with the STO buffer and the one without any buffer both don't show any obvious film peaks. The buffer layer study clearly suggests that the TiN seed layer serves as a critical epitaxial template for the STO buffer growth, which in turn is crucial for the highly epitaxial growth of the BTO-CeO_2 nanostructured film on Si. Despite the large lattice mismatch between TiN and Si (over 24%), TiN has been reported to grow on Si epitaxially through domain matching epitaxy[182].

Figure 4.2 shows the ϕ-scans for the BTO-CeO_2 films on STO/TiN buffered Si substrates, including STO (110) and BTO (110) planes relative to the Si (110) plane and CeO_2 (111) relative to Si (111). This is consistent with ϕ-scans of the samples directly grown on STO substrates, i.e., cube-on-cube growth for BTO and STO relative to the Si, and a 45^o in-plane rotation between CeO_2 and Si.

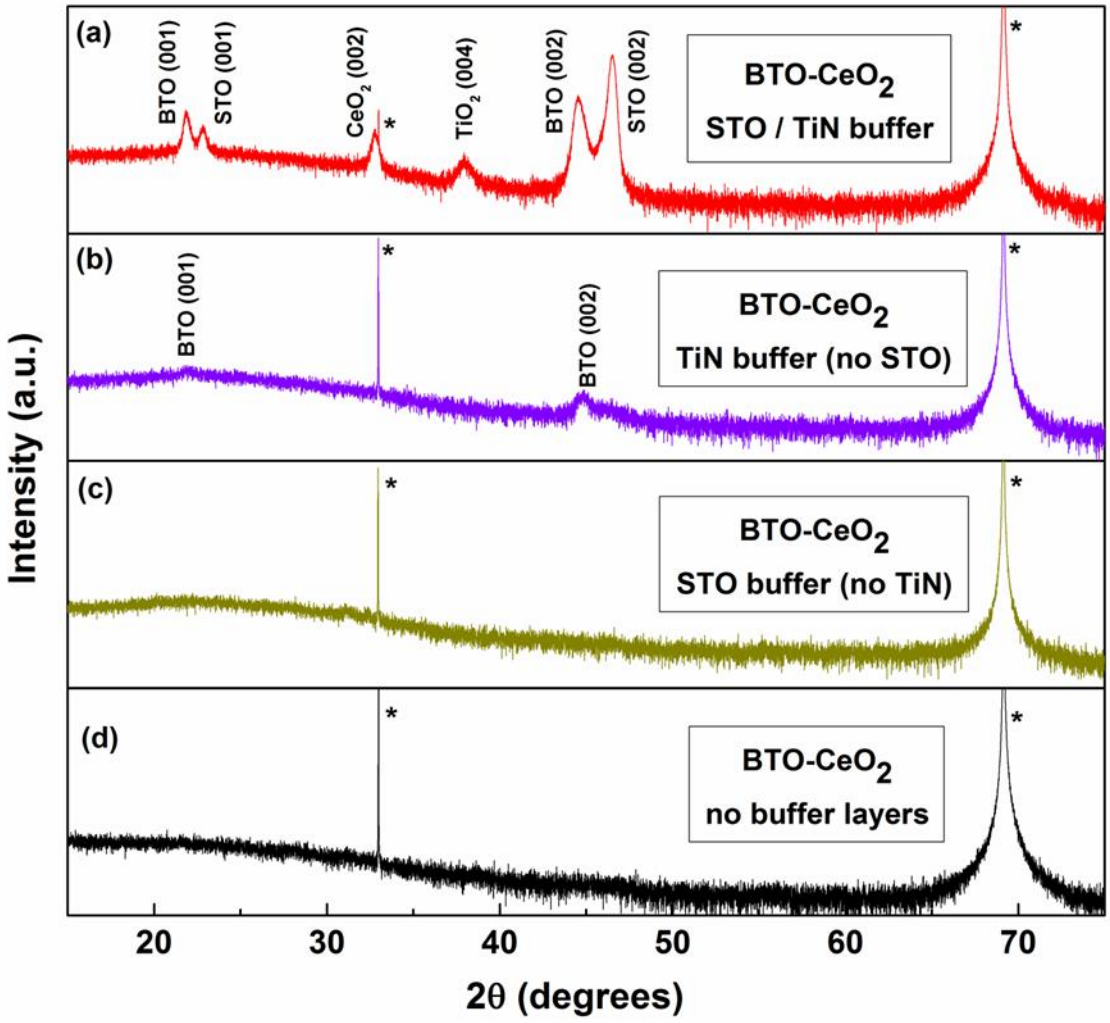

FIG. 4.1 Comparison of the XRD θ-2θ scans for BTO-CeO_2 films deposited at 5 Hz as a function of buffer layers.

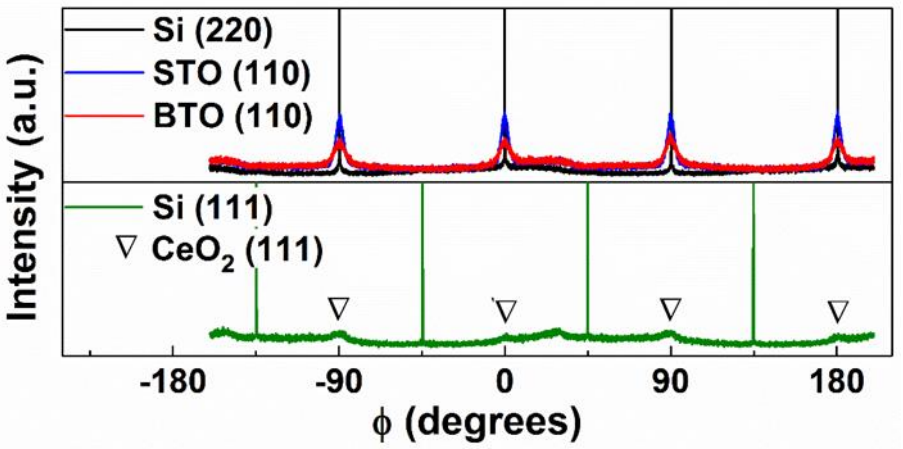

FIG. 4.2 ϕ-scan of the BTO (110) and STO (110) planes relative to the Si (110) plane and the ϕ-scan of the Si (111) plane showing four small CeO_2 (111) peaks (denoted as "∇") offset 45° from the Si (111) peaks.

4.4.1.2 Microstructure characterization

Shown in Figure 4.3 are the TEM cross-section images of the BTO-CeO_2 films grown on STO/TiN buffered Si substrates. The low magnification cross-section TEM image is shown in Figure 4.3 (a), with the inset for the corresponding SAED pattern. The BTO-CeO_2 layer is approximately 65 nm thick and the STO buffer layer is approximately 40 nm thick. The distinct diffraction dots from all the film layers in the SAED pattern confirm the high quality epitaxial growth of the buffer layers and the VAN films. The in-plane matching relationship is determined to be $(011)_{BTO} \| (010)_{CeO2} \| (011)_{STO} \| (011)_{Si}$ confirming the observations made in the XRD ϕ-scans in

Figure 4.2. The *c* and *a* values for the BTO phase are determined to be 4.04 Å and 3.98 Å, respectively, suggesting in a *c*/*a* ratio of 1.01, an out-of-plane tensile strain of 0.1% and an in-plane compressive strain of 0.3 %. Figure 4.3 (b) shows the STEM image of the sample in high angle annular dark-field mode (HAADF, also called Z-contrast image, where the image contrast is proportional to $Z^{1.7}$). The BTO-CeO_2 film shows clear columnar growth of the BTO (darker contrast) and CeO_2 (brighter contrast) phases. The high resolution TEM image in Figure 4.3 (c) shows the growth of the epitaxial TiN and STO buffer layers on Si substrate where the interfaces are sharp and there is no intermixing of the layers, except a thin (1-2 nm) native SiO_x layer at the TiN/Si interface formed during substrate heating prior to deposition. Figure 4.3 (d), the 7 nm thick SRO film has grown highly epitaxially on the STO buffer, which provides an epitaxial template for the BTO-CeO_2 film growth. The high quality epitaxial growth of BTO and CeO_2 phases is evident with clear phase boundaries and the average column widths are both 3-5 nm. It is noted that compared to the BTO-CeO_2 films grown on STO substrates the columnar structure in the films grown on the STO/TiN buffered Si substrates are less defined. This corresponds to the higher quality film growth observed on the STO substrates compared that on STO/TiN buffered Si.

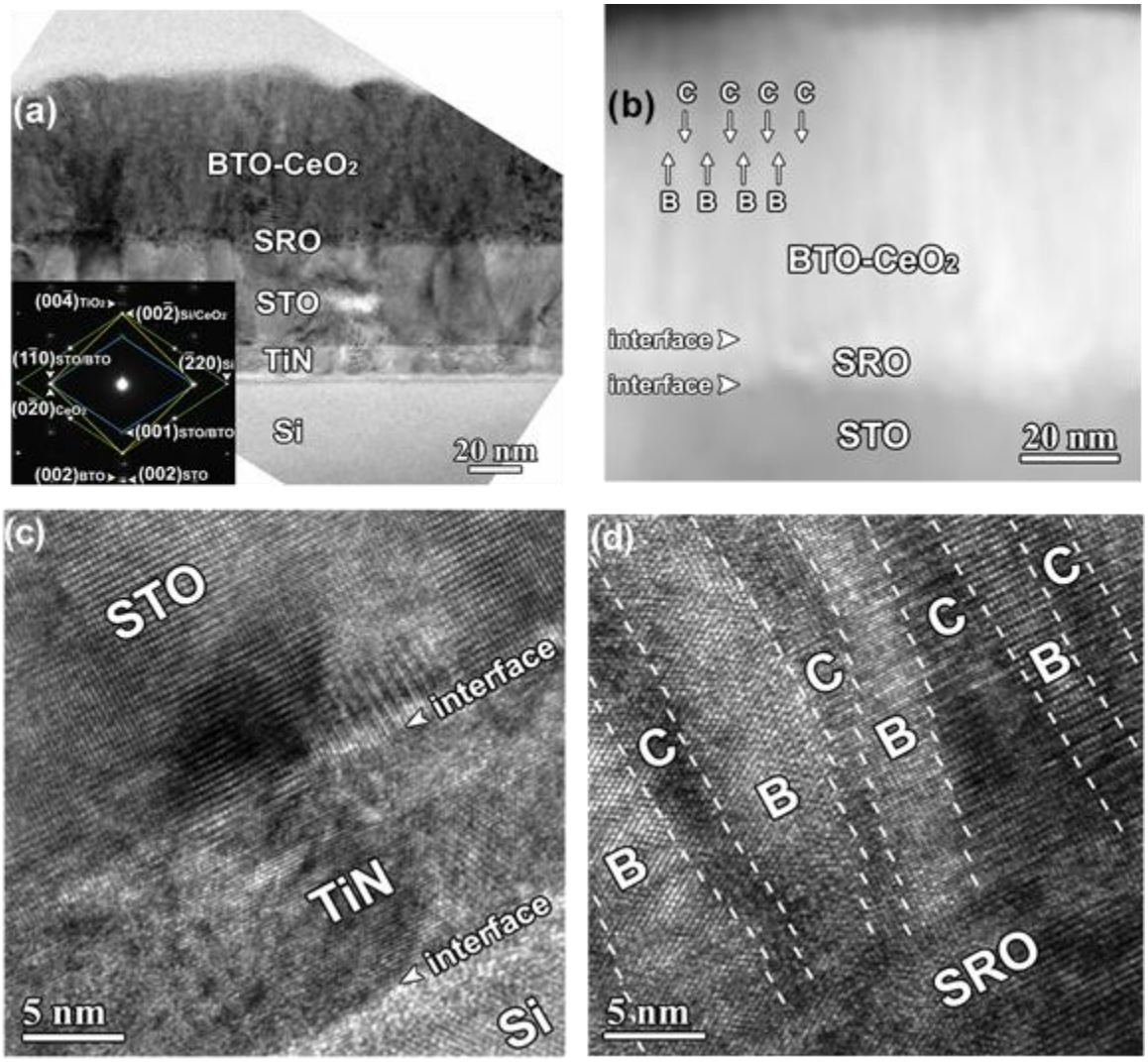

FIG. 4.3 TEM micrographs for BTO-CeO_2 films grown on the SRO/STO/TiN/Si stack at 5 Hz. (a) Low resolution image of the film stack with the inset showing the corresponding SAED pattern; (b) STEM dark field image showing the vertically aligned nanocolumns of BTO (B, darker contrast) and CeO_2 (C, lighter contrast); (c) high resolution image showing the STO and TiN layers grown on the Si substrate; (d) high resolution image showing the vertically aligned nanocolumns of BTO (B) and CeO_2 (C) on the SRO bottom electrode.

4.4.1.3 Effect of buffer layers on electrical results

In the ferroelectric P-E curve, *Ps* is the saturation polarization value, *Pr* is the remnant polarization when the applied field reduced to zero, *Vc* and *Ec* are the coercive voltage and coercive field, respectively, required to force the polarization value to zero. The P-E measurements for the VAN films deposited on Si with various buffer layers are presented in Fig. 7. As expected, the best response is observed in the STO/TiN buffered Si substrate, with a *Pr* of 13 $\mu C/cm^2$, *Vc* of 2 V, *Ec* of 307 kV/cm, and *Ps* of 29 $\mu C/cm^2$, respectively. In comparison, the sample without the buffer layers shows no ferroelectric response, and the hysteresis loop is characteristic of a lossy dielectric. Oddly however, the sample deposited without the TiN seed layer also shows a ferroelectric response, though not as good as that of the sample grown on the STO/TiN/Si stack. It is possible that there may be some localized ordering in the STO layer that has prompted some local texturing of the BTO phase, not obvious through the XRD characterization. It is also interesting to note that despite the lack of obvious texturing in the samples with only STO buffer, the ferroelectric response implies that there is no intermediate phase formation between the BTO and CeO_2 regardless of the presence of buffer layers.

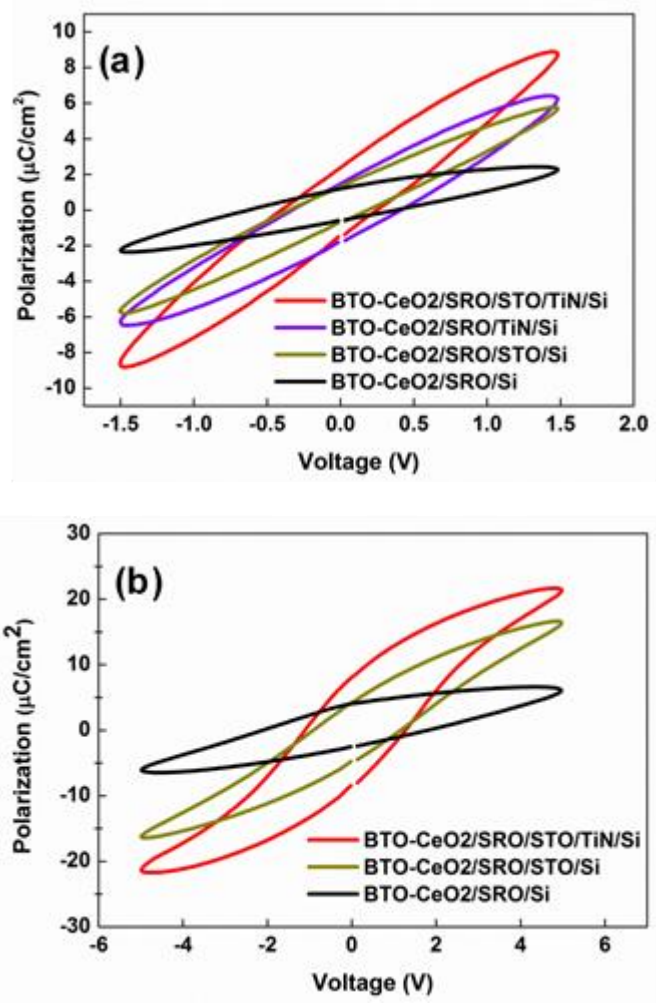

FIG. 4.4 Comparison of the polarization hysteresis measurements for BTO-CeO_2 films deposited at 5 Hz as a function of various buffer layers measured at (a) 1.5 V, (b) 4 V, and (c) 9 V.

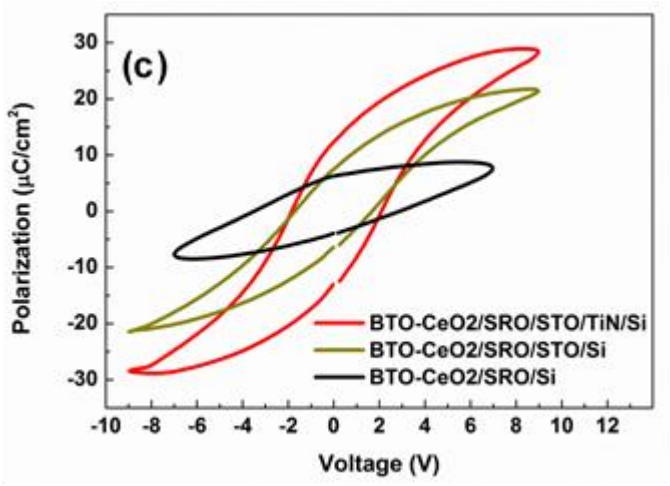

FIG. 4.4 Continued.

In Figure 4.5, the electrical properties measured for the BTO-CeO_2 films grown on Si. The C-V hysteresis curves in Figure 4.5 (a), measured at 10 kHz, show butterfly curves, however, the maxima of the C-V curve at -0.2 V and 0.1 V in the case of the STO/TiN buffered Si substrate, do not correspond to the V_c values observed in Figure 4.4 (c). This disparity could be attributed to artifacts due to the instrument configuration or a high leakage current, or both. Figure 4.5 (b) shows the change in the measured dielectric permittivity ($\varepsilon/\varepsilon_0$) as a function of measurement temperature. The peak in the $\varepsilon/\varepsilon_0$ curve 150 ^oC for the Si substrate suggests that the T_C has increased beyond the values of 120-130 ^oC for bulk BTO. This suggests that the incorporation of CeO_2 with BTO in VAN form presents a promising approach for increasing T_C of BTO.

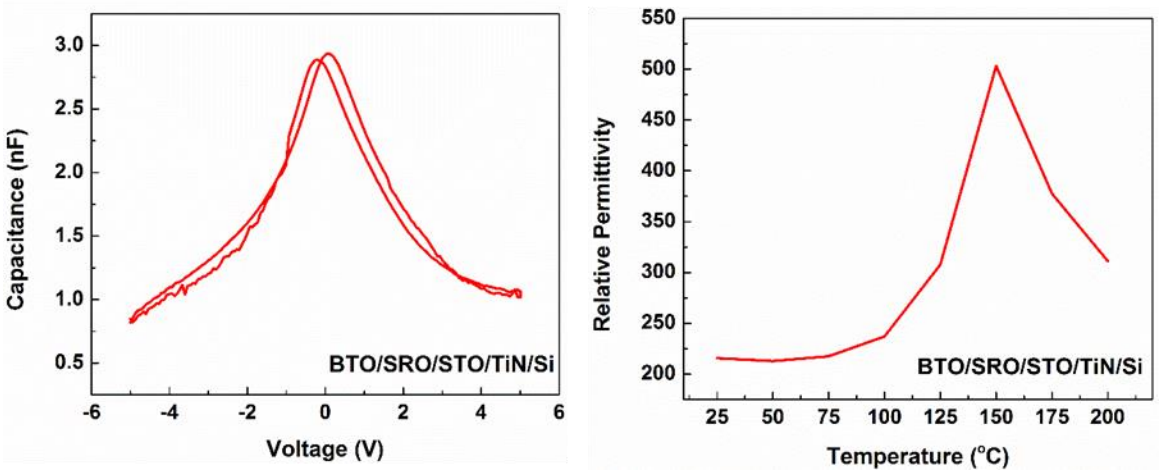

FIG. 4.5 Electrical measurements on BTO-CeO_2 films deposited on STO/TiN buffered Si substrates: (a) the room temperature capacitance-voltage curve at a measurement frequency of 10 kHz and (b) the variation of the dielectric constant with temperature at a measurement frequency of 10 kHz.

4.4.2 Frequency optimization

In addition to the effect of the buffer layers, the deposition frequency also has a strong impact on the epitaxial growth of the BTO-CeO_2 films as well as their ferroelectric properties.

4.4.2.1 Film quality

Shown in Figure 4.6 is the XRD data for BTO-CeO_2 films, all approximately 65 nm thick, grown on the STO/TiN/Si stack as a function of deposition frequency. Figures 4.6 (a), (b), and (c) show the data for the samples deposited at 5 Hz, 2 Hz, and 10 Hz,

respectively. All three samples show distinct BTO, STO, and CeO_2 (*00l*) peaks. Upon closer examination of the BTO (001) peak position in Figure 4.6 (d), there appears to be a correlation between the deposition frequency and the BTO (001) peak position. The peak for the 10 Hz sample has the smallest 2θ position, followed by the 5 Hz sample, and then the 2 Hz sample, corresponding to *c* value of 4.07 Å, 4.06 Å, and 4.06 Å, respectively. The corresponding out-of-plane tensile strain is calculated to be 0.57%, 0.68%, and 0.81%, respectively. The full width at half maximum (FWHM) for the BTO (001) peak is measured to be 0.293º, 0.329º, and 0.361º for the 5 Hz, 2 Hz, and 10 Hz samples, respectively.

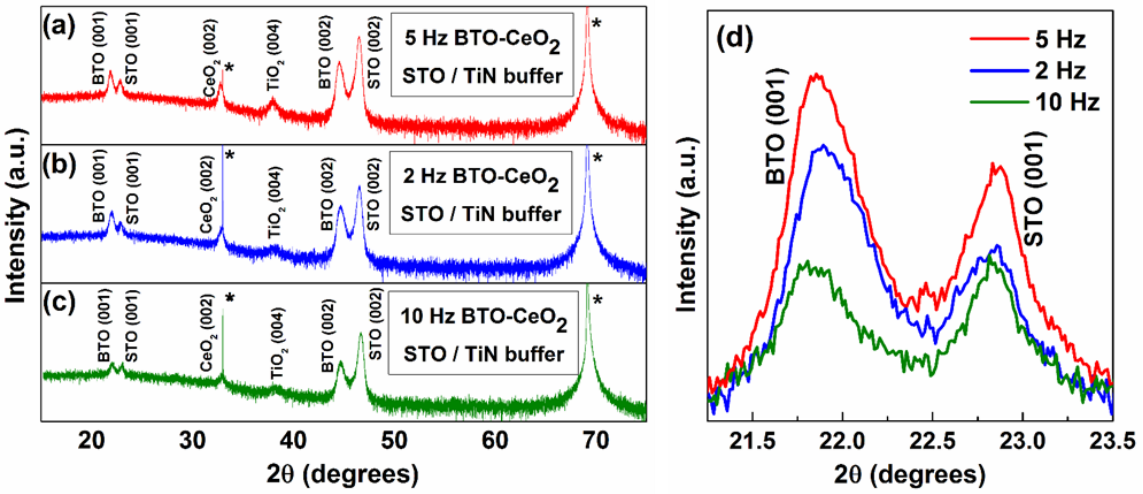

FIG. 4.6 Comparison of the XRD θ-2θ scans for BTO peak for the BTO-CeO_2 films deposited on the SRO/STO/TiN/Si stack at (a) 5 Hz, (b) 2 Hz, and (c) 10 Hz; (d) position of the BTO (001) peak as a function of deposition frequency.

4.4.2.2 Frequency dependence of electrical results

It is expected that, based on the *c* value and out-of-plane strain, the 10 Hz sample should have the best ferroelectric response. However, from the P-E measurement data in Figure 4.7, the 5 Hz sample still shows the best ferroelectric response, closely followed by the 2 Hz sample, while the response of the 10 Hz sample is much poorer, which directly correlates to their FWHM values. This shows that 5 Hz is the optimum deposition frequency to achieve the best epitaxial quality of the BTO-CeO_2 films on the SRO/STO/TiN/Si stack, resulting in the optimum ferroelectric response.

4.4.3 Discussion

The ferroelectric response of the BTO-CeO_2 films deposited on Si is slightly lower than, but still in the same range as that of the BTO-CeO_2 films on STO, discussed in Chapter III. The FWHM of 0.263^o for the films grown on the STO substrate is close

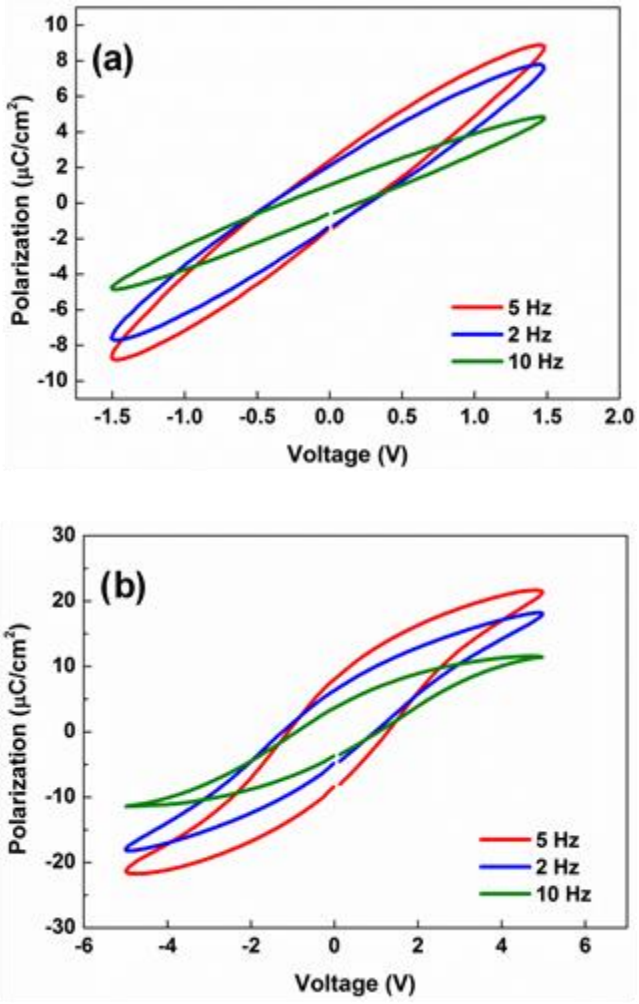

FIG. 4.7 Comparison of the polarization hysteresis measurements for BTO-CeO_2 films deposited on the SRO/STO/TiN/Si stack as a function of deposition frequency measured at (a) 1.5 V, (b) 4 V, and (c) 9 V.

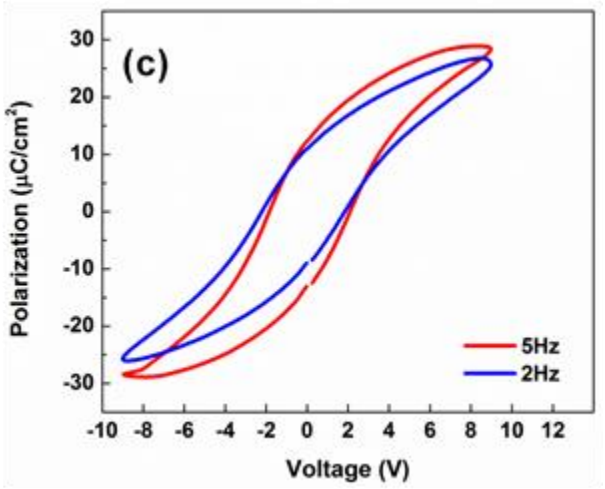

FIG. 4.7 Continued.

to, but still better than that of any of the films grown on Si, indicating that the quality of the films on the STO substrate are slightly better than those grown on Si. This can be attributed to the quality of the STO buffer layer compared to the STO substrates; improving the epitaxial quality of this layer will most likely improve the ferroelectric response of the films deposited on Si substrates. It must be noted, moreover, that the properties of BTO-CeO_2 films deposited on Si are also comparable to those of BTO and other BTO-based materials deposited on Si.[183-186]

4.5 Conclusions

We have successfully demonstrated, for the first time, a room temperature ferroelectric response in BTO-CeO_2 1:1 molar ratio composites, and an increase in the T_C to at least 150 ^oC owing to the strained VAN structure integrated on Si. The BTO-

CeO_2 films grow in a VAN architecture of 3-5 nm column widths on TiN/STO buffered Si substrates. The BTO-CeO_2 composite shows no Ce substitution of the Ba in the BTO lattice, no obvious intermixing, and no intermediate phase formation. The TiN seed layer protects the underlying Si substrate from oxidation, while providing a template for the near epitaxial growth of the STO buffer layer as well as a highly epitaxial VAN structure. These results show that by careful selection of buffer layers, the integration of high quality functional VAN architectures on Si substrates is highly feasible, opening the door to future incorporation of functional oxide materials in conventional Si-based devices.

CHAPTER V

RESISTIVE SWITCHING IN OXIDIZED TITANIUM NITRIDE

5.1 Overview

Forming-free resistive switching devices have been fabricated by *in situ* thermal oxidation of epitaxial TiN films on Si substrates, with the oxidized region serving as the oxide layer and the nitride region serving as the bottom electrode. X-ray diffraction and transmission electron microscopy characterizations confirm the formation of an oxide layer and its thickness is directly dependent on the oxidation time. Secondary ion mass spectrometry profiles show that the oxide formed is near stoichiometric TiO_2, and there is a non-stoichiometric oxygen-deficient layer at the TiO_2/TiN interface. From current-voltage hysteresis measurements, all films show forming-free bipolar resistive switching, regardless of the oxide layer thickness. The elimination of the electroforming step is attributed to the oxygen deficient layer at the oxide/nitride interface. This work demonstrates a one-step fabrication process for a simple resistive switching device.

5.2 Introduction

There has been a renewed interest in resistive switching, a phenomenon long observed in oxide materials and the basis for resistive random access memory devices (RRAM),[71] since the physical realization in 2008 of the missing fourth passive circuit element,[67] the "memristor", theorized in the 1970s[187]. In addition to some nitride[188], carbide[189], and chalcogenide[73] materials, to date, resistive switching has been observed in most oxides, with TiO_2, by far, as the most popular and well-studied.[69] Resistive switching in transition metal oxides like TiO_2 is believed to be driven by the movement of point defects under an applied electric field; oxygen ions and their corresponding oxygen vacancies are the dominant mobile defects at room temperature.[190] This redox reaction causes a localized change in electronic conductivity due to the change in oxygen stoichiometry.[72] Typically, a preliminary irreversible step, called the "electroforming" or "forming" voltage, is required to initiate the switching process by electrically depleting a region of oxygen ions, thereby increasing the local oxygen vacancy concentration.[72,79,80] However, electroforming is a highly unpredictable process and can damage the device, leading to severe variation in device-to-device variability and threatening device integrity.[79,80] Therefore it is highly desirable to eliminate this step. It has been shown that, by introducing an oxygen deficient TiO_{2-x} layer, in addition to the insulating TiO_2, the need for the electroforming step can be eliminated.[80]

TiN, a transition metal nitride, is implemented in a variety of industrial applications due to its very high electrical and thermal conductivity, high hardness, and

significant corrosion and erosion resistance.[131,133,135,136,191] It is very widely used in the semiconductor chip fabrication industry as a diffusion barrier material.[192] However, TiN has poor oxidation resistance.[191] In the oxidation process, oxygen reacts with the TiN to form TiO_2, while the nitrogen gas is expelled from the film into the atmosphere.[193] The oxidation rate is limited by the diffusion of oxygen through the TiO_2,[191] with a reported activation energy of 155-232 kJ/mol in an oxygen environment[193-195]. In some cases, an interlayer is formed at the interface of the oxide and nitride regions that is believed to be an oxynitride, a mixture of oxide and nitride phases,[193,196] or an oxygen deficient TiO_{2-x} layer.[197] In other instances, it is believed that no interlayer is formed and that there is a sharp interface between the oxide and the nitride regions.[195,198] Using the poor oxidation resistance behavior of TiN to our advantage, in this work we demonstrate a one step *in situ* oxidation process of epitaxial TiN films in a pulsed laser deposition chamber for a simple resistive switching device. The oxidized TiN serves as the oxide region, while the remaining TiN, with a conductivity on the order of 15 μΩ-cm,[199] serves as the bottom electrode. The effect of this interlayer, if present, on the resistive switching behavior of such oxide/nitride memristor device is investigated.

5.3 Experimental

All films were deposited in a vacuum chamber with a base pressure of approximately 10^{-7} Torr at a temperature of 700 ^{o}C by PLD using a Lambda Physik Compex Pro 205 KrF excimer laser (λ = 248 nm). The targets used for PLD were hot-pressed stoichiometric TiN, purchased from Plasmaterials, Inc. The substrates used for

deposition were Si (001), purchased from Desert Silicon, Inc. The Si substrates were subject to a 5 min buffered oxide etch to strip the native oxide. The TiN films were deposited under vacuum at a pulse rate of 10 Hz. Immediately following the deposition, the films were annealed at a temperature of 700 ^{o}C and an oxygen partial pressure of 500 Torr; the annealing times were controlled as 1, 2, and 5 min. Finally, 100 nm thick circular Au top contacts, of 0.1 mm^2 area, were sputtered on the oxidized film surface using a 99.99% pure Au sputter target from Williams Advanced Materials. X-ray diffraction (XRD) spectra were measured on a PANalytical Empyrean 2 diffractometer. Current-voltage (I-V) measurements were conducted using an Agilent E4980A Precision LCR meter. Transmission electron microscopy (TEM) was conducted using a FEI Tecnai G2 F20 ST FE-TEM. Secondary ion mass spectrometry (SIMS) for film composition and depth profiling was performed using a custom-modified CAMECA IMS 4f ion microprobe.

5.4 Results and discussion

5.4.1 TiN film growth and TiO_2 formation

Figure 5.1 shows the XRD θ-2θ patterns for the oxidized TiN films as a function of oxidation time, i.e., 1 min, 2 min, and 5 min. In addition to the Si substrate peaks, a distinct strong peak is observed for TiN (002) in all three films, indicating that the TiN films have grown highly textured along Si (001). A comparison of the TiN (002) peak for the three samples shows a systematic reduction in peak intensity with increasing

oxidation time. This suggests that the TiN layer has become progressively thinner with increasing oxidation time, there is an oxidized region above the TiN film that has become thicker with increasing oxidation time, or both. Additional small peaks have been observed corresponding to anatase TiO_2 (denoted as "A") in the sample oxidized for 1 min and rutile TiO_2 (denoted as "R") in the 2 min and 5 min samples, suggesting that the oxide formed is of polycrystalline quality.

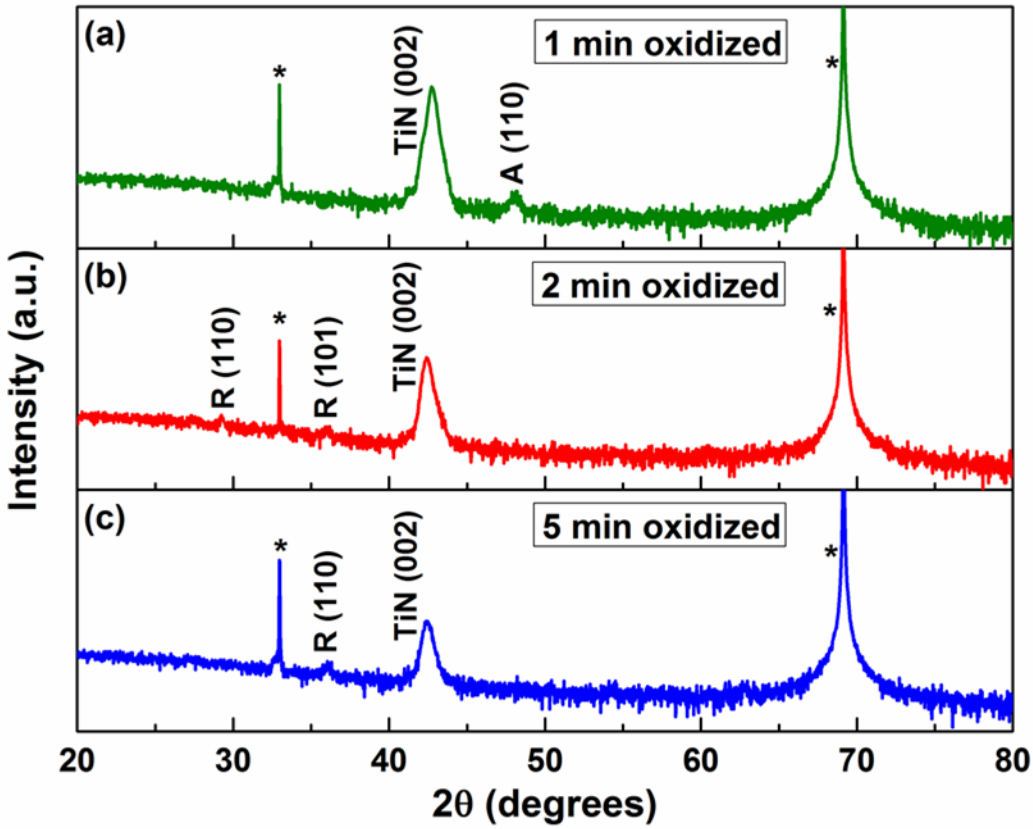

FIG. 5.1 XRD patterns for the samples oxidized for (a) 1 min, (b) 2 min, and (c) 5 min. The Si substrate peaks are denoted as "*", while peaks corresponding to rutile TiO_2 and anatase TiO_2 are denoted as "R" and "A", respectively.

5.4.2 Microstructure characterization

Figures 5.2 (a)-(c) show the cross-section TEM images for all three samples. The low magnification images confirm that in all three films, the top section of the TiN layer has been oxidized, resulting in thicker oxide and thinner nitride layers with increasing oxidation time. The thickness of the oxide layer is 85 nm, 120 nm, and 210 nm for the samples oxidized for 1 min, 2 min, and 5 min, respectively, while the remaining TiN layer thickness is 152 nm, 95 nm, and 62 nm, respectively. Figure 5.2 (d) is the high resolution image of the interface between the oxide and nitride layers for the sample oxidized for 5 min. The TiN region, at the bottom of the image, shows an obvious epitaxial lattice structure. The TiO_x region, at the top of the image, shows polycrystalline nature. An obvious transition region is observed between the oxide and nitride regions, of about 15 to 20 nm thick, is of near amorphous quality. The samples oxidized for 1 and 2 minutes showed a similar transition region of similar thickness between the oxide and nitride regions.

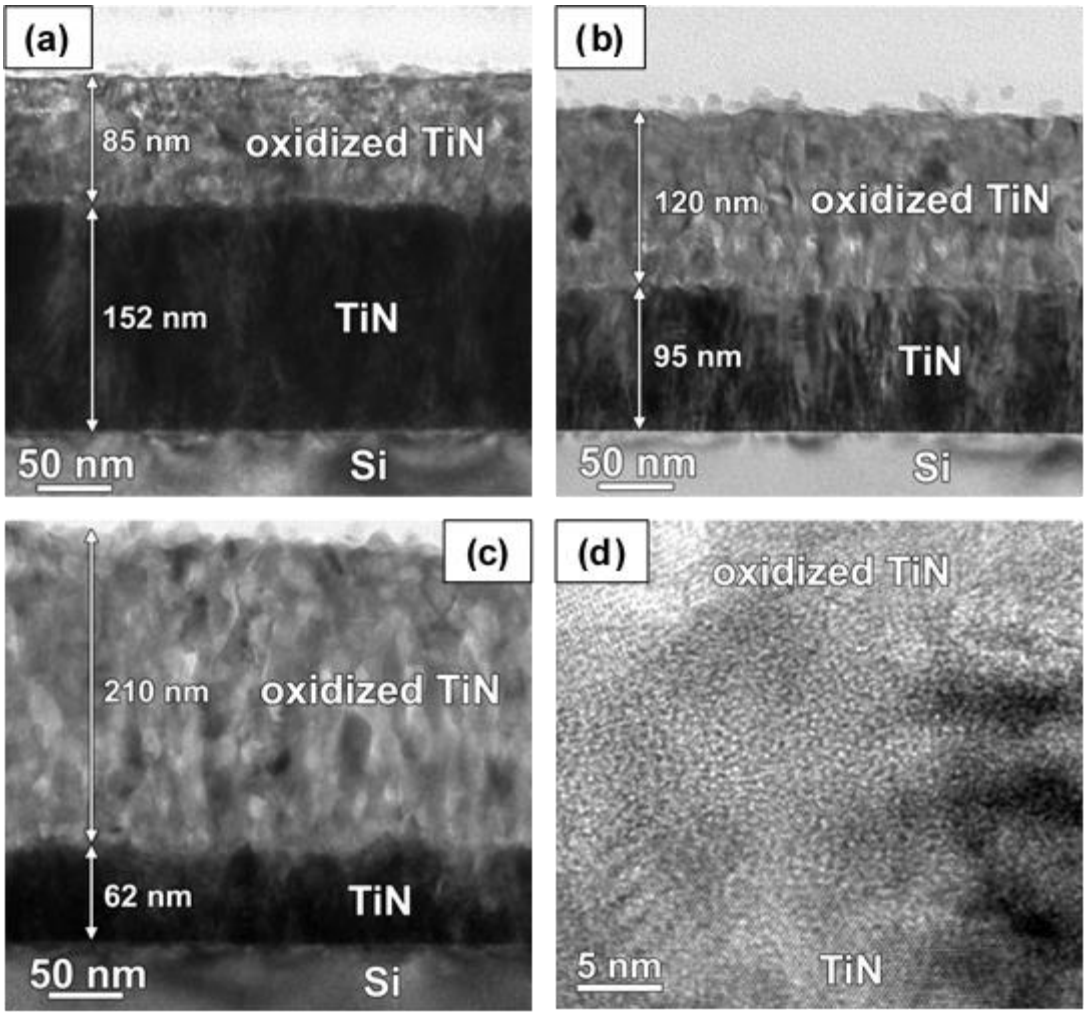

FIG. 5.2 Cross-section TEM images of the samples oxidized for (a) 1 min, (b) 2 min, and (c) 5 min. (d) High resolution image of the interface between the oxide and nitride regions for the sample oxidized for 5 min.

5.4.3 Film composition and depth profiling

To investigate the composition of the oxide layer and of the transition region between the oxide and nitride regions, a detailed SIMS depth profile study was conducted using both positive and negative secondary ions (SI). Figures 5.3 (a)-(c) show the SIMS profiles for the samples oxidized for 1 min, 2 min, and 5 min. The ion mass is given in the superscript preceding the element name, while the "+" or "-" in the superscript following it denotes the charge of the emitted ion. The SI intensities in the profiles reflect the qualitative film composition and the ionization probabilities of the emitted ions. To determine the film stoichiometry in the oxidized TiN region, the relative intensities between the $^{16}O^{+}$ and the $^{50}Ti^{+}$ profiles were compared to those of a reference stoichiometric TiO_2 film. As shown in Table 1 below, it was found that in all three samples, the oxidized TiN regions are near stoichiometric TiO_2 with a possibility of slight oxygen deficiency if considering instrument errors.

Table 5.1 Film composition/stoichiometry calculated from relative $^{16}O^+$ and $^{50}Ti^+$ intensities in the oxidized TiN region, based on comparison to a reference TiO_2 film.

Sample	**$^{16}O^+$ (counts/sec)**	**$^{50}Ti^+$ (counts/sec)**	**$^{16}O^+/^{50}Ti^+$ (counts/sec)**	**Ti : O stoichiometry**
TiO_2 reference	552	5540	0.0996	
1 min	501	5040	0.0995	1 : 2.00
2 min	346	3502	0.0988	1 : 1.99
5 min	399	4026	0.0990	1 : 1.99

Figure 5.3 (a) shows the SI profiles for the sample oxidized for 1 min. In the positive mode, once stabilized, the $^{16}O^+$ and the $^{50}Ti^+$ intensities are steady throughout the oxide region until the interface between the oxide and the nitride, where the intensities quickly drop. Significantly lower intensities have been observed for both the $^{16}O^+$ and the $^{50}Ti^+$ in the nitride region; for the case of $^{50}Ti^+$ it is due to a lower ionization probability in the TiN region, and, for the case of $^{16}O^+$, it is most likely due to some unavoidable oxygen and/or organic contamination of the same mass. Both profiles drop off sharply after the interface between the TiN and Si. In the negative mode, the $^{14}N^-$ profile shows an increase in intensity by one order of magnitude in the TiN regions relative to the background intensity, corresponding to the TiN thickness. It may be noted that the profile slopes of the $^{48}Ti^-$ and $^{14}N^-$ profiles are more gradual as compared to those of $^{50}Ti^+$ and $^{16}O^+$. It appears that the $^{48}Ti^-$ and $^{14}N^-$ profiles have gone some

apparent depth into the Si substrate, while the $^{50}Ti^{+}$ and $^{16}O^{+}$ profiles drop off more quickly. This is due to the knock-on effect where atoms from the outer layers are knocked deeper into the film and subsequently into the substrate due to the significantly higher primary Cs^{+} ion beam energy of 14.5 keV in the negative mode relative to 5.5 keV in the positive mode. The most interesting observation is at the $^{48}Ti^{-}$ profile just before the interface between the oxide and nitride regions, where a noticeable peak at the interface (highlighted in the figure) shows an increase in the ionization probability of the emitted Ti atoms. This peak shows an obvious increase in the intensity that is not observed in any of the other profiles. This oxygen deficient layer is approximately 20 nm thick, which is in agreement with the observation made in TEM in Figure 5.2 (d). Similar profiles have been observed in the samples oxidized for 2 min and 5 min in Figures 5.3 (b) and (c), respectively, with a small peak in the $^{48}Ti^{-}$ profile just before the interface between the oxide and nitride regions.

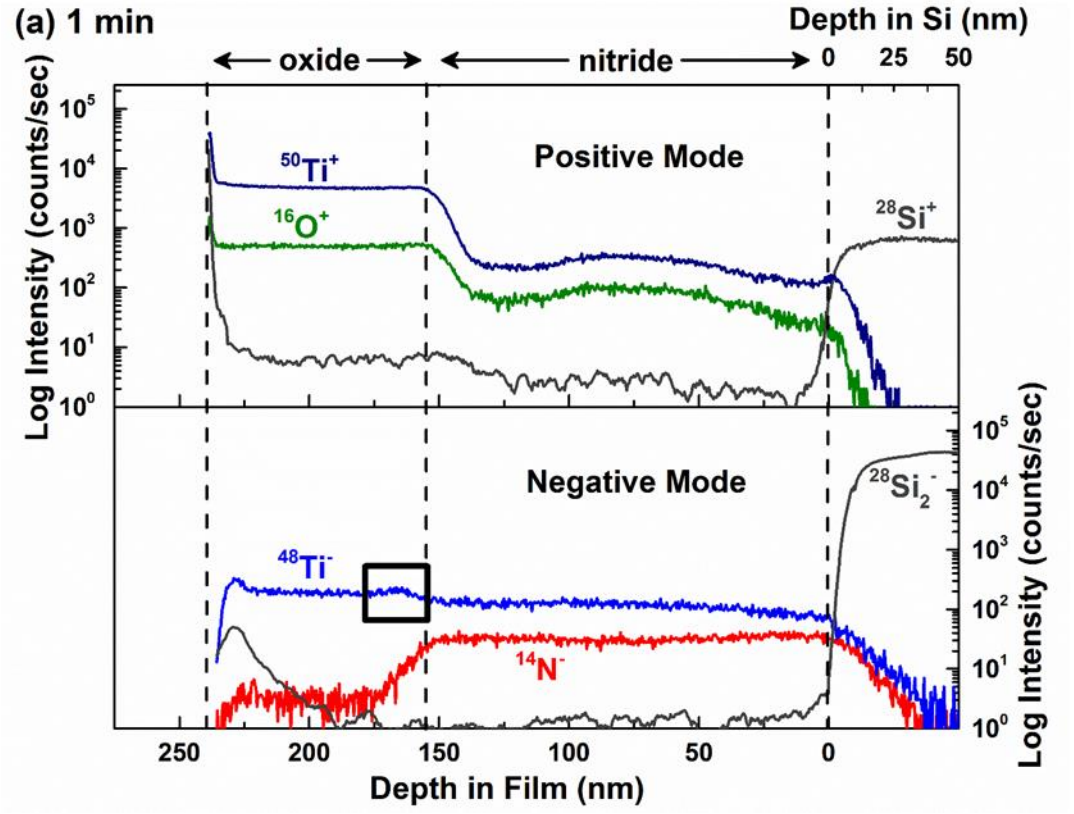

FIG. 5.3 SIMS profiles for the samples oxidized for (a) 1 min, (b) 2 min, and (c) 5 min. The ion mass is given in the superscript preceding the element name, while the "+" or "-" in the superscript following it denotes the charge of the emitted ion. The primary ion beam consisted 13 nA Cs^+ ions at 5.5 keV for the positive mode and 14.5 keV for the negative mode.

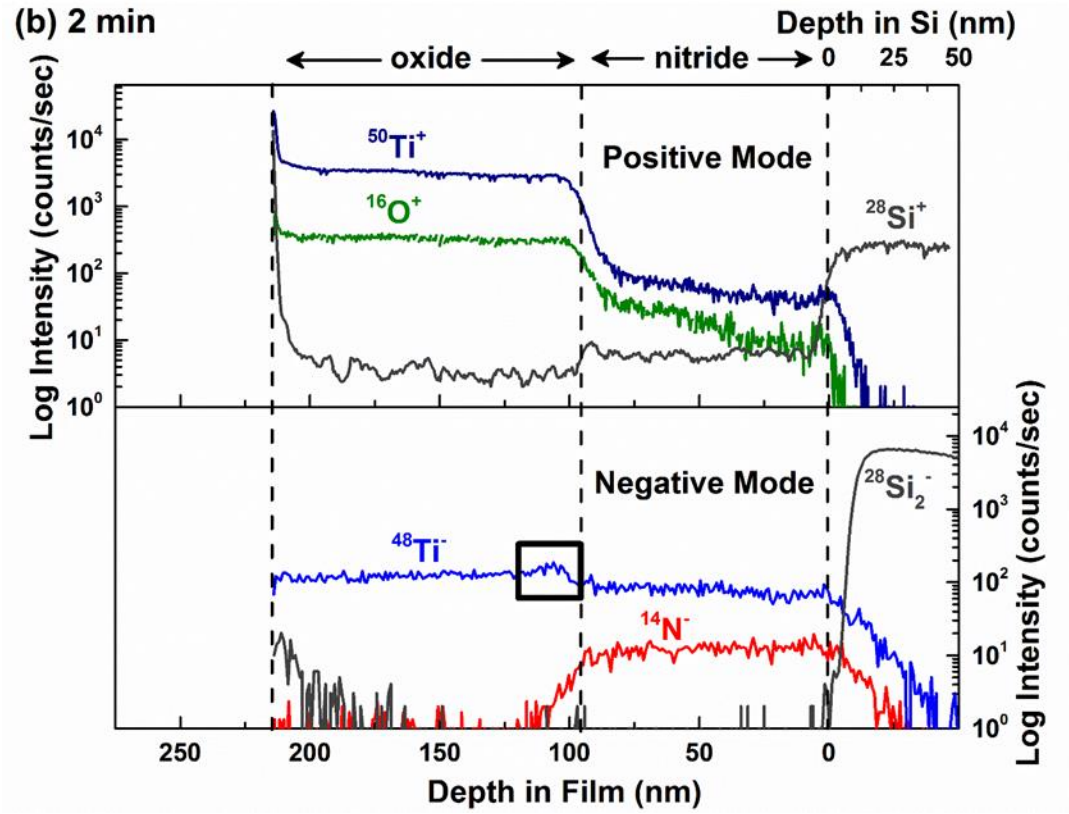

FIG. 5.3 Continued.

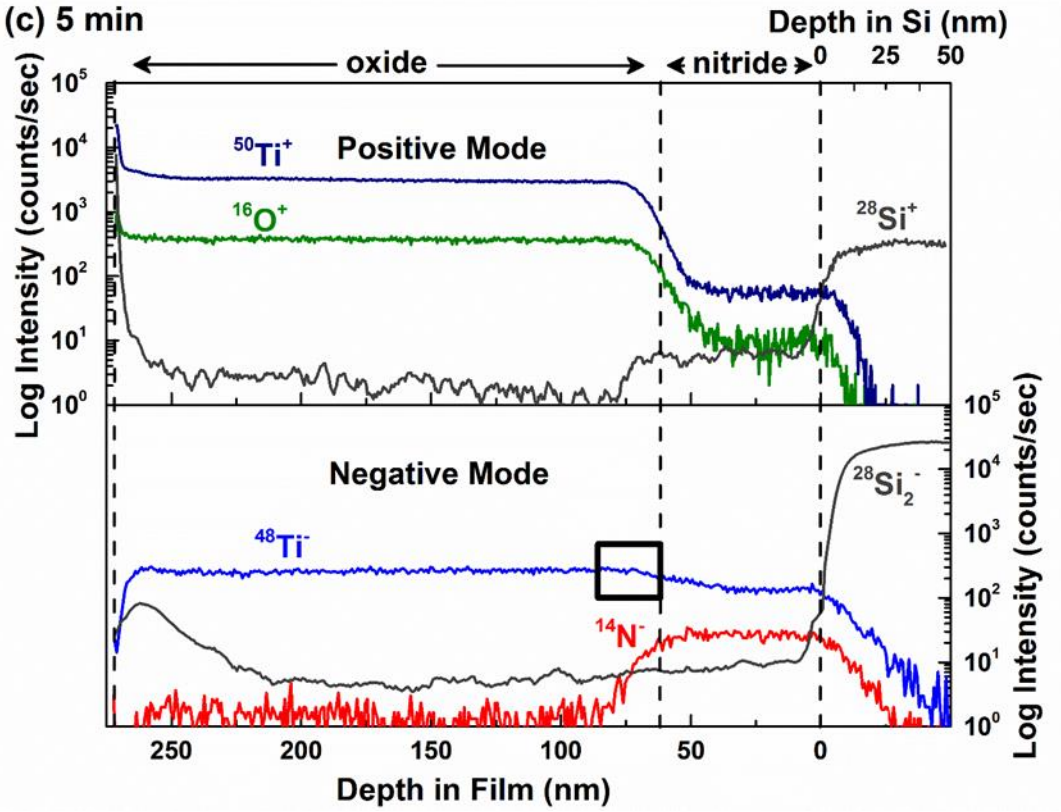

FIG. 5.3 Continued.

5.4.4 Electrical characterization

Figure 5.4 (a) and (b) show the I-V characteristics of all three samples in the linear and log scale, respectively. It is noted that all three films show characteristics typical of bipolar non-filamentary resistive switching[84]. A positive (SET) voltage switches the device from the high resistance state (HRS) to the low resistance state (LRS), while a negative (RESET) voltage switches the device back to the HRS. The diode-like current behavior at the positive and negative biases can be attributed to the

work functions of the top and bottom electrodes[200] or to the thermodynamic reactions at the oxide/electrode interface[77]. The magnitude of, both, the LRS and HRS state currents decreases as a function of increasing oxidation time, while the SET / RESET voltages increase as 2.8 V / -1.4 V, 3.3 V / -2.5 V, and 3.9 V / 3 V, for the 1 min, 2 min and 5 min samples, respectively. The resistance of the LRS and HRS differs by an order of magnitude for the films oxidized for 1 min and by almost two orders of magnitude for the films oxidized for 2 and 5 min. Most importantly, none of the samples show any need for the preliminary electroforming step or forming voltage. Shown in Fig. 5.4 (c), is the HRS and LRS retention data for all three samples up to a time of 10^5 s. All three samples show consistent retention of the HRS and LRS. The 2 min oxidized sample shows the best results based on the long term retention HRS/LRS ratio.

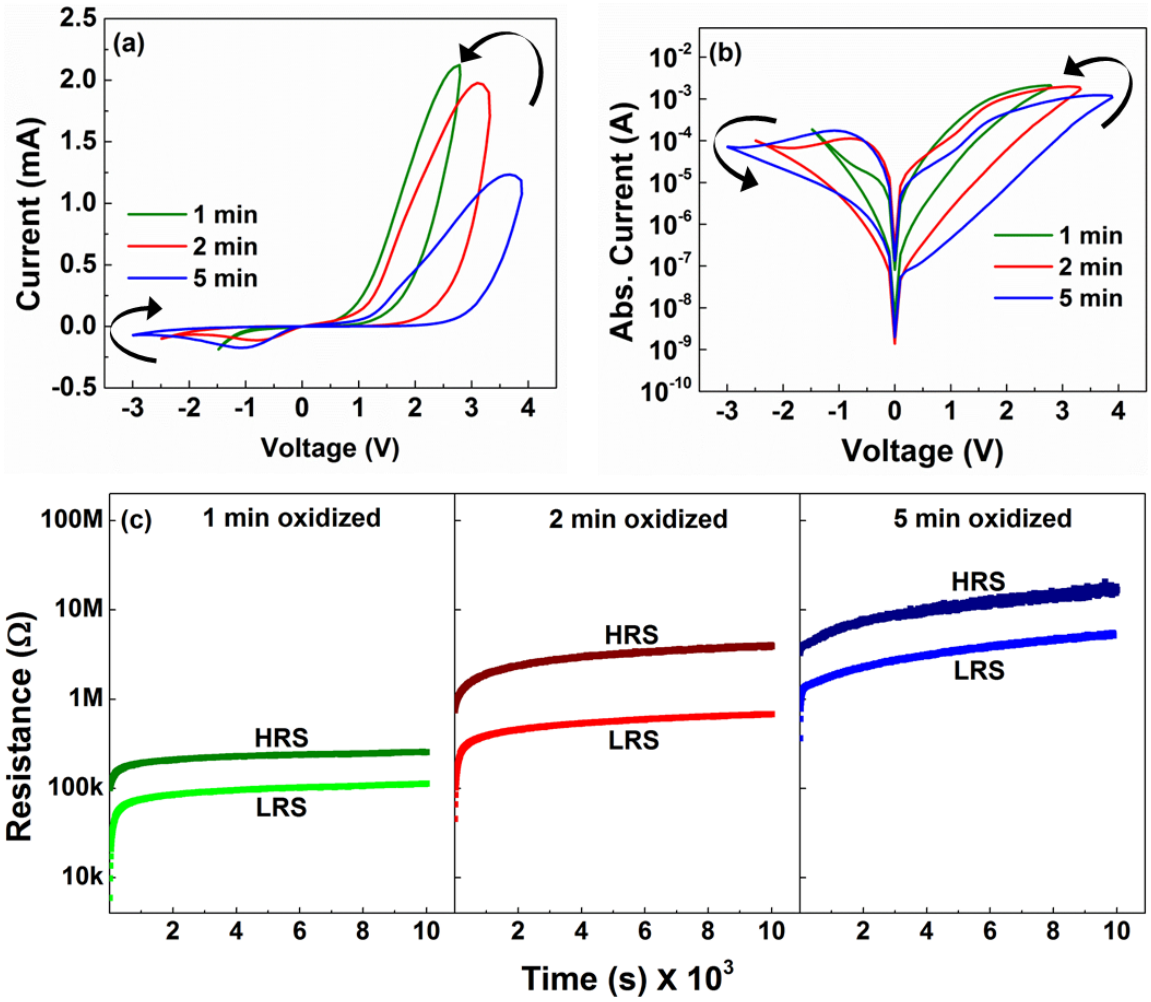

FIG. 5.4 I-V hysteresis curves for all samples plotted on the (a) linear scale and (b) logarithmic scale. All samples display bipolar resistive switching and all films are forming-free. (c) HRS and LRS retention data for all three samples.

5.4.5 Discussion

We believe that the elimination of the need for the forming voltage is because of the presence of the oxygen deficient layer. It has been demonstrated that an amorphous 30 nm thick oxygen deficient layer serves as a source of oxygen vacancies, while the switching occurs primarily in the amorphous 5 nm thick stoichiometric/insulating region.[80] A previous study on the resistive switching in a plasma oxidized TiN film showed the formation of an amorphous 4 nm TiO_{2-x} layer with an amorphous ~26 nm TiN_xO_y layer at the interface between the oxide and nitride regions, with an electroforming step required to initiate the switching process.[201] In both cases, the SET/RESET voltages were lower (~ ±1 V). In our case the thickness of the oxide layer is ~10 times greater and higher SET/RESET voltages (~ ±3 V) are observed, while the current is on a similar order of magnitude. This indicates that though our polycrystalline films are considerably thicker, a similar electric field strength is required, and the presence of grain boundaries provides paths for oxygen vacancy diffusion and current conduction. While the plasma oxidized thin film still required a forming voltage, it was avoided in our case, in spite of a far greater film thickness.

From the results presented, it is apparent that having a double layer film consisting of an oxygen deficient TiO_{2-x} layer and a near stoichiometric TiO_2 layer can eliminate the need for the electroforming step. In addition, the resistive switching and current conduction can be further impacted by the crystalline quality of the film. To further this study, the crystalline quality of the TiO_2 layer can be varied along with that

of the oxygen deficient layer. It is also possible that the SET/RESET voltages could be reduced for thinner films. For this purpose, future work on thinner films can be conducted by this unique growth and thermal oxidation combined method by better controlling the combination of annealing temperature, oxygen ambient conditions, and oxidation times.

5.5 Conclusions

We have successfully demonstrated forming-free resistive switching in TiO_2 films fabricated by *in situ* thermal oxidation of thick epitaxial TiN films for three different oxidation periods. In all cases, a near stoichiometric polycrystalline TiO_2 layer is formed, whose thickness increases as the oxidation time increases. A 20 nm thick oxygen deficient layer is formed at the interface between the oxide and nitride region that acts as a source of oxygen vacancies. All three samples are of polycrystalline quality that presents conduction paths along grain boundaries, thus all samples show forming-free bipolar resistive switching, regardless of oxide film thickness.

CHAPTER VI

GROWTH AND CHARACTERIZATION OF VERTICALLY ALIGNED NANOCOMPOSITES OF BARIUM TITANATE AND ZINC OXIDE

6.1 Overview

Vertically aligned nanocomposite films of $BaTiO_3$-ZnO have been deposited on $SrTiO_3$ substrates and $SrTiO_3$/TiN buffered Si substrates by pulsed laser deposition. X-ray diffraction and transmission electron microscopy characterization show that the films consist of distinct (00*l*) oriented $BaTiO_3$ and $(11\bar{2}0)$ oriented ZnO phases. Polarization hysteresis measurements show that the films are ferroelectric at room temperature and show some evidence of resistive switching. The properties of the films grown on Si substrates are comparable to those grown on $SrTiO_3$. Energy dispersive X-ray spectroscopy measurements show that the Ba/Ti cation stoichiometry can be tuned by controlling the laser fluence and the oxygen partial pressure during deposition, which can directly impact the ferroelectric response. This work is the first demonstration of an epitaxial vertically aligned nanocomposite film of $BaTiO_3$ and ZnO.

6.2 Introduction

There has been a growing interest in heterostructures based on $BaTiO_3$ (BTO), a ferroelectric perovskite insulating semiconductor, and ZnO, a wide-bandgap piezoelectric wurtzite semiconductor.[202-208] In bilayer BTO/ZnO structures, the interfacial charge coupling between the electrically reversible spontaneous polarization in BTO and the permanent spontaneous polarization and a piezoelectric polarization in ZnO biases the ferroelectric switching in BTO.[202] Additionally, trapped charges at the BTO/ZnO interface create a space-charge layer, resulting in an asymmetric charge distribution and giving rise to an internal electric field that further influences the switching characteristics.[203] For multilayer structures, this coupling of the polarization can occur at multiple interfaces.[202,205] Metal-ferroelectric insulator-semiconductor devices based on BTO/ZnO bilayer structures show permanent on/off switching with on/off current ratios as high as 10^6.[208] Resistive switching devices based on BTO/ZnO displayed resistive hysteresis at negative voltage biases, which disappeared at temperatures beyond the BTO Curie temperature of 125 ^oC, indicating that the hysteresis was related to the ferroelectric polarization.[207] It would thus be of interest to investigate the effects of vertical coupling of BTO and ZnO on their electrical and optical properties.

Vertically aligned nanocomposite (VAN) systems are an emergent class of self-assembled thin film architectures consisting of two immiscible phases, which show periodic vertical growth of alternating nanoscale heteroepitaxial domains. The unique

architecture of these structures, owing to their high surface area to volume ratio, allows for very precise tuning of their mechanical, electronic, and magnetic properties through vertical strain. This gives rise to interesting interfacial coupling of those properties for advanced functionalities in a variety of applications like solid oxide fuel cells, ferroelectrics, spintronic devices, multiferroics, electrically tunable dielectrics, and superconductors.[108,110,111,113-115] Moreover, by careful selection of buffer layers, it is possible to integrate these VAN systems onto Si substrates, rather than the typically used single crystal oxide substrates like $SrTiO_3$, $LaAlO_3$, and MgO.[112,118] However, to date, there have been no reports of BTO and ZnO grown in a VAN architecture. In this study, we report the deposition and characterization of BTO-ZnO VAN films on STO substrates and STO/TiN buffered Si substrates, with emphasis on film growth.

6.3 Experimental

All films were deposited in a vacuum chamber with a base pressure of approximately 10^{-7} Torr at a temperature of 700 ^{o}C by pulsed laser deposition (PLD) using a Lambda Physik Compex Pro 205 KrF excimer laser (λ = 248 nm). The TiN and STO targets used for PLD were hot-pressed stoichiometric TiN and STO, respectively, purchased from Plasmaterials, Inc. The BTO-ZnO (1:1 molar ratio) and $SrRuO_3$ (SRO) targets were custom made from powders purchased from Alfa Aesar. The substrates used for deposition were STO (001) and Si (001) purchased from MTI Corporation and Desert Silicon, Inc., respectively. The Si substrates were subjected to a 5 min buffered oxide etch to strip the native oxide prior to loading in the vacuum chamber. The TiN

seed layer was deposited under vacuum at a pulse rate of 10 Hz. The STO buffer and SRO bottom electrode were deposited at a pulse rate of 5 Hz and at an oxygen partial pressure of 40 mTorr. The pulse rate for the BTO-ZnO films was 5 Hz, while the laser fluence was varied from 1.31 J/cm^2 to 0.66 J/cm^2, and the oxygen partial pressure was varied from 100 mTorr to vacuum. The films were annealed immediately following the deposition at a temperature of 500 ^{o}C for 30 mins and an oxygen partial pressure of 500 Torr. 100 nm thick Au top contacts of 0.1 mm^2 area, were deposited on the BTO-ZnO film surface in a custom-built magnetron sputtering system using a 99.99% pure Au sputter target from Williams Advanced Materials.

X-ray diffraction (XRD) spectra were measured using a PANalytical Empyrean 2 diffractometer. Transmission electron microscopy (TEM), scanning tunneling electron microscopy (STEM), and electron diffraction images were acquired using a FEI Tecnai G2 F20 ST FE-TEM. Ferroelectric polarization-electric field hysteresis (P-E) measurements were performed using a TF Analyzer 1000 with leakage current compensation from aixACCT Systems GmbH. Current-voltage (I-V) measurements were conducted using an Agilent E4980A Precision LCR meter. Energy dispersive x-ray spectroscopy (EDS) measurements were acquired on a JEOL JSM-7500F scanning electron microscope equipped with an Oxford EDS system.

6.4 Results and discussion

6.4.1 Formation of a two phase structure

First, a detailed microstructural characterization was conducted on the BTO-ZnO films grown directly on single crystalline STO substrates to verify that a two-phase structure could be achieved. Figure 6.1 shows the XRD spectra of the BTO-ZnO samples deposited at an oxygen partial pressure of 40 mTorr, and a laser fluence of (a) 1.31 J/cm^2, (b) 1.05 J/cm^2, (c) 0.9 J/cm^2, (d) 0.82 J/cm^2, (e) 0.66 J/cm^2, and (f) 0.56 J/cm^2. In Figure 6.1 (a), the film deposited at 1.31 J/cm^2 shows clear peaks for BTO (00*l*), but no peaks associated with ZnO. The film grown at a fluence of 1.05 J/cm^2 in Figure 6.1 (b), shows clear peaks for BTO (00*l*) and a distinct peak for wurtzite ZnO ($11\bar{2}0$) suggesting that both phases have grown epitaxially. In Figures 6.1 (c) and (d), the intensity of the ZnO ($11\bar{2}0$) peak decreases with decreasing laser fluence, and completely disappears in Figures 1 (e) and (f). Moreover, in Figures 6.1 (d)-(f) a small peak appears, corresponding to either $ZnTiO_3$ (021) or an intermediate phase of BTO and ZnO, which is undesirable. Comparing the ZnO and BTO peak intensities, the highest ratio was obtained for the sample deposited at a laser fluence of 1.05 J/cm^2, which was selected for further depositions.

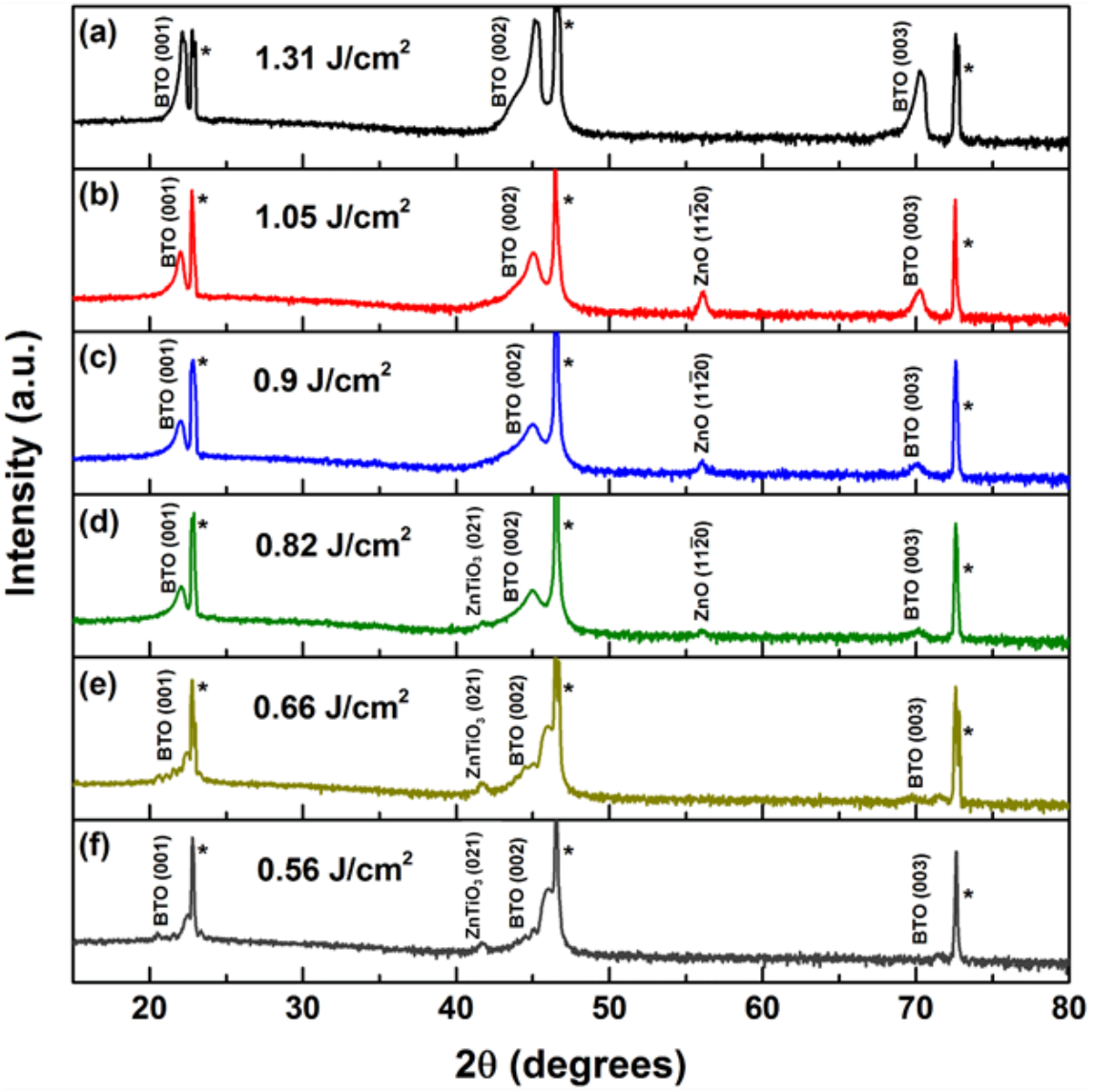

FIG. 6.1 Comparison of the XRD θ-2θ scans for BTO-ZnO films deposited at 40 mTorr as a function of laser fluence.

6.4.2 Microstructure characterization on STO and Si

Following the deposition of BTO-ZnO films directly on STO, a second set of films was deposited on STO and STO/TiN buffered Si substrates at a laser fluence of 1.05 J/cm^2 and an oxygen partial pressure of 40 mTorr with a 15 nm thick SRO layer to serve as the bottom electrode for electrical measurements. The XRD pattern for the film grown on STO in Figure 6.2 (a), shows distinct peaks for BTO (*00l*) and ZnO ($11\bar{2}0$), as previously observed in Figure 6.1 (b). Since the XRD patterns were obtained after Au top contacts had been deposited, some peaks associated with polycrystalline Au are also observed. The inset in Figure 6.2 (a) shows the ϕ-scans for the BTO and ZnO relative to the STO substrate. Comparing the ϕ-scans of the STO (110), BTO (110), and ZnO ($10\bar{1}0$) planes, the four peaks for the BTO phase overlap exactly with the four sharp peaks for the STO substrate, indicating that the BTO phase has grown in cube-on-cube form on the STO substrate. There are four ZnO peaks that are offset from the STO peaks by 45^o, indicating that the ZnO phase has two in-plane orientations, ±45^o, relative to the STO substrate. There appear to be two variations within each of the two orientations of the ZnO; each of the four ZnO ($10\bar{1}0$) peaks have two sub-peaks at 40^o and 50^o, indicating there is a ±5^o deviation from the exact 45^o. The in-plane orientation again

shows that the BTO and ZnO have grown as two distinct phases and that there is no obvious intermixing between the two phases. The out-of-plane matching relationship is determined to be $(001)_{BTO} \| (11\bar{2}0)_{ZnO} \| (001)_{STO}$, while the in-plane relationships are found to be $(110)_{BTO} \| (0001)_{ZnO} \| (110)_{STO}$ and $(\bar{1}10)_{BTO} \| (0001)_{ZnO} \| (\bar{1}10)_{STO}$, respectively. Similarly, for the BTO-ZnO film grown on STO/TiN buffered Si in Figure 6.2 (b), distinct peaks are observed for BTO (*00l*) and wurtzite ZnO ($11\bar{2}0$). A small peak corresponding to BTO (110) is also observed, indicating that the BTO phase is highly textured rather epitaxial and that the film quality is not as good as the film grown on the STO substrate. This is most likely due to a poorer quality of the STO buffer layer as compared to the single crystal STO substrate. The ϕ-scans of the Si (110), STO (110), BTO (110), and ZnO ($10\bar{1}0$) planes, in the inset in Figure 6.2 (b), show cube-on-cube growth for BTO and STO relative to the Si. The ZnO shows two orientations at $\pm 45^{o}$ relative to the Si, as well as a $\pm 5^{o}$ deviation from the 45^{o}, as observed in the films grown on STO.

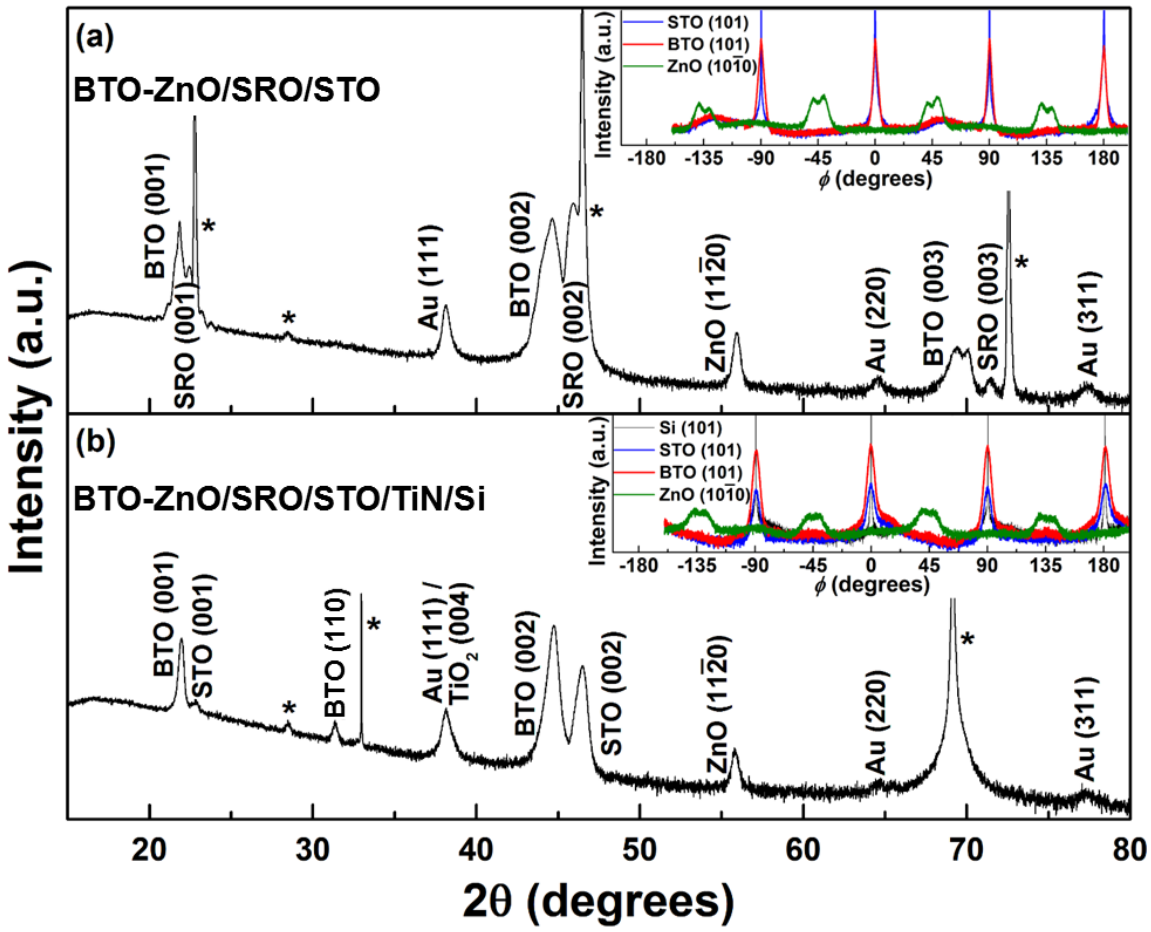

FIG. 6.2 (a) XRD θ-2θ scan of the for BTO-ZnO films grown on STO ("*" = substrate/background peak). The inset shows the ϕ-scans of the BTO (101) and ZnO (10$\bar{1}$0) planes relative to the STO (101) planes. (b) XRD θ-2θ scan of the for BTO-ZnO films grown on STO/TiN buffered Si ("*" = substrate/background peak). The inset shows the ϕ-scans of the BTO (101), STO (101), and ZnO (10$\bar{1}$0) planes relative to the Si (101) planes.

Figures 6.3 (a)-(d) show the TEM images of the BTO-ZnO films grown on STO substrates at a laser fluence of 1.05 J/cm^2 and an oxygen partial pressure of 40 mTorr. The low magnification cross-section TEM image is shown in Figure 6.3 (a), with the inset for the corresponding SAED pattern. The 280 nm thick BTO-ZnO layer obvious columnar growth and the SRO bottom electrode is 17 nm thick. The distinct diffraction dots from all the film layers in the SAED pattern confirm the high quality epitaxial growth of the VAN films. The high resolution TEM image in Figure 6.3 (b) shows vertical columns with thicker BTO columns of 20-40 nm and narrower ZnO columns of 3-10 nm. Figure 6.3 (c) shows the plan-view STEM image of the sample in high angle annular dark-field mode (Z-contrast image, where the image contrast is proportional to $Z^{1.7}$). The BTO-ZnO film shows distinct domains of the BTO (lighter contrast) and ZnO (darker contrast) phases, confirming the column dimensions of both phases, i.e. 20-40 nm for the BTO and 3-10 nm for the ZnO. It is apparent that the ZnO phase is confined to the interfaces between adjacent BTO columns, especially at the junction between 3-4

BTO columns. As observed in the ϕ-scans, the smaller ZnO domains have two orientations in-plane, $\pm 45^{o}$. The high resolution plan-view TEM image in Figure 6.3 (d), again shows that the columns are epitaxial. The TEM images for the films grown on STO/TiN buffered Si substrates are shown in Figure 6.3 (e)-(f). The cross-section TEM image in Figure 6.3 (e) shows the interface between the BTO-ZnO film, the buffer layers, and the Si substrate; the SAED pattern is shown in the inset. The column widths for the BTO and ZnO are similar to those observed in the films grown on STO. The buffer layer thicknesses are 11 nm for the TiN and 40 nm for the STO, while the SRO bottom electrode is 17 nm thick. The TiN, STO, and SRO have epitaxial growth with sharp interfaces and no intermixing, except for a thin (3-4 nm) layer of SiO_x formed at the TiN/Si interface most likely during the deposition or substrate heating prior to deposition. Figure 6.3 (f) shows that the interface between adjacent BTO and ZnO columns is sharp, while the columns themselves are highly epitaxial.

FIG. 6.3 TEM micrographs for BTO-ZnO films grown on (a)-(d) STO and (e)-(f) STO/TiN buffered Si substrates. (a) Low-resolution cross-section image of showing the BTO-ZnO film grown on STO with the inset showing the corresponding SAED pattern; (b) high-resolution image showing vertically aligned nanocolumns of BTO and ZnO; (c) plan-view dark-field STEM image showing the larger BTO nanocolumns ("B", ligther contrast) and smaller ZnO nanocolumns ("Z", darker contrast); (d) high-resolution plan-view image showing a ZnO column between several larger BTO columns. e) Low-resolution cross-section image of showing the BTO-ZnO film grown on Si with the inset showing the corresponding SAED pattern and (f) high resolution image showing the interface between vertically aligned nanocolumns of BTO and ZnO.

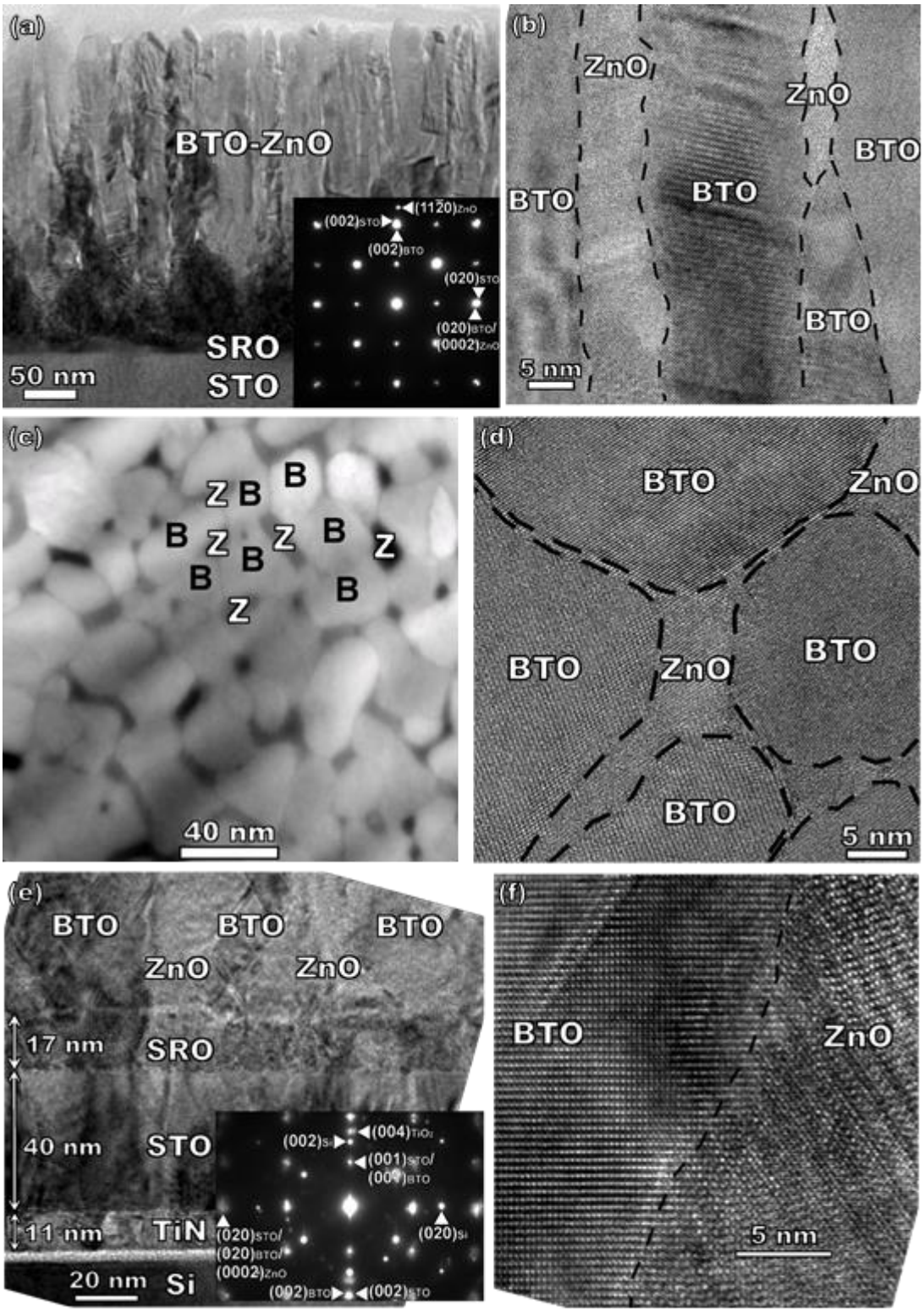
(a)
BTO-ZnO
SRO
STO
50 nm
(002)STO
(11$\bar{2}$0)ZnO
(002)BTO
(020)STO
(020)BTO/
(0002)ZnO
(b)
ZnO
ZnO
BTO
BTO
BTO
BTO
5 nm
(c)
Z B
B
B Z B Z B Z
B
B
Z
40 nm
(d)
BTO
ZnO
BTO
ZnO
BTO
BTO
5 nm
(e)
BTO
BTO
BTO
ZnO
ZnO
17 nm
SRO
40 nm
STO
11 nm
TiN
20 nm
Si
(002)Si
(004)TiO2
(001)STO/
(001)BTO
(020)Si
(020)STO/
(020)BTO/
(0002)ZnO
(002)BTO
(002)STO
(f)
BTO
ZnO
5 nm

6.4.3 Electrical characterization on STO and Si

Figure 6.4 presents a comparison study of the electrical properties measured for the BTO-ZnO films grown on STO and STO/TiN buffered Si at a laser fluence of 1.05 J/cm^2 and an oxygen partial pressure of 40 mTorr. In Figure 6.4 (a) the leakage current for the samples on both substrates is comparable, though fairly high. More importantly, it is interesting to observe that both samples display resistive switching. Figure 6.4 (b) shows the polarization hysteresis loop measured on the samples at 1 kHz at room temperature. Both samples show a weak ferroelectric response, which is similar for both samples, indicating that the films on both substrates are of similar quality. The ferroelectric response is lower than that of reports of pure BTO deposited on STO and Si, however, the films are ferroelectric at room temperature.

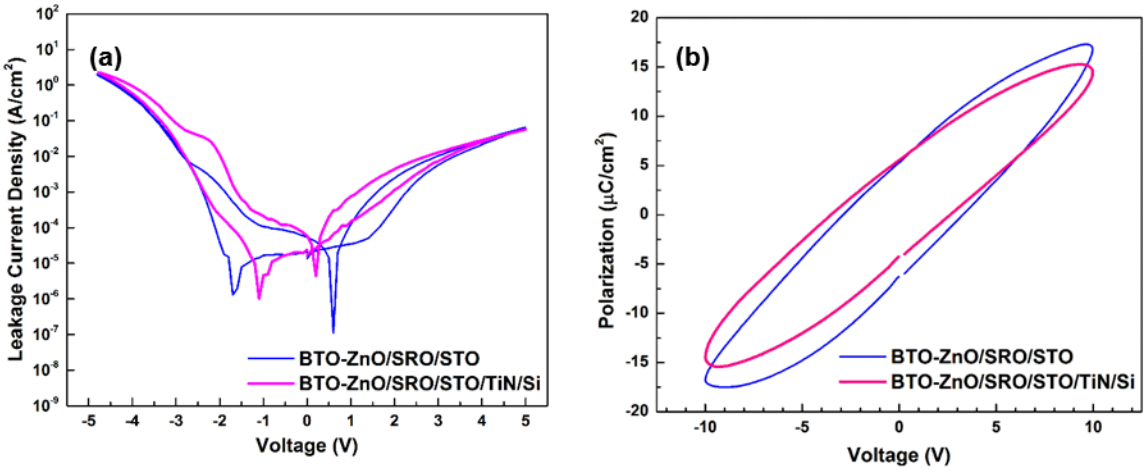

FIG. 6.4 (a) Leakage current and (b) polarization hysteresis measurements on BTO-ZnO films deposited on STO and STO/TiN buffered Si substrates.

6.4.4 Effect of oxygen partial pressure

A third set of samples was deposited on STO substrates with an SRO bottom electrode to investigate the effect of the oxygen partial pressure during deposition. The oxygen partial pressure was varied as 100 mTorr, 40 mTorr, 5 mTorr, and vacuum during the deposition. The post deposition anneal was eliminated. Shown in Figure 6.5 is a summary of the electrical properties for the BTO-ZnO films as function of oxygen partial pressure during deposition. The films deposited under vacuum were very leaky, so those data are not included in this report. Figure 6.5 (a) shows the leakage current for all three samples. The 40 mTorr sample, shows some evidence of resistive switching, as observed in Figure 6.4 (a). However, this behavior is absent from the 100 mTorr and 5 mTorr samples. In Figure 6.5 (b), the polarization hysteresis results measured at 1 kHz show a clear trend as a function of oxygen partial pressure. The 5 mTorr sample shows the best hysteresis loop, followed by the 40 mTorr sample, and then the 100 mTorr sample. This indicates that the ferroelectric response is optimal for low oxygen partial pressures, it decreases with an increase in the oxygen partial pressure, and is not measureable for vacuum deposition conditions. Moreover, it also shows that it is possible to improve the ferroelectric response of the BTO-ZnO system by tuning the deposition parameters.

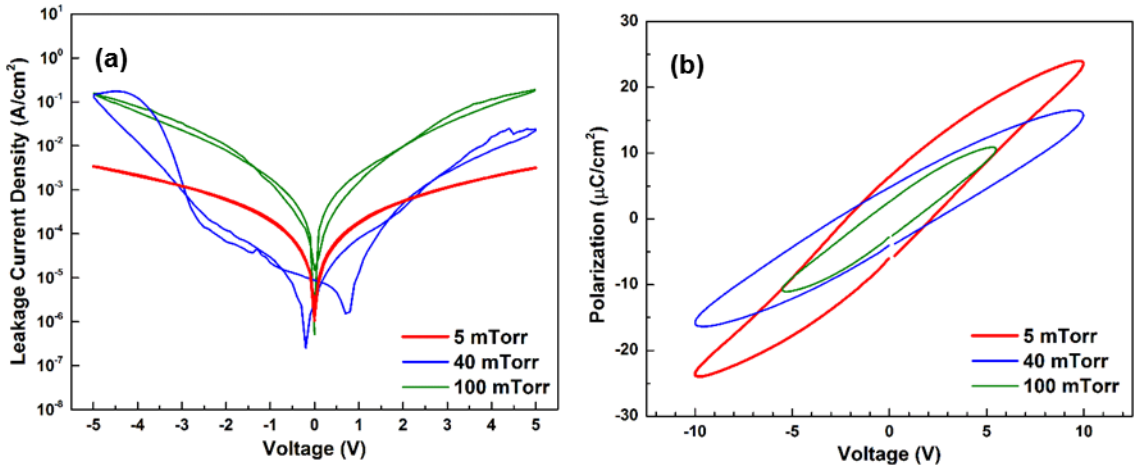

FIG. 6.5 (a) Leakage current and (b) polarization hysteresis measurements on BTO-ZnO films deposited on STO substrates as a function of oxygen partial pressure.

The results presented above indicate that laser fluence and oxygen partial pressure are important parameters that strongly influence the growth and quality of the BTO-ZnO films. To verify the effect of the laser fluence and oxygen partial pressure on the cation stoichiometry of BTO in the BTO-ZnO samples investigated thus far, a composition analysis was performed by EDS, the results of which are summarized in Figure 6.6. Due to possible measurement errors, this data must be considered qualitatively rather than quantitatively. The change in the Ba/Ti atomic ratio as a function of laser fluence (at an oxygen partial pressure of 40 mTorr) is shown in Figure 6.6 (a). There is an obvious trend of a decrease in the Ba/Ti ratio with increasing laser fluence, with the exception of the data point at 0.82 J/cm^2, which is most likely an outlier. In Figure 6.6 (b), the variation of the Ba/Ti ratio due to the oxygen partial pressure (at a laser fluence of 1.05 J/cm^2) shows a decrease in the Ba/Ti ratio with

increasing oxygen pressure. This also matches the result in Figure 6.5 (b) that shows a decrease in the ferroelectric response with increasing oxygen pressure.

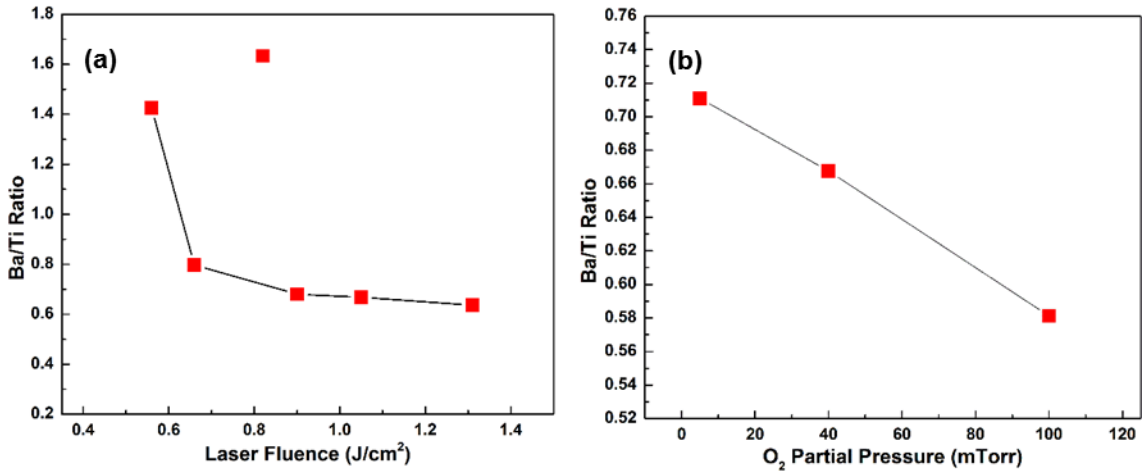

FIG. 6.6 The variation of the Ba/Ti cation stoichiometry in the BTO-ZnO films as a function of (a) laser fluence at an oxygen partial pressure of 40 mTorr and (b) oxygen partial pressure during deposition at a laser fluence of 1.05 J/cm^2.

6.4.5 Discussion

It has been demonstrated that the properties of BTO films deposited by PLD are modulated by their deposition parameters, especially the laser fluence and oxygen partial pressure, both of which affect the kinetic energy of the ablated species.[62-65,209-211] Since our system includes ZnO as a second phase, the dynamics of the ablated species during deposition is more complex. The relationship between the Ba/Ti ratio to the laser

fluence, observed in Figure 6.6 (a) is in agreement with a previous study on the dependence of the Ba/Ti ratio on the laser fluence, in which it was observed that low laser fluences resulted in Ba-rich films and higher laser fluences produced stoichiometric BTO films which had the optimal ferroelectric response.[62] The oxygen partial pressure was kept constant at 20 mTorr. Regarding the effect of oxygen pressure, however, there are mixed opinions in published literature. One study reported ideal stoichiometry in films deposited at low pressures less than 7.5 mTorr, Ti deficiency in films deposited in the intermediate range of 7.5-75 mTorr, and Ba deficiency at pressures higher than 75 mTorr.[63] Conversely, another study found that oxygen pressures greater than 75 mTorr yielded Ti-deficient films.[64] The ideal Ba/Ti stoichiometry was achieved at oxygen pressures in the range of 15-75 mTorr.[64] In a more recent work, it was reported that $BaTiO_3$ films are Ba-rich at a low oxygen pressure of 5 mTorr, stoichiometric at 40 mTorr, and Ti-rich at higher pressures,[65] a trend which is also observed in Figure 6.6 (b). All three groups used a laser fluence of 2 J/cm^2.

Tuning the deposition parameters could also modulate the stoichiometry between the BTO and ZnO phases. To expand on this work, a more detailed study must be performed to include the ZnO phase. The ferroelectric response could be improved by varying the BTO-ZnO composition, in addition to the deposition parameters to optimize the VAN structure. The piezoelectric and optical properties of the structure must also be investigated; due to the piezoelectric and optoelectronic nature of ZnO, some unique functionalities could be realized, that would ultimately be incorporated into Si-based devices.

6.5 Conclusions

We have successfully demonstrated, for the first time, a two-phase VAN film consisting of epitaxial and highly textured BTO and ZnO STO and STO/TiN buffered Si substrates, respectively. Electrical characterization shows that the films grown on both substrates exhibit similar properties and, more importantly, that they are ferroelectric at room temperature. The ferroelectric response can be improved by tuning the oxygen pressure during deposition. Composition analysis shows that both the laser fluence and the oxygen partial pressure can modulate the Ba/Ti cation stoichiometry which, in turn, impacts the ferroelectric properties. This study is a preliminary step in incorporating ferroelectric semiconductor materials with optically active piezoelectric semiconductors in a VAN architecture, paving the way for the realization of novel functionalities that can be integrated on Si.

CHAPTER VII

DIFFUSION BARRIER PROPERTIES OF NITRIDE FILMS ON FUEL CLADDING*

7.1 Overview

In this work, titanium nitride (TiN) and zirconium nitride (ZrN) coatings are proposed as diffusion barriers between stainless steel nuclear fuel cladding and lanthanide fission products. TiN and ZrN have been coated as barrier materials between pure Fe and Ce, i.e. diffusion couples of Fe/TiN/Ce and Fe/ZrN/Ce, annealed up to a temperature of 600 ^{o}C, and compared to the diffusion behavior of uncoated Fe/Ce. Backscattered electron images and energy dispersive X-ray spectroscopy measurements confirm that, with a 500 nm TiN or ZrN layer, no obvious diffusion is observed between Fe and Ce. Basic diffusion characteristics of the Fe/Ce couple have also been measured and compared with the TiN and ZrN coated ones. These preliminary results strongly advocate that TiN and ZrN coatings may be feasible as diffusion barriers against Ce and possibly other lanthanide fission products.

---

*This chapter is reprinted with permission from "Diffusion barrier properties of nitride-based coatings on fuel cladding" by F F. Khatkhatay, J. Jian, L. Jiao, Q. Su, J. Gan, J. I. Cole, and H. Y. Wang, Journal of Alloys and Compounds, **580**, 442 (2013).

7.2 Introduction

The progress of advanced nuclear reactors, including molten salt, fast burner, supercritical water, and high temperature reactors, relies heavily on the development of fuel cladding technologies[212,213] that isolate the fuel from the coolant in the reactor core. Currently, ferritic and martensitic stainless steels are being considered as fuel cladding materials for many of these reactors, designed for coolant operating temperatures less than 600 ^{o}C in the reactor core.[212,213] A phenomenon that threatens the integrity of the cladding, called fuel-cladding chemical interaction (FCCI), occurs at elevated temperatures due to the swelling of the metallic fuel and its contact with the cladding surface under irradiation. In addition, lanthanide fission products migrating to the interface between the fuel and the cladding also contribute to this phenomenon. FCCI can result in eutectic melting and phase formation, thinning of the cladding (termed wastage), and lowered mechanical stability of the structure.[213-215] The implementation of a diffusion barrier (or a liner), on the cladding surface in contact with the fuel, could help mitigate FCCI.[214,216] For such a diffusion barrier to be successful, it should tolerate high radiation doses and temperatures, resist interaction with both the cladding and the fuel, and have a good thermal conductivity.[214,217]

TiN, a refractory metal nitride ceramic, is a promising candidate as a diffusion barrier. It has high melting temperature, excellent exhibited ion-irradiation tolerance, high thermal conductivity, and high hardness.[131,133,135,136] TiN thin films have increased resistance to erosion and corrosion and have found numerous industrial applications.[191]

In addition, TiN has been demonstrated as an excellent diffusion barrier against copper diffusion into silicon substrates, and has been used extensively in the integrated circuit fabrication industry.[192] Our previous study on TiN based coatings on stainless steel shows that they have superior mechanical stability,[216] e.g., no delamination, cracking, or obvious change in hardness was observed between as-deposited and thermal-cycle tested samples; no adhesive or cohesive failure occurred when the samples were scratch tested, which indicates that the films had good adhesion to the substrates. Chemical vapor deposition (CVD) of diamond on pure Fe, a 25 nm thick layer of TiN was shown to prevent carbon diffusion into the Fe substrates, but no mention was made about the diffusion of carbon or Fe into the TiN layer.[218,219] In another study, TiN coatings, formed by CVD, on nickel-containing cemented carbide substrates, showed that some nickel was incorporated into the TiN film; this occurrence was attributed to either gas phase nickel compounds in the reaction zone, liquid phase nickel that seeped between the TiN nuclei, or nickel diffusion into the TiN grains.[220] A ZrN, also a refractory nitride, has melting temperature, thermal conductivity, and hardness properties similar to those of TiN [133]. Moreover, ZrN has very low neutron absorption and zirconium based alloys are currently used as fuel cladding in commercial nuclear power plants [221]. A 500 nm ZrN layer has been shown to prevent diffusion between palladium, a platinum group metal, and stainless steel.[222] However some Fe diffused into the ZrN,[222] and therefore TiN is expected to perform better than ZrN.

However, to date, there is no report on the diffusion barrier properties of TiN or ZrN against lanthanide fission products that form in irradiated metallic fuels. In our

previous study, no obvious diffusion was found between HT-9, a martensitic stainless steel cladding material, and Ce, a representative lanthanide, using a thin TiN barrier.[216] A concern remains that the diffusion of Ce in stainless steel could be difficult and therefore no obvious diffusion was observed. For this reason, a baseline of an Fe/Ce diffusion couple was selected for this study. The baseline Fe/Ce diffusion couple has been previously studied with clear diffusion observed at temperatures ranging from 425 ^{o}C to 785 ^{o}C.[223,224] In this work, TiN and ZrN, each 500 nm in thickness, have been independently deposited between the Fe and Ce to compare the diffusion interaction of the coated Fe/Ce couple to that of the baseline Fe/Ce diffusion couple.

7.3 Experimental

500 nm thick TiN and ZrN films were deposited on 1 mm thick Fe bars by pulsed laser deposition (PLD) using a Lambda Physik Compex Pro 205 KrF excimer laser (λ = 248 nm). The TiN and ZrN targets used for PLD were hot-pressed stoichiometric TiN and ZrN, purchased from Plasma Materials, Inc. The Fe substrates (99.99 % in purity, Alfa Aesar) were cut into 0.25 inch × 0.125 inch pieces and polished prior to deposition. The deposition details are provided elsewhere.[216] The Ce sheets were 99.9 % in purity (American Elements, Inc.) preserved in mineral oil to prevent oxidation. The Ce sheets were thoroughly cleaned to remove any surface contamination and cut to match the size of the Fe substrates. The diffusion couples were assembled by sandwiching the Ce sheet between two Fe samples, one bare and the other coated, in a custom-made stainless steel

clamp, shown in Figure 7.1. The assembly process was conducted in a glove box to avoid oxidation and contamination.

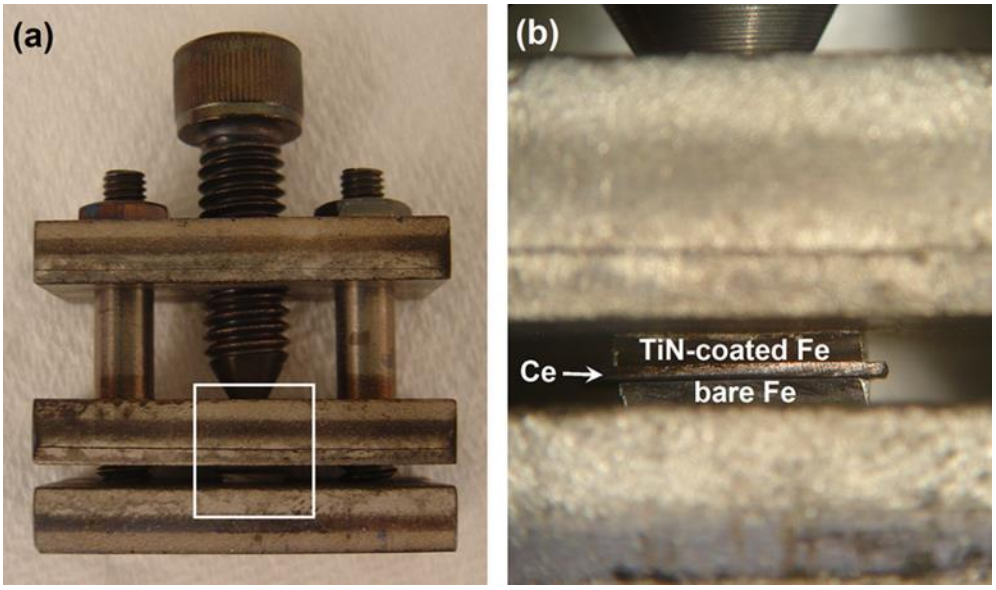

FIG. 7.1 (a) Diffusion couple sandwich in stainless steel clamp; (b) higher magnification of region highlighted in (a) clearly showing the TiN-coated-Fe bar, Ce sheet, and the bare Fe bar.

The diffusion couples were annealed in a high vacuum quartz tube furnace (Barnstead/Thermolyne F21135). The annealing temperatures were varied as 500 ^{o}C, 550 ^{o}C, 575 ^{o}C, and 600 ^{o}C, with a ramp rate of 10 ^{o}C/min at a pressure of 10^{-6} Torr. The annealing time was controlled at either 12 h or 24 h. After annealing, the sample was polished to expose the cross-section of the coated Fe / Ce / bare Fe sandwich and to ensure a smooth surface. Backscattered electron (BSE) images and energy dispersive X-

ray spectroscopy (EDS) measurements were conducted using a JEOL JSM-7500F scanning electron microscope (SEM) equipped with an Oxford EDS system.

7.4 Results and discussion

7.4.1 Bare Fe/Ce interface

Figure 7.2 shows the cross-section SEM/BSE images of the interface of the bare Fe/Ce couples annealed at different temperatures and durations. In Figure 7.2 (a) the BSE image for the Fe/Ce couple after annealing at 500 ^{o}C for 24 h shows that there is obvious diffusion on both sides of the interface and it is difficult to identify the exact location of the Fe/Ce interface. Figure 7.2 (b), (c), and (d) are the BSE images of the bare Fe/Ce interface annealed at 550 ^{o}C for 24h, 550 ^{o}C for 12 h, and 575 ^{o}C for 12 h, respectively. As in the 500 ^{o}C 24 h case, all the images show that there is evident diffusion across both sides of the interface. As the temperature and time increase, the diffusion depth correspondingly increases. The bare Fe/Ce couple annealed at 600 ^{o}C had severe interdiffusion and melting, due to which the diffusion depths could not be reasonably determined on either side of the interface. This is believed to have occurred due to the eutectic point at $Fe_{0.836}Ce_{0.164}$ and 592 ^{o}C in the Fe/Ce phase diagram.[225] Therefore, the bare Fe/Ce diffusion data for the 600 ^{o}C annealing has been excluded from the following discussion. It may be noted in all the BSE images, that there are microstructural features as well as black particles apparent on the surface of the sample that are more prominent on the Ce side of the diffusion couple rather than the Fe side.

They are the result of polishing residue that became embedded in the relatively soft Ce, as well as unavoidable oxidation of the Ce surface once the cross-section was exposed.

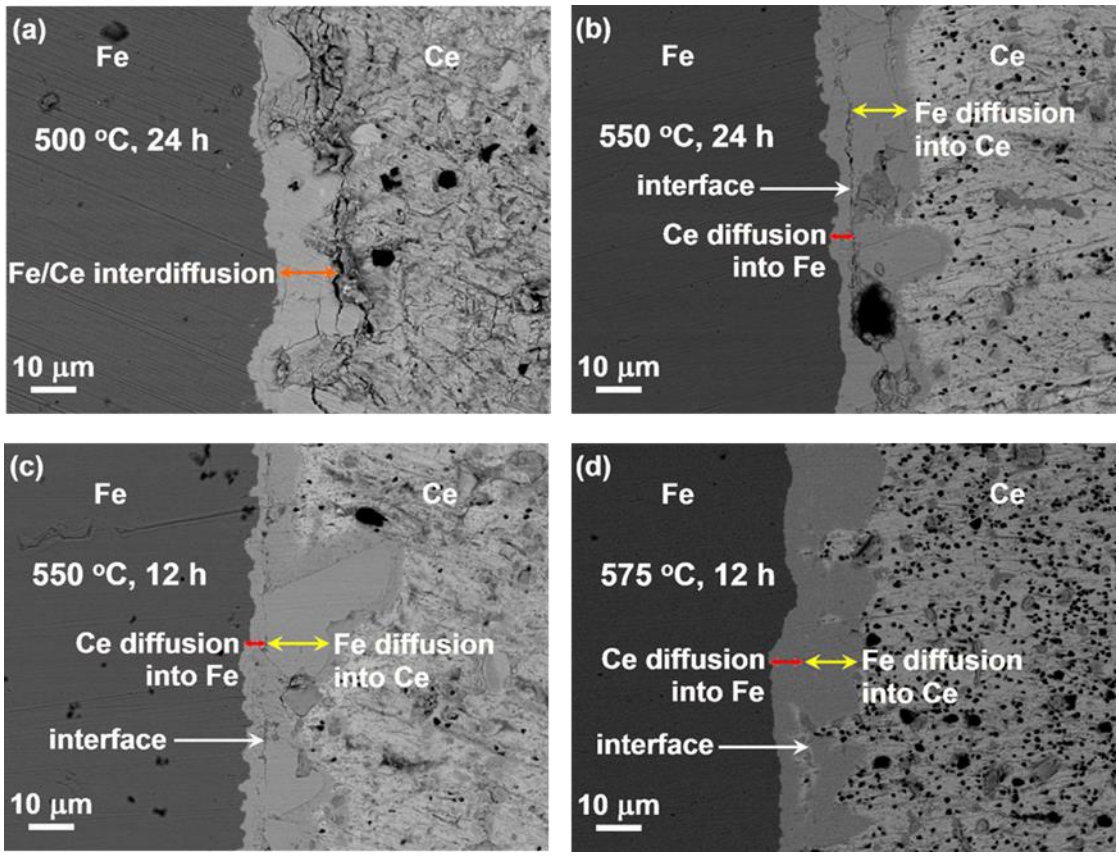

FIG. 7.2 Cross-section of the bare Fe/Ce interface for different annealing conditions: (a) 500 °C for 24 h, (b) 550 °C for 24 h, (c) 550 °C for 12 h, and (d) 575 °C for 12 h.

7.4.2 TiN-coated Fe/Ce interface

Contrary to the case of the bare Fe/Ce diffusion couples in Figure 7.2, the SEM/BSE images of the annealed TiN-coated Fe/Ce interface in Figure 7.3 show that there is no obvious diffusion across the interface in the presence of the 500 nm thick TiN layer under all the temperatures and durations tested. In Figure 7.3 (a), the interface of the couple annealed at 500 ^{o}C for 24 h shows that there is no evidence of diffusion. The dark contrast of the TiN layer is clearly visible between the lighter contrast of the Fe and considerably lighter contrast of the Ce. Figure 7.3 (b), (c), and (d) are the BSE images of the couples annealed at 550 ^{o}C for 24 h, 575 ^{o}C for 12 h, and 600 ^{o}C for 24 h, respectively. All images show that there is no obvious diffusion across the Fe/TiN/Ce interface. As shown in the higher magnification inset in Figure 7.3(d), the interface is still clean and abrupt after annealing at 600 ^{o}C for 24 h.

7.4.3 ZrN-coated Fe/Ce interface

Figure 7.4 shows the cross-section SEM/BSE images of the Fe/Ce interface with the ZrN coating, annealed at different temperatures and durations. Figure 7.4 (a), (b), and (c) are the BSE images for the Fe/ZrN/Ce diffusion couple after annealing at 500 ^{o}C for 24 h, 550 ^{o}C for 24 h, 575 ^{o}C for 12 h, and 600 ^{o}C for 24 h, respectively. The inset in Figure 7.4 (d) shows the interface at a higher magnification. The intermediate contrast of the ZrN is clearly visible between the dark contrast of Fe and the considerably lighter contrast of Ce. Similar to the case of the TiN-coated Fe/Ce interface in Figure 7.3, all the

images show that there is no obvious diffusion across the Fe/ZrN/Ce interface, even after annealing for 600 ºC for 24 h.

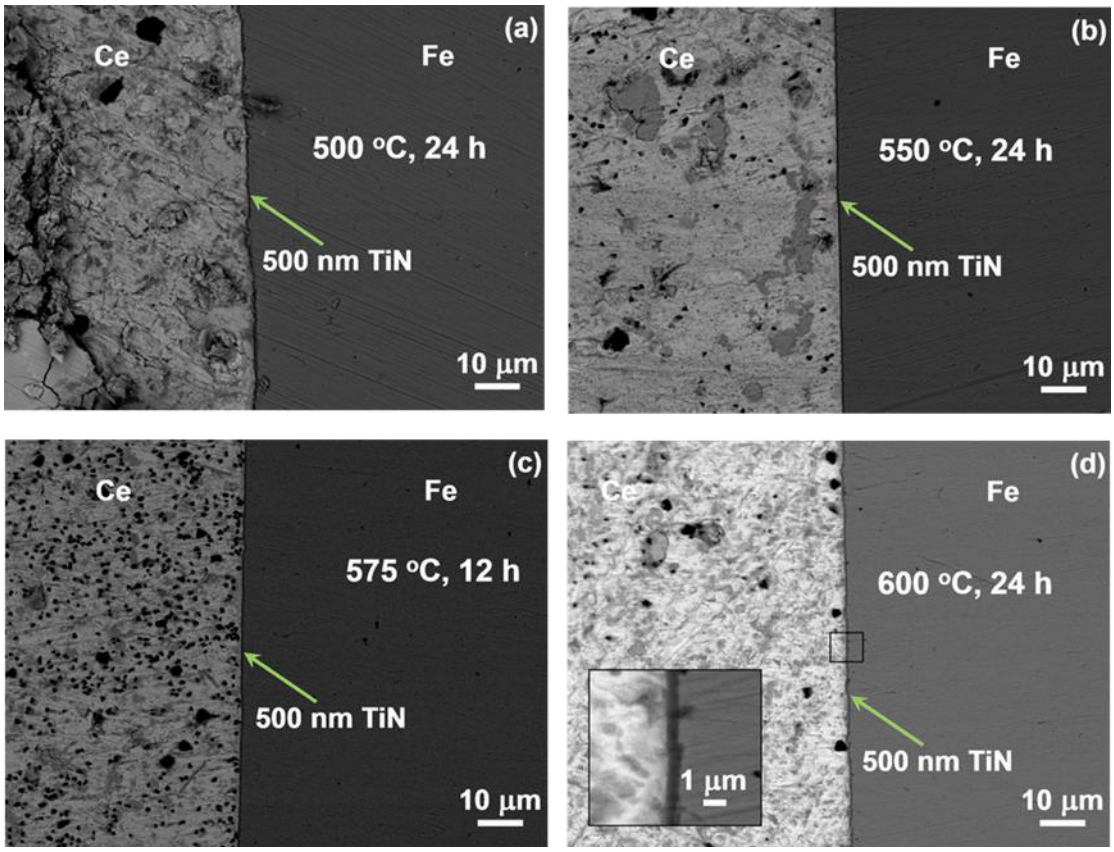

FIG. 7.3 Cross-section of the TiN-coated Fe/Ce interface for different annealing conditions: (a) 500 ºC for 24 h, (b) 550 ºC for 24 h, (c) 575 ºC for 12 h, and (d) 600 ºC for 24 h with the inset showing a clean and sharp interface at higher magnification.

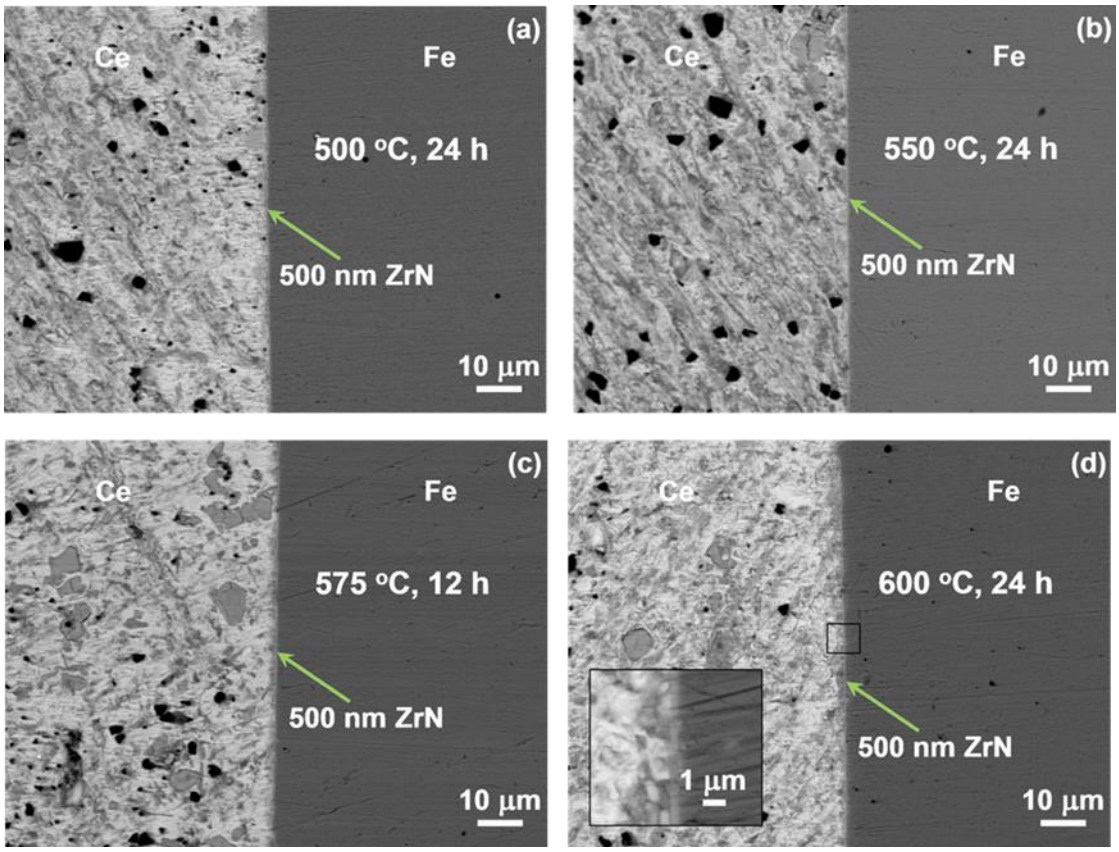

FIG. 7.4 Cross-section of the ZrN-coated Fe/Ce interface for different annealing conditions: (a) 500 °C for 24 h, (b) 550 °C for 24 h, (c) 575 °C for 12 h, and (d) 600 °C for 24 h with the inset showing a clean and sharp interface at higher magnification.

7.4.4 Characterization of the Fe/Ce interdiffusion behavior

The diffusion depths on both sides of the interface for the Fe side of the diffusion couple sandwich were measured for the 550 °C and 575 °C samples. Since the location of the interface for the 500 °C sample could not be determined, the diffusion lengths for

Fe in Ce and Ce in Fe were estimated based on its total interdiffusion length and the ratios of the diffusion lengths of Fe in Ce vs. Ce in Fe for the 550 ºC and 575 ºC samples. The corresponding diffusion coefficients were calculated using Equation 7-1.

$$x = \sqrt{2Dt} \tag{7-1}$$

where x is the diffusion length, D is the diffusion coefficient, and t is the total annealing time.[226] Table 7.1 lists the diffusion lengths and corresponding calculated diffusion coefficients. The tabulated values are averages of 33 measured lengths for each combination of time and temperature.

Table 7.1 Measured diffusion lengths and calculated diffusion coefficients for the bare Fe side of the diffusion couples

		Ce in Fe				**Fe in Ce**			
Anneal Time	Temp	$L_{Ce\ in\ Fe}$ (μm)	StDev	$D_{Ce\ in\ Fe}$ (cm^2/s)	StDev	$L_{Fe\ in\ Ce}$ (μm)	StDev	$D_{Fe\ in\ Ce}$ (cm^2/s)	StDev
24 h	500 ºC	1.86	0.09	2.01E-13	0.20E-13	12.03	0.60	8.37E-12	0.84E-12
24 h	550 ºC	3.60	0.18	7.48E-13	0.75E-13	11.45	0.57	7.59E-12	0.76E-12
12 h	550 ºC	2.69	0.14	8.38E-13	0.84E-13	8.82	0.44	8.99E-12	0.90E-12
12 h	575 ºC	4.59	0.23	2.43E-12	0.24E-13	10.81	0.54	1.35E-11	0.14E-11

The calculated diffusion coefficients from Table 7.1 were compared to those found in published literature and plotted in Figure 7.5 (a). Overall, the experimental data is in agreement with the published data.[223] The experimental data was fit to an Arrhenius relationship given by Equation 7-2.

$$D = D_0 \times exp\left(\frac{-E_a}{kT}\right) \tag{7-2}$$

where D is the diffusion coefficient, D_0 is the diffusivity, E_a is the activation energy, k is Boltzmann's constant, and T is the absolute temperature. The diffusion coefficient and activation energy were calculated from the above data, shown in Fig. 7.5 (b), and listed in Table 7.2.

Table 7.2 Calculated activation energy and diffusivity for Ce in Fe and Fe in Ce

	Ce in Fe	**Fe in Ce**
Activation Energy, E_a (eV)	1.79	0.270
Std. Dev. of E_a (eV)	1E-15	1E-16
Diffusivity, D_0 (cm^2/s)	0.082	4.39E-10
Std. Dev. of D_0 (cm^2/s)	8.2E-3	4.39E-11

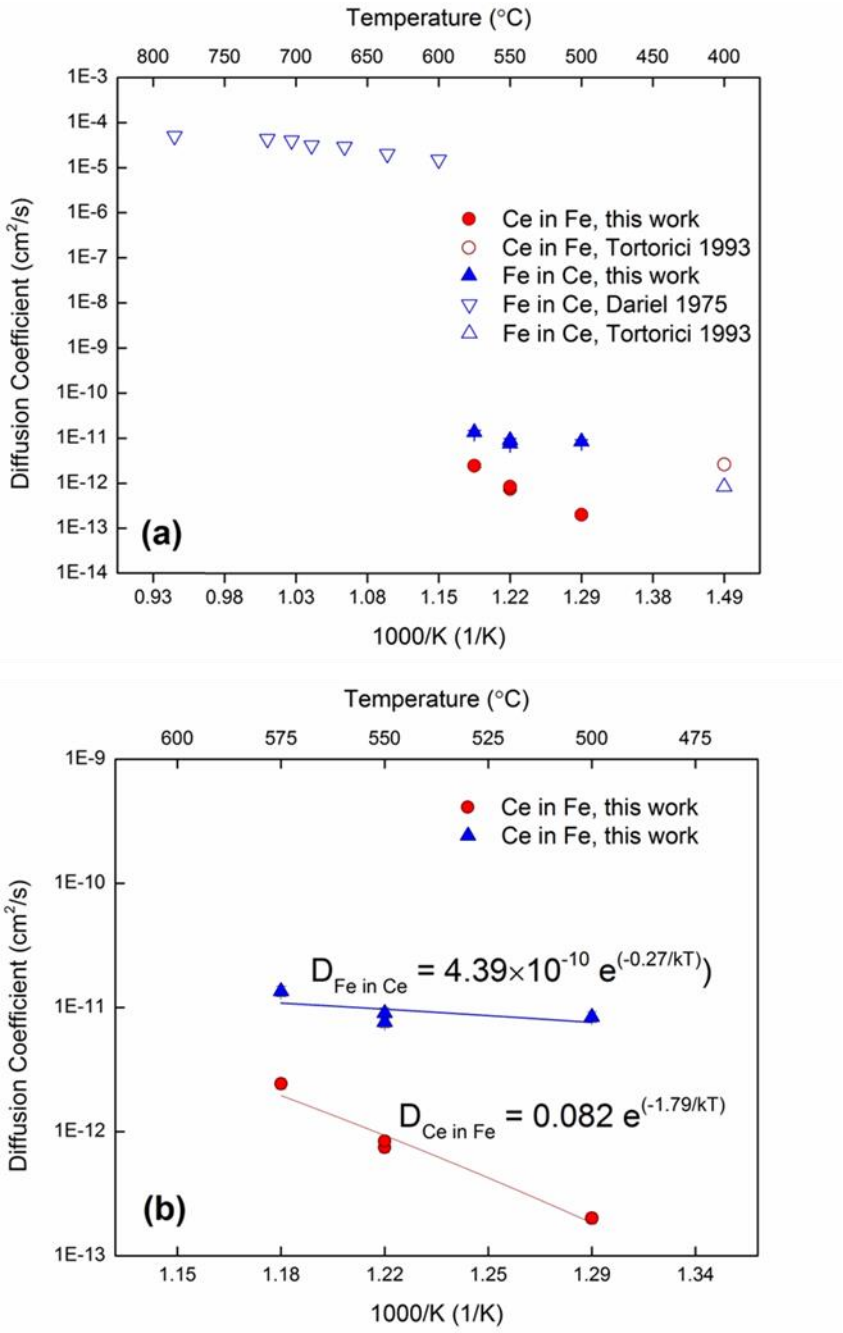

FIG. 7.5 (a) Comparison of calculated diffusion coefficients from this work (solid symbols) with those found in published literature (open symbols); (b) plot of calculated values of diffusivity and activation energy.

So far, very limited work has been published on the interdiffusion behavior of the Fe / Ce system. For example, a radio-isotope tracer diffusion study, which monitored the diffusion of Fe isotopes deposited on Ce,[224] was conducted in the temperature range higher than the reported eutectic temperature of 592 ºC,[225] and no data is below that temperature was reported. Therefore, a large diffusion coefficient of 0.017 ± 0.005 cm^2/s was reported for Fe in Ce, much larger than our results. Additionally, the annealing times were exceedingly short (300 s to 600 s), and radio-isotope tracers of Fe rather than naturally abundant metallic Fe were used as the diffusing species. However, the reported E_a value of 0.516 ± 0.022 eV for Fe diffusion in Ce is close to our findings.[224] The other study on the 425 ºC Fe/Ce diffusion couple[223] shows that the diffusion coefficients are within the same range as our calculations. However, their diffusion coefficient calculated for Ce in Fe (2.6E-12 cm^2/s) was higher than that of Fe in Ce (8.4E-13 cm^2/s), which is the opposite of what we observe. This could be related to different methods in considering reference points for the measurement of diffusion lengths. Moreover, the study was performed at only one temperature, 425 ºC,[223] so no E_a or D_0 was reported, and it is not possible to ascertain whether the trend of $D_{Ce\ in\ Fe} > D_{Fe\ in\ Ce}$ holds for a wider temperature range.

7.4.5 EDS characterization

To verify that TiN and ZrN are indeed effective as diffusion barriers, EDS measurements were conducted across the interface of the Fe/Ce diffusion couples with and without the coating. Figure 7.6 compares the EDS spectrum of the bare Fe/Ce

interface annealed at 550 ^{o}C for 12 h with the spectra of TiN-coated Fe/Ce interface and the ZrN-coated Fe/Ce interface annealed at 600 ^{o}C for 24 h. Figure 7.6 (a) shows the result of the EDS line scan across the bare Fe / Ce interface. Its corresponding BSE image is shown in Figure 7.6 (b). The TiN coated Fe / Ce interface is shown in Figure 7.6 (c) with its corresponding BSE image in Figure 7.6 (d). The ZrN coated Fe / Ce interface is shown in Figure 7.6 (e) with its corresponding BSE image in Figure 7.6 (f). From the line scan it is evident that on the bare Fe side, the composition change is gradual and there is more Fe diffusion into Ce than vice versa. However, there is no indication of diffusion, of either Fe or Ce, to the other side of the interface on either the TiN coated or the ZrN coated Fe side of the couple, and the interface is clean and sharp based on how abruptly the composition profiles drop as the scanned beam crosses the interface. The traces of polishing residue mentioned earlier are also visible in the line scans as variations in the detection levels in the pure Fe and pure Ce regions. The Fe concentration spikes at approximately 7 μm in Figure 7.6 (c) and 10 μm in Figure 7.6 (e) are due to polishing residue embedded in the Ce. Similar spikes were noticed in most of the line scans at varying distances from the interface, but without any correlation to the annealing time or temperature.

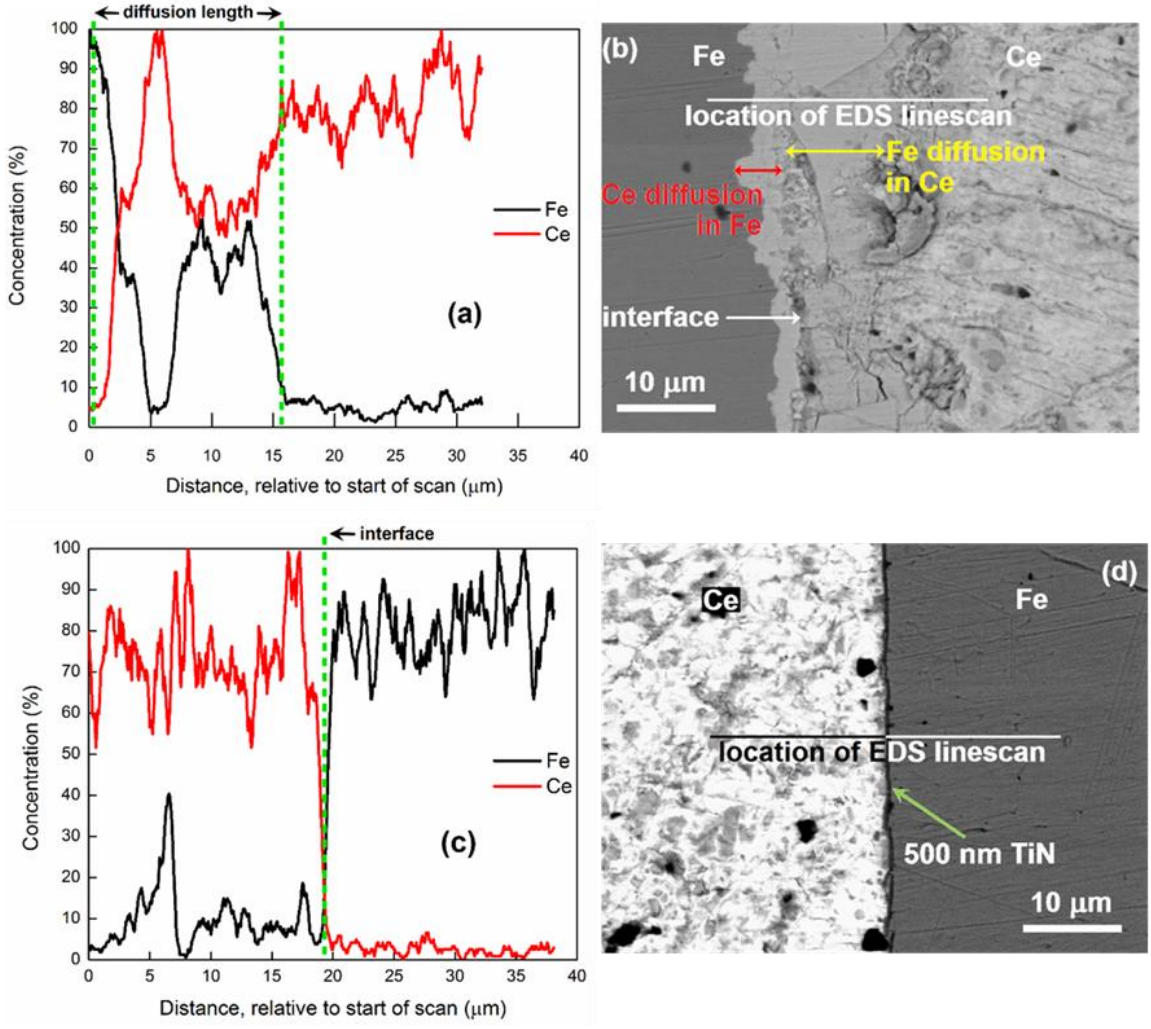

FIG. 7.6 Result of the EDS line scan across the bare Fe / Ce interface and (b) its corresponding BSE image; (c) result of the EDS line scan across the TiN coated Fe / Ce interface and (d) its corresponding BSE image; (e) result of the EDS line scan across the ZrN coated Fe / Ce interface and (f) its corresponding BSE image.

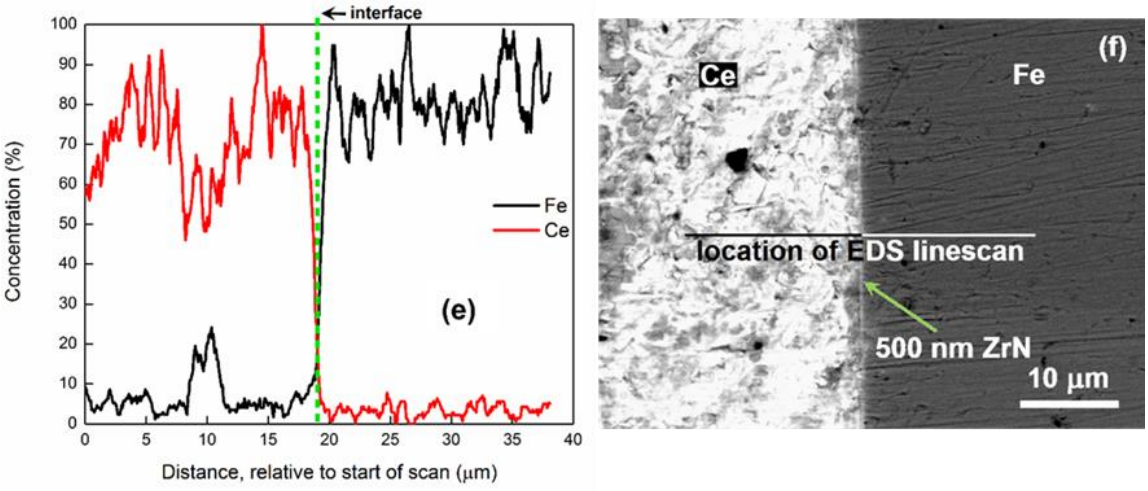

FIG. 7.6 Continued.

7.4.6 Discussion

From the experimental results above, it is obvious that both, TiN and ZrN, serve as excellent diffusion barriers between Fe and Ce up to the maximum temperature tested in this study, 600 ^{o}C. To expand on this study, the film quality of the TiN and ZrN could be further optimized for different film thicknesses in terms of the film's ability to effectively prevent any interaction between the Fe and Ce, so the minimum required film thickness might be determined. Longer annealing times must be tested as well, to investigate the long-term diffusion barrier characteristics of TiN and ZrN. On the other hand, there are other potential candidate diffusion barriers, such as tantalum nitride and aluminum nitride, which could have diffusion barrier properties comparable to those of TiN and ZrN. Additionally, future experiments should also consider a wider temperature

range and longer time periods for the Fe / Ce interdiffusion study for a more accurate E_a and D_0 calculation.

7.5 Conclusions

We have successfully demonstrated the effectiveness of TiN and ZrN thin films as diffusion barriers between Fe and Ce up to the temperature required for technical applications (higher temperatures might be desired for Fe-based oxide dispersion strengthened alloys), and no obvious diffusion was observed in any of the diffusion couples with a nitride coating. We have also conducted a baseline study of the diffusion interaction between Fe and Ce, and the activation energy and diffusivity are calculated to be 1.79 eV and 0.082 cm^2/s respectively for Ce in Fe and 0.27 eV and 4.39E-10 cm^2/s respectively for Fe in Ce. This study provides strong evidence that TiN and ZrN coatings provide reliable diffusion barrier characteristics against Ce and possibly other lanthanide fission products.

CHAPTER VIII

SUMMARY AND FUTURE WORK

In this dissertation, we have investigated property enhancement in prospective materials for next-generation memory devices based on the ferroelectric and resistive switching phenomena. First, we employed the novel two-phase VAN structure for property enhancement in oxide films. For ferroelectric devices, we have incorporated ferroelectric $BaTiO_3$ with CeO_2 in a VAN structure to improve its Curie temperature while maintaining its ferroelectric properties on $SrTiO_3$ substrates. We have replicated the $BaTiO_3$-CeO_2 system on Si using an optimized $SrTiO_3$/TiN double buffer layer to realize similar results on Si. Next, we have demonstrated a simple resistive switching device by *in situ* oxidation of TiN on Si substrates, which is forming-free due to the presence of an oxygen deficient layer near the interface between the oxide and nitride regions. Furthermore, we have successfully grown a VAN system of $BaTiO_3$-ZnO on $SrTiO_3$ and $SrTiO_3$/TiN buffered Si. The ferroelectric properties of the films can be improved by tuning the deposition conditions. Although further work is required to optimize the film properties, this is the first demonstration of an epitaxial VAN system of $BaTiO_3$ and ZnO. Finally, we have demonstrated that, in addition to being an excellent buffer layer for integration of functional oxides on Si, TiN can also be successfully implemented as a diffusion barrier in extreme environments.

We have shown how a vertically aligned structure can improve the ferroelectric properties in $BaTiO_3$ and that the formation of an oxygen deficient region in oxidized

TiN has helped to enhance its resistive switching properties. The next step could be to combine these two findings to study the effects of a VAN structure in resistive switching devices. Future work includes investigation on: (1) the effects of vertical interfaces and vertical strain on the resistive switching properties of the material; (2) the relationship, if any, between the ferroelectric and resistive switching properties; and (3) the effects of deposition conditions on the microstructure and stoichiometry of the individual phases in the VAN systems.

REFERENCES

[1] A. Makarov, V. Sverdlov, and S. Selberherr, Microelectronics Reliability **52,** 628 (2012).

[2] S. A. Wolf, J. W. Lu, M. R. Stan, E. Chen, and D. M. Treger, Proceedings of the IEEE **98,** 2155 (2010).

[3] C. Y. Lin, C. Y. Liu, C. C. Lin, and T. Y. Tseng, Journal of Electroceramics **21,** 61 (2008).

[4] C. N. R. Rao and B. Raveau, *Transition Metal Oxides: Structure, Properties, and Synthesis of Ceramic Oxides*, 2nd ed. (Wiley, New York, 1998).

[5] L. W. Martin, Y. H. Chu, and R. Ramesh, Materials Science & Engineering R **68,** 89 (2010).

[6] J. L. F. Da Silva, M. V. Ganduglia-Pirovano, J. Sauer, V. Bayer, and G. Kresse, Physical Review B **75,** 045121 (2007).

[7] I. Atribak, I. Such-Basaniez, A. Bueno-Lopez, and A. Garcia-Garcia, Journal of Catalysis **250,** 75 (2007).

[8] A. J. Jacobson, Chemistry of Materials **22,** 660 (2010).

[9] L. Malavasi, C. A. J. Fisher, and M. S. Islam, Chemical Society Reviews **39,** 4370 (2010).

[10] U. Diebold, Surface Science Reports **48,** 53 (2003).

[11] V. Swamy, L. S. Dubrovinsky, N. A. Dubrovinskaia, F. Langenhorst, A. S. Simionovici, M. Drakopoulos, V. Dmitriev, and H. P. Weber, Solid State Communications **134,** 541 (2005).

[12] L. S. Dubrovinsky, N. A. Dubrovinskaia, V. Swamy, J. Muscat, N. M. Harrison, R. Ahuja, B. Holm, and B. Johansson, Nature **410,** 653 (2001).

[13] K. S. Narayan and T. B. Singh, Applied Physics Letters **74,** 3456 (1999).

[14] K. Nakata and A. Fujishima, Journal of Photochemistry and Photobiology C **13,** 169 (2012).

[15] H. A. Durand, J. H. Brimaud, O. Hellman, H. Shibata, S. Sakuragi, Y. Makita, D. Gesbert, and P. Meyrueis, Applied Surface Science **86,** 122 (1995).

[16] S. K. Kim, K. M. Kim, D. S. Jeong, W. Jeon, K. J. Yoon, and C. S. Hwang, Journal of Materials Research **28,** 313 (2013).

[17] J. L. G. Fierro, *Metal Oxides: Chemistry and Applications* (Taylor & Francis, Boca Raton, 2005).

[18] U. Ozgur, Y. I. Alivov, C. Liu, A. Teke, M. A. Reshchikov, S. Dogan, V. Avrutin, S. J. Cho, and H. Morkoc, Journal of Applied Physics **98,** 103 (2005).

[19] M. A. Myers, M. T. Myers, M. J. General, J. H. Lee, L. Shao, and H. Wang, Applied Physics Letters **101,** 5 (2012).

[20] M. A. Myers, J. H. Lee, and H. Wang, Materials Letters **100,** 78 (2013).

[21] M. G. Blamire, J. L. MacManus-Driscoll, N. D. Mathur, and Z. H. Barber, Advanced Materials **21,** 3827 (2009).

[22] S. Das and S. Ghosh, Dalton Transactions **42,** 1645 (2013).

[23] G. H. Haertling, Journal of the American Ceramic Society **82,** 797 (1999).

[24] H. Y. Hwang, S. W. Cheong, P. G. Radaelli, M. Marezio, and B. Batlogg, Physical Review Letters **75,** 914 (1995).

[25] K. Uchino, *Ferroelectric devices* (CRC Press, Boca Raton, 2010).

[26] R. D. Clark, Materials **7,** 2913 (2014).

[27] C. Zhao, C. Z. Zhao, S. Taylor, and P. R. Chalker, Materials **7,** 5117 (2014).

[28] S. P. Pavunny, J. F. Scott, and R. S. Katiyar, Materials **7,** 2669 (2014).

[29] M. Suzuki, Materials **5,** 443 (2012).

[30] L. B. Kong, S. Li, T. S. Zhang, J. W. Zhai, F. Y. C. Boey, and J. Ma, Progress in Materials Science **55,** 840 (2010).

[31] D. C. Look, Materials Science and Engineering B **80,** 383 (2001).

[32] A. Janotti and C. G. Van de Walle, Reports on Progress in Physics **72,** 126501 (2009).

[33] X. Chen and S. S. Mao, Chemical Reviews **107,** 2891 (2007).

[34] A. Hirohata and K. Takanashi, Journal of Physics D **47,** 40 (2014).

[35] I. Zutic, J. Fabian, and S. Das Sarma, Reviews of Modern Physics **76,** 323 (2004).

[36] M. B. Salamon and M. Jaime, Reviews of Modern Physics **73,** 583 (2001).

[37] S. Roy and S. B. Majumder, Journal of Alloys and Compounds **538,** 153 (2012).

[38] D. I. Khomskii, Journal of Magnetism and Magnetic Materials **306,** 1 (2006).

[39] S. R. Foltyn, L. Civale, J. L. Macmanus-Driscoll, Q. X. Jia, B. Maiorov, H. Wang, and M. Maley, Nature Materials **6,** 631 (2007).

[40] J. Orenstein and A. J. Millis, Science **288,** 468 (2000).

[41] C. Hammond, *The Basics of Crystallography and Diffraction* (Oxford University Press, New York, 2009).

[42] R. Calio, U. B. Rongala, D. Camboni, M. Milazzo, C. Stefanini, G. de Petris, and C. M. Oddo, Sensors **14,** 4755 (2014).

[43] P. S. Halasyamani, in *Functional Oxides* (John Wiley & Sons, Ltd, Chichester, 2010), p. 1.

[44] S. R. Anton and H. A. Sodano, Smart Materials & Structures **16,** R1 (2007).

[45] K. Uchino, *Advanced Piezoelectric Materials: Science and Technology* (Woodhead Publishing, Philadelphia, 2010).

[46] K. M. Ok, E. O. Chi, and P. S. Halasyamani, Chemical Society Reviews **35,** 710 (2006).

[47] N. Nuraje and K. Su, Nanoscale **5,** 8752 (2013).

[48] E. Aksel and J. L. Jones, Sensors **10,** 1935 (2010).

[49] H. Jaffe, Journal of the American Ceramic Society **41,** 494 (1958).

[50] S. O. Leontsev and R. E. Eitel, Science and Technology of Advanced Materials **11** (2010).

[51] P. K. Panda, Journal of Materials Science **44,** 5049 (2009).

[52] K. Tsuda, R. Sano, and M. Tanaka, Physical Review B **86,** 214106 (2012).

[53] W. J. Lin, T. Y. Tseng, H. B. Lu, S. L. Tu, S. J. Yang, and I. N. Lin, Journal of Applied Physics **77,** 6466 (1995).

[54] V. Vaithyanathan, J. Lettieri, W. Tian, A. Sharan, A. Vasudevarao, Y. L. Li, A. Kochhar, H. Ma, J. Levy, P. Zschack, J. C. Woicik, L. Q. Chen, V. Gopalan, and D. G. Schlom, Journal of Applied Physics **100,** 024108 (2006).

[55] K. J. Choi, M. Biegalski, Y. L. Li, A. Sharan, J. Schubert, R. Uecker, P. Reiche, Y. B. Chen, X. Q. Pan, V. Gopalan, L. Q. Chen, D. G. Schlom, and C. B. Eom, Science **306,** 1005 (2004).

[56] J. Junquera and P. Ghosez, Nature **422,** 506 (2003).

[57] Y. S. Kim, D. H. Kim, J. D. Kim, Y. J. Chang, T. W. Noh, J. H. Kong, K. Char, Y. D. Park, S. D. Bu, J. G. Yoon, and J. S. Chung, Applied Physics Letters **86,** 3 (2005).

[58] G. Gerra, A. K. Tagantsev, N. Setter, and K. Parlinski, Physical Review Letters **96,** 4 (2006).

[59] H. Wu, Y. G. Zhan, H. Z. Xing, and W. Z. Shen, Solid State Communications **149,** 802 (2009).

[60] M. G. Stachiotti, Applied Physics Letters **84,** 251 (2004).

[61] D. Fuchs, M. Adam, P. Schweiss, S. Gerhold, S. Schuppler, R. Schneider, and B. Obst, Journal of Applied Physics **88,** 1844 (2000).

[62] D. S. Kan and Y. Shimakawa, Applied Physics Letters **99,** 081907 (2011).

[63] J. Gonzalo, R. G. San Roman, J. Perriere, C. N. Afonso, and R. P. Casero, Applied Physics A **66,** 487 (1998).

[64] C. L. Li, Z. H. Chen, Y. L. Zhou, and D. F. Cui, Journal of Physics-Condensed Matter **13,** 5261 (2001).

[65] A. P. Chen, F. Khatkhatay, W. Zhang, C. Jacob, L. Jiao, and H. Wang, Journal of Applied Physics **114,** 124101 (2013).

[66] T. Prodromakis, C. Toumazou, and L. Chua, Nature Materials **11,** 478 (2012).

[67] D. B. Strukov, G. S. Snider, D. R. Stewart, and R. S. Williams, Nature **453,** 80 (2008).

[68] L. O. Chua and S. M. Kang, Proceedings of the IEEE **64,** 209 (1976).

[69] J. J. S. Yang, D. B. Strukov, and D. R. Stewart, Nature Nanotechnology **8,** 13 (2013).

[70] F. Pan, S. Gao, C. Chen, C. Song, and F. Zeng, Materials Science & Engineering R **83,** 1 (2014).

[71] R. Waser, Journal of Nanoscience and Nanotechnology **12,** 7628 (2012).

[72] R. Waser, R. Dittmann, G. Staikov, and K. Szot, Advanced Materials **21,** 2632 (2009).

[73] I. Valov and M. N. Kozicki, Journal of Physics D **46,** 074005 (2013).

[74] Z. S. Tang, Y. Q. Chi, L. Fang, R. L. Liu, and X. Yi, Journal of Nanoscience and Nanotechnology **14,** 1494 (2014).

[75] K. Szot, M. Rogala, W. Speier, Z. Klusek, A. Besmehn, and R. Waser, Nanotechnology **22,** 254001 (2011).

[76] S. M. Hong, H. D. Kim, H. M. An, and T. G. Kim, Materials Research Bulletin **48,** 5080 (2013).

[77] J. J. Yang, J. P. Strachan, F. Miao, M. X. Zhang, M. D. Pickett, W. Yi, D. A. A. Ohlberg, G. Medeiros-Ribeiro, and R. S. Williams, Applied Physics A **102,** 785 (2011).

[78] J.-F. Marucco, J. Gautron, and P. Lemasson, Journal of Physics and Chemistry of Solids **42,** 363 (1981).

[79] J. J. Yang, F. Miao, M. D. Pickett, D. A. A. Ohlberg, D. R. Stewart, C. N. Lau, and R. S. Williams, Nanotechnology **20,** 215201 (2009).

[80] J. P. Strachan, J. J. Yang, L. A. Montoro, C. A. Ospina, A. J. Ramirez, A. L. D. Kilcoyne, G. Medeiros-Ribeiro, and R. S. Williams, Beilstein Journal of Nanotechnology **4,** 467 (2013).

[81] K. M. Kim, D. S. Jeong, and C. S. Hwang, Nanotechnology **22,** 17 (2011).

[82] D. H. Kwon, K. M. Kim, J. H. Jang, J. M. Jeon, M. H. Lee, G. H. Kim, X. S. Li, G. S. Park, B. Lee, S. Han, M. Kim, and C. S. Hwang, Nature Nanotechnology **5,** 148 (2010).

[83] J. Y. Chen, C. L. Hsin, C. W. Huang, C. H. Chiu, Y. T. Huang, S. J. Lin, W. W. Wu, and L. J. Chen, Nano Letters **13,** 3671 (2013).

[84] P. R. Mickel, A. J. Lohn, and M. J. Marinella, Modern Physics Letters B **28,** 25 (2014).

[85] J. Narayan and B. C. Larson, Journal of Applied Physics **93,** 278 (2003).

[86] D. G. Schlom, L. Q. Chen, X. Q. Pan, A. Schmehl, and M. A. Zurbuchen, Journal of the American Ceramic Society **91,** 2429 (2008).

[87] Y. Song, H. J. Zhou, Q. X. Xu, J. Luo, H. Z. Yin, J. Yan, and H. C. Zhong, Journal of Electronic Materials **40,** 1584 (2011).

[88] K. J. Kuhn, A. Murthy, R. Kotlyar, and M. Kuhn, ECS Transactions **33,** 3 (2010).

[89] J. P. Locquet, J. Perret, J. Fompeyrine, E. Machler, J. W. Seo, and G. Van Tendeloo, Nature **394,** 453 (1998).

[90] I. Bozovic, G. Logvenov, I. Belca, B. Narimbetov, and I. Sveklo, Physical Review Letters **89,** 4 (2002).

[91] H. Sato, A. Tsukada, and M. Naito, Physica C **408,** 848 (2004).

[92] R. Ghosh, D. Basak, and S. Fujihara, Journal of Applied Physics **96,** 2689 (2004).

[93] D. G. Schlom, L. Q. Chen, C. B. Eom, K. M. Rabe, S. K. Streiffer, and J. M. Triscone, Annual Review of Materials Research **37,** 589 (2007).

[94] A. R. Chaudhuri, M. Arredondo, A. Hahnel, A. Morelli, M. Becker, M. Alexe, and I. Vrejoiu, Physical Review B **84,** 054112 (2011).

[95] C. Daumont, W. Ren, I. C. Infante, S. Lisenkov, J. Allibe, C. Carretero, S. Fusil, E. Jacquet, T. Bouvet, F. Bouamrane, S. Prosandeev, G. Geneste, B. Dkhil, L. Bellaiche, A. Barthelemy, and M. Bibes, Journal of Physics-Condensed Matter **24,** 5 (2012).

[96] Y. S. Kim, J. S. Choi, J. Kim, S. J. Moon, B. H. Park, J. Yu, J. H. Kwon, M. Kim, J. S. Chung, T. W. Noh, and J. G. Yoon, Applied Physics Letters **97,** 242907 (2010).

[97] Y. L. Li, S. Choudhury, J. H. Haeni, M. D. Biegalski, A. Vasudevarao, A. Sharan, H. Z. Ma, J. Levy, V. Gopalan, S. Trolier-McKinstry, D. G. Schlom, Q. X. Jia, and L. Q. Chen, Physical Review B **73,** 13 (2006).

[98] Y. L. Li and L. Q. Chen, Applied Physics Letters **88,** 3 (2006).

[99] C. Ederer and N. A. Spaldin, Physical Review Letters **95,** 257601 (2005).

[100] A. R. James and X. X. Xi, Journal of Applied Physics **92,** 6149 (2002).

[101] J. G. Wu, D. Q. Xiao, J. G. Zhu, J. L. Zhu, J. Z. Tan, and Q. L. Zhang, Applied Physics Letters **90,** 3 (2007).

[102] D. G. Schlom, J. H. Haeni, J. Lettieri, C. D. Theis, W. Tian, J. C. Jiang, and X. Q. Pan, Materials Science and Engineering B **87,** 282 (2001).

[103] J. F. Scott, Science **315,** 954 (2007).

[104] C. H. Ahn, K. M. Rabe, and J. M. Triscone, Science **303,** 488 (2004).

[105] H. Han, Y. Kim, M. Alexe, D. Hesse, and W. Lee, Advanced Materials **23,** 4599 (2011).

[106] P. M. Rorvik, T. Grande, and M. A. Einarsrud, Advanced Materials **23,** 4007 (2011).

[107] O. I. Lebedev, J. Verbeeck, G. Van Tendeloo, O. Shapoval, A. Belenchuk, V. Moshnyaga, B. Damashcke, and K. Samwer, Physical Review B **66,** 104421 (2002).

[108] H. Zheng, J. Wang, S. E. Lofland, Z. Ma, L. Mohaddes-Ardabili, T. Zhao, L. Salamanca-Riba, S. R. Shinde, S. B. Ogale, F. Bai, D. Viehland, Y. Jia, D. G. Schlom, M. Wuttig, A. Roytburd, and R. Ramesh, Science **303,** 661 (2004).

[109] A. P. Chen, M. Weigand, Z. X. Bi, W. R. Zhang, X. J. Lu, P. Dowden, J. L. MacManus-Driscoll, H. Y. Wang, and Q. X. Jia, Scientific Reports **4,** 7 (2014).

[110] A. P. Chen, Z. X. Bi, Q. X. Jia, J. L. MacManus-Driscoll, and H. Y. Wang, Acta Materialia **61,** 2783 (2013).

[111] A. P. Chen, Z. X. Bi, C. F. Tsai, J. Lee, Q. Su, X. H. Zhang, Q. X. Jia, J. L. MacManus-Driscoll, and H. Y. Wang, Advanced Functional Materials **21,** 2423 (2011).

[112] W. Zhang, A. Chen, F. Khatkhatay, C. F. Tsai, Q. Su, L. Jiao, X. Zhang, and H. Wang, ACS Appl Mater Interfaces **5,** 3995 (2013).

[113] C. F. Tsai, L. Chen, A. P. Chen, F. Khatkhatay, W. R. Zhang, and H. Y. Wang, IEEE Transactions on Applied Superconductivity **23,** 8001204 (2013).

[114] Q. Su, D. Yoon, A. P. Chen, F. Khatkhatay, A. Manthiram, and H. Y. Wang, Journal of Power Sources **242,** 455 (2013).

[115] O. Lee, S. A. Harrington, A. Kursumovic, E. Defay, H. Y. Wang, Z. X. Bi, C. F. Tsai, L. Yan, Q. X. Jia, and J. L. MacManus-Driscoll, Nano Letters **12,** 4311 (2012).

[116] W. Zhang, A. Chen, Z. Bi, Q. Jia, J. L. MacManus-Driscoll, and H. Wang, Current Opinion in Solid State and Materials Science **18,** 6 (2014).

[117] A. Artemev, J. Slutsker, and A. L. Roytburd, Acta Materialia **53,** 3425 (2005).

[118] F. Khatkhatay, A. P. Chen, J. H. Lee, W. R. Zhang, H. Abdel-Raziq, and H. Y. Wang, ACS Applied Materials & Interfaces **5,** 12541 (2013).

[119] S. A. Harrington, J. Y. Zhai, S. Denev, V. Gopalan, H. Y. Wang, Z. X. Bi, S. A. T. Redfern, S. H. Baek, C. W. Bark, C. B. Eom, Q. X. Jia, M. E. Vickers, and J. L. MacManus-Driscoll, Nature Nanotechnology **6,** 491 (2011).

[120] Z. X. Bi, J. H. Lee, H. Yang, Q. X. Jia, J. L. MacManus-Driscoll, and H. Y. Wang, Journal of Applied Physics **106,** 5 (2009).

[121] Q. Su, D. Yoon, Z. Sisman, F. Khatkhatay, Q. X. Jia, A. Manthiram, and H. Y. Wang, International Journal of Hydrogen Energy **38,** 16320 (2013).

[122] A. P. Chen, Z. X. Bi, H. Hazariwala, X. H. Zhang, Q. Su, L. Chen, Q. X. Jia, J. L. MacManus-Driscoll, and H. Y. Wang, Nanotechnology **22,** 315712 (2011).

[123] J. J. Huang, C. F. Tsai, L. Chen, J. Jian, F. Khatkhatay, K. Y. Yu, and H. Y. Wang, Journal of Applied Physics **115,** 123902 (2014).

[124] H. J. Liu, L. Y. Chen, Q. He, C. W. Liang, Y. Z. Chen, Y. S. Chien, Y. H. Hsieh, S. J. Lin, E. Arenholz, C. W. Luo, Y. L. Chueh, Y. C. Chen, and Y. H. Chu, ACS Nano **6,** 6952 (2012).

[125] Y. M. Zhu, D. Ke, R. Yu, Y. H. Hsieh, H. J. Liu, P. P. Liu, Y. H. Chu, and Q. Zhan, Applied Physics Letters **102,** 5 (2013).

[126] C. Schmitz-Antoniak, D. Schmitz, P. Borisov, F. M. F. de Groot, S. Stienen, A. Warland, B. Krumme, R. Feyerherm, E. Dudzik, W. Kleemann, and H. Wende, Nature Communications **4** (2013).

[127] H. P. Wu, G. Z. Chai, T. Zhou, Z. Zhang, T. Kitamura, and H. M. Zhou, Journal of Applied Physics **115,** 9 (2014).

[128] D. H. Kim, N. M. Aimon, X. Y. Sun, and C. A. Ross, Advanced Functional Materials **24,** 2334 (2014).

[129] W. R. Zhang, J. Jian, A. P. Chen, L. Jiao, F. Khatkhatay, L. G. Li, F. Chu, Q. X. Jia, J. L. MacManus-Driscoll, and H. Y. Wang, Applied Physics Letters **104,** 5 (2014).

[130] L. Benco, Journal of Solid State Chemistry **111,** 440 (1994).

[131] L. E. Toth, *Transition metal carbides and nitrides* (Academic Press, New York, 1971).

[132] A. E. Palty, H. Margolin, and J. P. Neilsen, Transactions of the American Society for Metals **46,** 312 (1954).

[133] H. O. Pierson, *Handbook of Refractory Carbides and Nitrides: Properties, Characteristics, Processing, and Applications* (Noyes Publications, Westwood, 1996).

[134] S. H. Kim, H. Park, K. H. Lee, S. H. Jee, D. J. Kim, Y. S. Yoon, and H. B. Chae, Journal of Ceramic Processing Research **10,** 49 (2009).

[135] S. T. Oyama, *Chemistry of Transition Metal Carbides and Nitrides* (Blackie Academic & Professional, London, 1996).

[136] H. Wang, R. Araujo, J. G. Swadener, Y. Q. Wang, X. Zhang, E. G. Fu, and T. Cagin, Nuclear Instruments & Methods in Physics Research Section B **261,** 1162 (2007).

[137] R. Buhl, H. K. Pulker, and E. Moll, Thin Solid Films **80,** 265 (1981).

[138] S. Y. Zhang and W. G. Zhu, Journal of Materials Processing Technology **39,** 165 (1993).

[139] A. Schroer, W. Ensinger, and G. K. Wolf, Materials Science and Engineering A **140,** 625 (1991).

[140] D. Starosvetsky and I. Gotman, Biomaterials **22,** 1853 (2001).

[141] F. Khatkhatay, J. Jian, L. Jiao, Q. Su, J. Gan, J. I. Cole, and H. Y. Wang, Journal of Alloys and Compounds **580,** 442 (2013).

[142] F. Khatkhatay, L. Jiao, J. Jian, W. R. Zhang, Z. J. Jiao, J. Gan, H. B. Zhang, X. H. Zhang, and H. Y. Wang, Journal of Nuclear Materials **451,** 346 (2014).

[143] A. E. Kaloyeros and E. Eisenbraun, Annual Review of Materials Science **30,** 363 (2000).

[144] H. C. M. Knoops, L. Baggetto, E. Langereis, M. C. M. van de Sanden, J. H. Klootwijk, F. Roozeboom, R. A. H. Niessen, P. H. L. Notten, and W. M. M. Kessels, Journal of the Electrochemical Society **155,** G287 (2008).

[145] M. Saadaoui, H. van Zeijl, W. H. A. Wien, H. T. M. Pham, C. Kwakernaak, H. C. M. Knoops, W. M. M. Kessels, R. van de Sanden, F. C. Voogt, F. Roozeboom, and P. M. Sarro, IEEE Transactions on Components Packaging and Manufacturing Technology **1,** 1728 (2011).

[146] L. Djomeni, T. Mourier, S. Minoret, S. Fadloun, F. Piallat, S. Burgess, A. Price, Y. Zhou, C. Jones, D. Mathiot, and S. Maitrejean, Microelectronic Engineering **120,** 127 (2014).

[147] V. Chakrapani, F. Rusli, M. A. Filler, and P. A. Kohl, Journal of Power Sources **216,** 84 (2012).

[148] L. Djomeni, T. Mourier, S. Minoret, S. Fadloun, J. P. Barnes, D. Rouchon, S. Burgess, A. Price, L. Vandroux, and D. Mathiot, Silicon Compatible Materials, Processes, and Technologies for Advanced Integrated Circuits and Emerging Applications 4 **61,** 219 (2014).

[149] M. P. Warusawithana, C. Cen, C. R. Sleasman, J. C. Woicik, Y. L. Li, L. F. Kourkoutis, J. A. Klug, H. Li, P. Ryan, L. P. Wang, M. Bedzyk, D. A. Muller, L. Q. Chen, J. Levy, and D. G. Schlom, Science **324,** 367 (2009).

[150] S. Abel, D. Caimi, M. Sousa, T. Stoferle, C. Rossel, C. Marchiori, A. Chelnokov, and J. Fompeyrine, in *Oxide-Based Materials and Devices III*, San Francisco, California, 2012 (Proceedings of SPIE), p. 82630Y.

[151] U. C. Chung, D. Michau, C. Elissalde, S. Li, A. Klein, and M. Maglione, Thin Solid Films **520,** 1997 (2012).

[152] F. Sanchez, M. Varela, X. Queralt, R. Aguiar, and J. L. Morenza, Applied Physics Letters **61,** 2228 (1992).

[153] W. C. Shih and W. H. Yang, Physica B **405,** 234 (2010).

[154] G. Niu, J. Penuelas, L. Largeau, B. Vilquin, J. L. Maurice, C. Botella, G. Hollinger, and G. Saint-Girons, Physical Review B **83,** 054105 (2011).

[155] R. D. Vispute, J. Narayan, K. Dovidenko, K. Jagannadham, N. Parikh, A. Suvkhanov, and J. D. Budai, Journal of Applied Physics **80,** 6720 (1996).

[156] A. Kumar, Q. You, J. S. Kapat, A. Mangiaracina, A. Catletge, and Y. Vohra, Thin Solid Films **308,** 209 (1997).

[157] C. M. Jin, W. Wei, H. H. Zhou, T. H. Yang, and R. J. Narayan, Applied Physics Letters **93,** 3 (2008).

[158] A. Achour, K. A. Aissa, M. Mbarek, K. El Hadj, N. Ouldhamadouche, N. Barreau, L. Le Brizoual, and M. A. Djouadi, Thin Solid Films **538,** 71 (2013).

[159] P. Gupta and J. Narayan, Journal of Applied Physics **115,** 043513 (2014).

[160] K. H. Wong and Y. S. Leung, Thin Solid Films **354,** 55 (1999).

[161] R. K. Singh, O. W. Holland, and J. Narayan, Journal of Applied Physics **68,** 233 (1990).

[162] R. K. Singh and J. Narayan, Physical Review B **41,** 8843 (1990).

[163] B. Fultz and J. Howe, *Transmission Electron Microscopy and Diffractometry of Materials*, 4th ed. (Springer, New York, 2012).

[164] D. B. Williams and C. B. Carter, *Transmission Electron Microscopy: A Textbook for Materials Science* (Plenum Press, New York, 1996).

[165] C. R. Brundle, C. A. Evans, and S. Wilson, *Encyclopedia of Materials Characterization: Surfaces, Interfaces, Thin Films* (Butterworth-Heinemann, Boston, 1992).

[166] D. K. Schroder, *Semiconductor Material and Device Characterization* (Wiley, Hoboken, 2006).

[167] C. B. Sawyer and C. H. Tower, Physical Review **35,** 0269 (1930).

[168] D. M. Evans, A. Schilling, A. Kumar, D. Sanchez, N. Ortega, R. S. Katiyar, J. F. Scott, and J. M. Gregg, Philosophical Transactions of the Royal Society A **372,** 20120450 (2014).

[169] J. Rodel, W. Jo, K. T. P. Seifert, E. M. Anton, T. Granzow, and D. Damjanovic, Journal of the American Ceramic Society **92,** 1153 (2009).

[170] M. A. A. Issa, N. M. Molokhia, and Z. H. Dughaish, Journal of Physics D **16,** 1109 (1983).

[171] J. P. Guha and D. Kolar, Journal of the American Ceramic Society **56,** 5 (1973).

[172] J. P. Guha, Journal of the American Ceramic Society **62,** 627 (1979).

[173] Y. J. Kim, Y. Gao, G. S. Herman, S. Thevuthasan, W. Jiang, D. E. McCready, and S. A. Chambers, Journal of Vacuum Science & Technology A **17,** 926 (1999).

[174] J. Dubuisson and P. Basseville, in *Materials Science Research*, North Carolina State University, Raleigh, NC, 1964 (Plenum Press), p. 77.

[175] J. H. Hwang and Y. H. Han, Japanese Journal of Applied Physics Part 1 **39,** 2701 (2000).

[176] T. X. Li, Z. Hu, M. Zhang, K. S. Li, D. B. Yu, and H. Yan, Applied Surface Science **258,** 4558 (2012).

[177] E. V. Ramana, S. M. Yang, R. J. Jung, M. H. Jung, B. W. Lee, and C. U. Jung, Journal of Applied Physics **113,** 187219 (2013).

[178] T. Yamada, C. S. Sandu, M. Gureev, V. O. Sherman, A. Noeth, P. Muralt, A. K. Tagantsev, and N. Setter, Advanced Materials **21,** 1363 (2009).

[179] M. Cernea, I. Matei, A. Iuga, and C. Logofatu, Journal of Materials Science **36,** 5027 (2001).

[180] D. F. K. Hennings, B. Schreinemacher, and H. Schreinemacher, Journal of the European Ceramic Society **13,** 81 (1994).

[181] E. Wachtel and I. Lubomirsky, Scripta Materialia **65,** 112 (2011).

[182] H. Wang, A. Kvit, X. Zhang, C. C. Koch, and J. Narayan, MRS Proceedings **697**, P8.4 (2001).

[183] J. Shin, A. Goyal, S. Jesse, and D. H. Kim, Applied Physics Letters **94,** 252903 (2009).

[184] D. Fasquelle, M. Mascot, and J. C. Carru, Solid-State Electronics **75,** 6 (2012).

[185] J. P. George, J. Beeckman, W. Woestenborghs, P. F. Smet, W. Bogaerts, and K. Neyts, Nanoscale Research Letters **8,** 1 (2013).

[186] Q. Zhou, C. R. Zhou, H. B. Yang, G. H. Chen, W. Z. Li, and H. Wang, Journal of the American Ceramic Society **95,** 3889 (2012).

[187] L. O. Chua, IEEE Transactions on Circuit Theory **18,** 507 (1971).

[188] B. J. Choi, J. J. Yang, M. X. Zhang, K. J. Norris, D. A. A. Ohlberg, N. P. Kobayashi, G. Medeiros-Ribeiro, and R. S. Williams, Applied Physics A **109,** 1 (2012).

[189] L. Zhong, L. Jiang, R. Huang, and C. H. de Groot, Applied Physics Letters **104,** 093507 (2014).

[190] D. S. Jeong, R. Thomas, R. S. Katiyar, J. F. Scott, H. Kohlstedt, A. Petraru, and C. S. Hwang, Reports on Progress in Physics **75,** 076502 (2012).

[191] L. Hultman, Vacuum **57,** 1 (2000).

[192] C. Lee and Y. L. Kuo, JOM **59,** 44 (2007).

[193] J. Desmaison, P. Lefort, and M. Billy, Oxidation of Metals **13,** 505 (1979).

[194] H. Y. Chen and F. H. Lu, Journal of Vacuum Science & Technology A **23,** 1006 (2005).

[195] K. Hinode, Y. Homma, M. Horiuchi, and T. Takahashi, Journal of Vacuum Science & Technology A **15,** 2017 (1997).

[196] H. Van Bui, A. W. Groenland, A. A. I. Aarnink, R. A. M. Wolters, J. Schmitz, and A. Y. Kovalgin, Journal of the Electrochemical Society **158,** H214 (2011).

[197] L. Soriano, M. Abbate, J. C. Fuggle, P. Prieto, C. Jimenez, J. M. Sanz, L. Galan, and S. Hofmann, Journal of Vacuum Science & Technology A **11,** 47 (1993).

[198] I. Milosev, H. H. Strehblow, B. Navinsek, and M. Metikoshukovic, Surface and Interface Analysis **23,** 529 (1995).

[199] J. Narayan, P. Tiwari, X. Chen, J. Singh, R. Chowdhury, and T. Zheleva, Applied Physics Letters **61,** 1290 (1992).

[200] J. J. Yang, M. D. Pickett, X. M. Li, D. A. A. Ohlberg, D. R. Stewart, and R. S. Williams, Nature Nanotechnology **3,** 429 (2008).

[201] G. S. Tang, F. Zeng, C. Chen, H. Y. Liu, S. Gao, C. Song, Y. S. Lin, G. Chen, and F. Pan, Nanoscale **5,** 422 (2013).

[202] M. Schubert, N. Ashkenov, T. Hofmann, M. Lorenz, H. Hochmuth, H. von Wenckstern, M. Grundmann, and G. Wagner, Annalen Der Physik **13,** 61 (2004).

[203] N. Ashkenov, A. Schubert, E. Twerdowski, H. von Wenckstern, B. N. Mbenkum, H. Hochmuth, M. Lorenz, W. Grill, and M. Grundmann, Thin Solid Films **486,** 153 (2005).

[204] V. M. Voora, T. Hofmann, M. Brandt, M. Lorenz, M. Grundmann, and M. Schubert, Physica Status Solidi C **5,** 1328 (2008).

[205] V. M. Voora, T. Hofmann, M. Brandt, M. Lorenz, N. Ashkenov, M. Grundmann, and M. Schubert, Applied Physics Letters **95,** 3 (2009).

[206] M. Brandt, H. Frenzel, H. Hochmuth, M. Lorenz, M. Grundmann, and J. Schubert, Journal of Vacuum Science & Technology B **27,** 1789 (2009).

[207] V. M. Voora, T. Hofmann, M. Schubert, M. Brandt, M. Lorenz, M. Grundmann, and N. Ashkenov, Applied Physics Letters **94,** 142904 (2009).

[208] P. Schwinkendorf, M. Lorenz, H. Hochmuth, Z. P. Zhang, and M. Grundmann, Physica Status Solidi A **211,** 166 (2014).

[209] J. Gottmann, T. Klotzbucher, and E. W. Kreutz, in *Alt '97 International Conference on Laser Surface Processing*, Limoges, France, 1998 (Proceedings of SPIE), p. 8.

[210] E. W. Kreutz and J. Gottmann, Physica Status Solidi A **166,** 569 (1998).

[211] E. W. Kreutz and J. Gottmann, Journal of the European Ceramic Society **24,** 979 (2004).

[212] P. Yvon and F. Carre, Journal of Nuclear Materials **385,** 217 (2009).

[213] T. R. Allen, J. T. Busby, R. L. Klueh, S. A. Maloy, and M. B. Toloczko, JOM **60,** 15 (2008).

[214] V. Firouzdor, L. Wilson, K. Sridharan, B. Semerau, B. Hauch, J. Brechtl, J. I. Cole, and T. R. Allen, Key Engineering Materials **507,** 3 (2012).

[215] R. D. Mariani, D. L. Porter, T. P. O'Holleran, S. L. Hayes, and J. R. Kennedy, Journal of Nuclear Materials **419,** 263 (2011).

[216] I. Kim, F. Khatkhatay, L. Jiao, G. Swadener, J. I. Cole, J. Gan, and H. Y. Wang, Journal of Nuclear Materials **429,** 143 (2012).

[217] S. A. Maloy, M. Toloczko, J. Cole, and T. S. Byun, Journal of Nuclear Materials **415,** 302 (2011).

[218] P. S. Weiser, S. Prawer, A. Hoffman, R. R. Manory, P. J. K. Paterson, and S. A. Stuart, Journal of Applied Physics **72,** 4643 (1992).

[219] P. S. Weiser, S. Prawer, A. Hoffman, P. J. K. Paterson, and R. R. Manory, Journal of Applied Physics **76,** 2164 (1994).

[220] W. Schintlmeister, O. Pacher, K. Pfaffinger, and T. Raine, Journal of the Electrochemical Society **123,** 924 (1976).

[221] K. Tucek, M. Jolkkonen, J. Wallenius, and W. Gudowski, Nuclear Technology **157,** 277 (2007).

[222] M. Chotirach, S. Tantayanon, S. Tungasmita, and K. Kriausakul, Journal of Membrane Science **405,** 92 (2012).

[223] P. C. Tortorici and M. A. Dayananda, Journal of Nuclear Materials **204,** 165 (1993).

[224] M. P. Dariel, Acta Metallurgica **23,** 473 (1975).

[225] H. Okamoto, Journal of Phase Equilibria and Diffusion **29,** 116 (2008).

[226] M. A. Dayananda and D. A. Behnke, Scripta Metallurgica et Materialia **25,** 2187 (1991).